2015-07-02

Design and Fabrication of Optical Polymer Waveguide Devices for Optical Interconnects and Integrated Optical Coherence Tomography

Guomin Jiang
University of Miami, jgmmiami@gmail.com

UNIVERSITY OF MIAMI

DESIGN AND FABRICATION OF OPTICAL POLYMER WAVEGUIDE DEVICES FOR OPTICAL INTERCONNECTS AND INTEGRATED OPTICAL COHERENCE TOMOGRAPHY

By

Guomin Jiang

A DISSERTATION

Submitted to the Faculty
of the University of Miami
in partial fulfillment of the requirement of
the degree of Doctor of Philosophy

Coral Gables, Florida

August 2015

UNIVERSITY OF MIAMI

A dissertation submitted in partial fulfillment of
the requirements for the degree of
Doctor of Philosophy

DESIGN AND FABRICATION OF OPTICAL POLYMER WAVEGUIDE DEVICES FOR OPTICAL INTERCONNECTS AND INTEGRATED OPTICAL COHERENCE TOMOGRAPHY

Guomin Jiang

Approved:

_____ Michael R. Wang, Ph.D. Professor of Electrical and Computer Engineering	_____ Ali Ghahremaninezhad, Ph.D. Assistant Professor of Civil, Architectural and Environmental Engineering
_____ Sung Jin Kim, Ph.D. Assistant Professor of Electrical and Computer Engineering	_____ Olga Korotkova, Ph.D. Associate Professor of Physics
_____ Onur Tigli, Ph.D. Assistant Professor of Electrical and Computer Engineering	_____ Dean of the Graduate School

JIANG, GUOMIN (Ph.D., Electrical and Computer Engineering)
Design and Fabrication of Optical Polymer Waveguide Devices for Optical Interconnects and Integrated Optical Coherence Tomography (August 2015)

Abstract of a dissertation at the University of Miami.

Dissertation supervised by Professor Michael R. Wang.
No. of pages in text. (151)

Optical interconnects is a promising technique to boost the speed of electronic systems through replacing high speed electrical data buses using optical ones. Optical coherence tomography is an attractive imaging technique that has been widely used in medical imaging applications with capability of high resolution subsurface cross sectional imaging in living tissues. Both the optical interconnects and the optical coherence tomography imaging may benefit from the use of integrated optics technology in particular polymer waveguides that can be designed and fabricated to improve the device capability, system compactness, and performance reliability.

In this dissertation, we first present our innovative design and realization on the polymer waveguides with 45° integrated mirrors for optical interconnects using the vacuum assisted microfluidic (VAM) soft lithography. VAM is a new microfluidic based replication technique which can be utilized to improve the performance of imprinted devices by eliminating the residue planar layer and accomplish complex devices incorporating different materials in the same layer. A prism-assisted inclined UV lithography technique is introduced to increase the slanted angles of the side walls of the microstructures and to fabricate multidirectional slanted microstructures. It is also used to fabricate 45° integrated mirrors in polymer waveguides to support surface normal optical

coupling for optical interconnects. A dynamic card-to-backplane optical interconnects system has also been demonstrated based on polymer waveguides with tunable optofluidic couplers. The operation of the tunable optofluidic coupler is accomplished by controlling the position of air bubbles and index matching liquid in the perpendicular microfluidic channel for refractive index modulation. The dynamic activation and deactivation of the backplane optofluidic couplers can save the optical signal power. 10 Gbps eye diagrams of the dynamic optical interconnect link have been demonstrated showing the needed high performance optical interconnection.

The design and fabrication of planar concave grating (PCG) wavelength demultiplexer on SU-8 polymer waveguides is presented for wavelength division multiplexing system to further support optical interconnection applications. The PCG wavelength demultiplexers with a flattened spectral response are accomplished by innovative design of a multi-mode interference coupler as input to the PCG. The mode field distribution at the PCG planar input is controlled by adjusting the width of an input waveguide taper connected to multi-mode interference coupler. By extending the channel number and density, the PCG wavelength demultiplexer can become a compact optical spectrometer which could be used to realize a portable optical coherence tomography system. The design of a 200-channel and a 1024-channel PCG spectrometers with low crosstalk, small channel loss, good uniformity, and chip size of 3 cm × 3 cm and 8 cm × 8 cm, respectively, has been performed. An alternative quicker solution using cylindrical optics with a vertical beam size of about 3 mm in the diffraction plane is also demonstrated to achieve a compact optical spectrometer, which is capable of supporting optical coherence tomography subsurface imaging applications.

Acknowledgements

Time files. It has been four years since I came to University of Miami to pursue my Ph.D. degree. Every time I look back on my experience over the last four years, I am truly grateful for all the people around me. Your help and support provided me with great courage and faith to continuously improve myself and pursue academic innovation.

I would like to express my deepest gratitude to my advisor, Professor Michael R. Wang. He is a kind and knowledgeable person. He offered me many excellent ideas and useful guidance during my Ph.D. studies. Dear Professor Wang, thank you very much for your patient guidance, enthusiastic encouragement, and useful critiques of my research work throughout my student education. I learned a lot from your profound knowledge, wisdom, and your professional way of working.

I would like to extend great appreciation to my graduate committee members, Professor Sung Jin Kim, Professor Onur Tigli, Professor Ali Ghahremaninezhad, and Professor Olga Korotkova. I am so honored to have had you on my committee: your broad views and sensitive research perspectives inspired me in new ways to solve problems. I must say “Thank you” for providing me with constructive advice and for the invaluable time you contributed to help me complete my dissertation.

I also need to thank my fellow colleagues: Mr. Kai Shen, Mrs. Hui Lu, Mr. Sarfaraz Baig, Mr. Hossein Shokri Kojori, Mr. Young-Hun Paik, Mr. Jinhui Gu, Mr. Guoyi Li, Dr. Yuxin Wei, Dr. Bing Li, and Dr. Yunpeng Wang. With your friendship, I feel warm and happy every day. Thank you for all the assistance and encouragement you provided me with during my daily life.

I would also like to thank New Span Opto-Technology Inc. for providing instruments and facility support during my Ph.D. research.

Last but not least, I want to thank my family: my parents, my parents-in-law, and my wife. No matter what kind of difficulties I face, I always have courage to overcome them because of your constant support, encouragement, and unconditional love. I love you all.

TABLE OF CONTENTS

page

LIST OF FIGURES vii

LIST OF TABLES xv

Chapter

1 INTRODUCTION 1
1.1 Introduction and Motivation 1
1.1.1 Integrated Optics for Optical Interconnects 2
1.1.2 Integrated Optics for Wavelength Division Multiplexing 5
1.1.3 Integrated Optics for Miniaturized Spectrometer for Optical Coherence Tomography 7
1.2 Polymer Waveguide Devices 10
1.2.1 Selection of Polymer for Our Integrated Optics 10
1.2.2 Fabrication of Polymer Waveguide 12
1.2.3 Polymer Waveguide with Integrated Mirrors 14
1.3 Dissertation Overview 15

2 LITHOGRAPHY FABRICATION OF POLYMER WAVEGUIDES 19
2.1 Photolithography Fabrication of Polymer Waveguides 20
2.2 Vacuum Assisted Microfluidic Fabrication of Polymer Waveguides 21
2.2.1 Master and PDMS Stamp Fabrication 24
2.2.2 VAM Fabrication of Multi-mode Polymer Waveguides 26
2.2.3 VAM Fabrication of Single-Mode Polymer Waveguides 28
2.2.4 VAM Fabrication of Multi-section Polymer Waveguides Incorporating Different Materials 30
2.3 Synthesized Polymer Waveguide Resins Supporting Soft Lithography Fabrication 31
2.4 Summary 35

3 PRISM-ASSISTED INCLINED UV LITHOGRAPHY FOR 3D MICROSTRUCTURE FABRICATION 37
3.1 Microstructure Fabrication 38
3.2 Prism-assisted UV Lithography for Slanted Structures with Large Exposure Angles 41
3.3 Prism-assisted One-step UV Lithography for Multidirectional Inclined Structures 46
3.4 Summary 54

4 FLEXIBLE POLYMER WAVEGUIDES WITH INTEGRATED MIRRORS FOR OPTICAL INTERCONNECTS 55
4.1 VAM Soft Lithography Fabrication of Polymer Waveguides with Integrated Mirrors 56

4.1.1 SU-8 Master and PDMS Mold Fabrication 57
4.1.2 Polymer Waveguides with Integrated Mirrors Imprint 61
4.2 Optical Test 63
4.3 Summary 66

5 TUNABLE OPTOFLUIDIC COUPLER FOR DYNAMIC CARD-TO-BACKPLANE OPTICAL INTERCONNECTS 68
5.1 Simulation of Operation of Optofluidic Coupler 72
5.2 VAM Soft Lithography Fabrication 73
5.3 Tunable Optofluidic Coupler 77
5.4 Optical Test of Dynamic System 79
5.5 High Speed Test 82
5.6 Summary 85

6 PLANAR CONCAVE GRATING WAVELENGTH DEMULTIPLEXER FOR OPTICAL INTERCONNECTION AND INTEGRATED OPTICAL COHERENCE TOMOGRAPHY 87
6.1 Planar Concave Grating based on SU-8 Polymer Waveguides 88
6.1.1 SU-8 Polymer Waveguide 88
6.1.2 Basic Theory of Planar Concave Grating 91
6.1.2 Design and Simulations of PCG 92
6.1.4 Planar Concave Grating Fabrication and Testing 98
6.2 Planar Concave Grating with Flattened Spectral Response for Optical Interconnects 105
6.2.1 MMI Aperture for the Desired Input Field Profile 106
6.2.2 MMI-PCG Design and Simulations 109
6.2.3 MMI-PCG Fabrication and Testing 112
6.3 Planar Concave Grating for Integrated Spectrometer 115
6.3.1 SD-OCT Parameters 116
6.3.2 PCG Spectrometer for SD-OCT 117
6.3.3 Alternative Compact Spectrometer 122
6.4 Summary 133

7 CONCLUSION 135
7.1 Recommendations for Future Work 138

REFERENCES 141

LIST OF FIGURES

Page

Fig. 1.1. Several physical interconnection hierarchies. 4

Fig. 1.2. WDM functions schematic. 6

Fig. 1.3. Schematic of a SD-OCT system. 8

Fig. 1.4. Bulky SD-OCT system in our lab showing optical spectrometer and reference arm optics. 9

Fig. 1.5. Propagation losses of several reported polymer waveguides with different polymer materials. 12

Fig. 2.1. Schematic illustration of the process of photolithography fabrication. 20

Fig. 2.2. Schematic diagram of theoretical μTM fabrication process. 22

Fig. 2.3. Schematic of practical μTM fabrication process with remnant planar layer. 22

Fig. 2.4. Schematic illustration of the whole process of (a) PDMS mold fabrication and (b) polymer waveguide imprint. 24

Fig. 2.5. Schematic of the fabrication process of the master. 25

Fig. 2.6. Schematic of the fabrication process of the PDMS mold. 26

Fig. 2.7. Image of a fabricated PDMS mold. 26

Fig. 2.8. Schematic process of VAM fabrication of polymer waveguides. 27

Fig. 2.9. Image of experimental setup of VAM fabrication. 27

Fig. 2.10. SEM image of imprinted polymer waveguides. 28

Fig. 2.11. Schematic of the PDMS mold for the VAM system. 29

Fig. 2.12. SEM image of the fabricated single-mode channel waveguide [90]. 29

Fig. 2.13. A design of the VAM system for multi-section polymer waveguides fabrication. 31
Fig. 2.14. SEM image of the fabricated multi-section polymer waveguides [91] 31
Fig. 2.15. The transmittance properties of the synthesized UV curable core resin of 15 μm thickness [90]. 33
Fig. 2.16. The refractive index change of light sensitive resin. 34
Fig. 2.17. The absorption spectrum of the UV cured light sensitive resin. The sharp peak at 532 nm is due to the laser beam. 35
Fig. 3.1. Schematic diagram of inclined UV lithography in the air. 39
Fig. 3.2. (a) Schematic diagram of inclined UV lithography in an index matching liquid and (b) simulation of the exposure angle versus slanted stage angle in air, water, heptane, and glycerol. 40
Fig. 3.3. The sample/mask plate holder with rotation features for multi-directional inclined UV exposure. 40
Fig. 3.4. (a) Schematic diagram of prism-assisted UV lithography for the expansion of the exposure angle in the resin. (b) Schematic of cross-sectional view of the UV light path bending. 42
Fig. 3.5. The exposure angle θ in SU-8 as a function of the prism angle α and slanted stage angle β. 43
Fig. 3.6. SEM images of the fabricated inclined structures with different exposure angles. 43
Fig. 3.7. SEM images of the fabricated 3D inclined microstructures with 45° exposure angles. 44

Fig. 3.8. (a) Schematic of initiating cross-linking of the resin. (b) Schematic of cross-section view of the UV light path bending showing both incident and reflection exposures. 45

Fig. 3.9. SEM images of the inclined structures with 45° exposure angles fabricated by internal reflected UV exposure beams. 45

Fig. 3.10. (a) Schematic diagram of fabricating multi-directional structures using a polyhedron prism. (b) Schematic of a cross-sectional diagram showing the UV light paths. 47

Fig. 3.11. Fabrication of upside-down tripod structure by one-step exposure using a corner prism. 47

Fig. 3.12. Two specific ways for the arrangement of the basic upside-down tripod structures. 48

Fig. 3.13. SEM images of the fabricated complex 3D microstructures using a corner prism. 50

Fig. 3.14. Fabrication of horn and fan-shaped structures by one-step exposure using a cone prism. 51

Fig. 3.15. SEM images of the fabricated similar structure of Fig. 3.13(b) without enough exposure dosage with (b) as magnified view of a local portion of (a). 52

Fig. 3.16. The effective exposure area and its percentage of base area (a) depend on the number of side surface and (b) depend on the circumradius of the base. 53

Fig. 4.1. Schematic illustration of the whole process of (a) PDMS mold fabrication and (b) polymer waveguide imprint. 56
Fig. 4.2. (a) Schematic diagram of prism-assisted inclined UV lithography. (b) Schematic of cross-section view of the UV light path bending. 58
Fig. 4.3. Schematic of the fabrication process of the SU-8 master and the PDMS mold. 59
Fig. 4.4. Top view of the fabricated SU-8 master with full depth inclined surfaces (a) and half depth inclined surfaces (b). 60
Fig. 4.5. Schematic process of polymer waveguides imprint. 62
Fig. 4.6. The image of the flexible polymer waveguides with 45° integrated mirrors. 62
Fig. 4.7. SEM images of imprinted polymer waveguides with full mirrors and half mirrors. 63
Fig. 4.8. Light spots detection of the polymer waveguides for (a) full mirrors and (b) half mirrors. 64
Fig. 4.9. Total insertion loss (a) and coupling loss (b) for full mirrors. Total insertion loss (c) and coupling loss (d) for half mirrors. 65
Fig. 5.1. Schematic of array waveguide evanescent coupler for card-to-backplane optical interconnection. 69
Fig. 5.2. Schematic illustration of (a) dynamic card-to-backplane optical interconnection and (b) tunable optofluidic coupler. 71
Fig. 5.3. The reflected light power and output light power compare to input light power as a function of the depth of incline surface at on and off states. .. 73

Fig. 5.4. Schematic illustration of the process of (a) PDMS mold fabrication and (b) polymer waveguide and microfluidic channel structure imprint. 74
Fig. 5.5. SEM images of the fabricated polymer waveguide and microfluidic channel structure with (a) 1/3 mirrors and (b) half mirrors. 76
Fig. 5.6. Image of the whole system with waveguide array and three optofluidic couplers. 77
Fig. 5.7. Optical micrographs of the operation of tunable optofluidic coupler (a) air bubble contact with waveguide mirrors (b) glycerol contact with waveguide mirrors. 78
Fig. 5.8. ON/OFF operation of the optofluidic couplers. The interconnect beam in the waveguide is propagating from right to left. 79
Fig. 5.9. Reflected power from (a) coupler I with 1/3 mirrors and (b) coupler II with half mirrors when activated (black square) or deactivated (red circle). 80
Fig. 5.10. The change of reflected power from the coupler III. 81
Fig. 5.11. Bit sequences are superimposed over one another to obtain the final eye diagram. 82
Fig. 5.12. The full width of the time histogram for p-p jitter. 83
Fig. 5.13. (a) Schematic setup and (b) experimental setup of high speed test. 84
Fig. 5.14. Measured 10 Gbps eye diagrams for coupler III when both couplers I and II were (a) activated and (b) deactivated. 85
Fig. 6.1. Cross section of a small SU-8 strip waveguide. 89
Fig. 6.2. Single-mode (SM) condition and fundamental mode (FM) cutoff. 89

Fig. 6.3. Calculated fundamental (TE00) mode profile. 90
Fig. 6.4. Schematics with the Rowland configuration for PCG..... 91
Fig. 6.5. Schematic of a grating with (a) two paths and (b) coordinate system..... 93
Fig. 6.6. Simulated spectral response of 4-channel PCG..... 95
Fig. 6.7. Simulated spectral response of 16-channel PCG..... 96
Fig. 6.8. The relationship between channel spacing and Rowland circle radius. 96
Fig. 6.9. The calculated values of birefringence and wavelength shift as a function of hco..... 97
Fig. 6.10. The center wavelength shift as a function of waveguide thickness h_{co}. 98
Fig. 6.11. Extra loss related to the rounding radius of grating teeth..... 98
Fig. 6.12. PCG fabrication process. 99
Fig. 6.13. Microscope images of (a) the fabricated PCG device, (b) the further magnified grating portion, (c) the cross section of straight reference waveguides, and (d) the cross section of 4-channel output waveguides.. 100
Fig. 6.14. (a) Schematic of waveguide mode profile testing system and (b) picture of the experimental setup. 101
Fig. 6.15. Mode profiles of the 2.5 μm and 5 μm wide waveguides. 102
Fig. 6.16. (a) Schematic of PCG test system and (b) picture of the experimental setup..... 103
Fig. 6.17. The measured transmission spectrum of the fabricated 4-channel PCG.. 104
Fig. 6.18. The measured transmission spectrum of the fabricated 16-channel PCG. 104
Fig. 6.19. The schematic diagram of the MMI-PCG. 105
Fig. 6.20. Schematic image of a MMI aperture for a PCG. 107

Fig. 6.21. (a) Schematic geometry of MMI aperture. (b)-(f) Simulated filed distribution of the 10 μm wide W MMI with input taper widths w of 4.0, 6.0, 7.0, 7.7, and 9.0 μm, respectively. 108
Fig. 6.22. Mode field distribution at the end of MMI for different input taper widths w. 109
Fig. 6.23. Simulated transmission spectrum of (a) MMI-PCG with variation of input taper width w of (b) MMI-PCG with a 7.7 μm wide input taper. 111
Fig. 6.24. Microscope images of (a) the fabricated MMI-PCG and (b) magnified image of the grating. 112
Fig. 6.25. Microscope images of the fabricated MMI aperture with input taper width w of (a) 4 μm, (b) 6 μm, (c) 7 μm, and (d) 8 μm. 113
Fig. 6.26. Measured spectral response of (a) MMI-PCG with variation of input taper width w and (b) MMI-PCG with 7 μm wide input taper 114
Fig. 6.27. Bulky optical spectrometer portion of SD-OCT system. 116
Fig. 6.28. Simulated transmission spectra for the 200-channel PCG (a) at central channels and (b) over the complete spectral range 120
Fig. 6.29. Simulated transmission spectrum for the 1024-channel PCG (a) at central channels and (b) over the spectral range from 1260 nm to 1280 nm. 121
Fig. 6.30. Schematic of a compact spectrometer. 123
Fig. 6.31. The optical design and ZEMAX ray tracing of the compact spectrometer. 126

Fig. 6.32. (a) Total irradiance and (b) X-cross irradiance of the detector at 840 nm wavelength before tilting the detector and its collection lens. 127

Fig. 6.33. (a) Total irradiance and (b) X-cross irradiance at 790 nm wavelength; (c) Total irradiance and (d) X-cross irradiance at 890 nm wavelength. 128

Fig. 6.34. (a) Total irradiance and (b) X-cross irradiance of the detector at 840 nm wavelength after tilting the detector and its collection lens with 4°. 128

Fig. 6.35. (a) Total irradiance and (b) X-cross irradiance at 790 nm wavelength; (c) Total irradiance and (d) X-cross irradiance at 890 nm wavelength. 129

Fig. 6.36. Experimental setup of the compact spectrometer system. 130

Fig. 6.37. Dispersion plot of spectrometer. 130

Fig. 6.38. (a) Sample interferogram measured by compact spectrometer in the SD-OCT system with a mirror in the sample arm and (b) the reconstructed data showing the axial resolution. 131

Fig. 6.39. OCT signal roll-off versus sample depth. 131

Fig. 6.40. OCT images of the (a) orange sample, (b) onion sample, and (c) fingerprint. 132

LIST OF TABLES

Page

Table 6.1. The design parameters of 4-channel and 16-channel PCGs. 94

Table 6.2. The parameters of the designed MMI-PCG. 110

Table 6.3. The design parameters of the PCG spectrometers. 118

Chapter 1

Introduction

1.1 Introduction and Motivation

The concept of "integrated optics" was first mentioned by Dr. Miller in 1969 [1], in which miniaturized optical devices including optical fiber and optical integrated circuits (OICs) would replace the conventional wire links and electrical integrated circuits [2]. It is based on guided wave optics principle with light being trapped inside a higher refractive index waveguide core medium surrounded by lower refractive index cladding or air. The light trapping during propagation can be visualized as total internal reflection while being better described by propagating mode solutions of Maxwell's equations of electromagnetic waves in waveguide geometry with boundary conditions. The light propagation in an optical channel waveguide is similar to that in an optical fiber. The controlled light propagation can facilitate the formation of functional optical device elements such as modulators, wavelength multiplexers, miniaturized spectrometers, add/drop filters, beam splitters, fanouts, switches, and various couplers. It can offer fascinating planar lightwave circuits with light path being crossing or parallel on a common substrate that can be either ridged or flexible to benefit the applications in light signal and power delivery.

The integrated optics approach has been widely used for optical interconnection, offering significant advantages in performance, compactness, stability, and cost when compared to conventional electrical methods. Recently, integrated optics has been used

for optofluidics [3, 4] and bio-sensing [5] applications to replace bulky sensor components. The conventional optical coherence tomography (OCT) system is large, unwieldy, and expensive which contains many bulky optical components such as beam splitters, reference arm optics, and optical spectrometers. Integrated optics could replace some of these bulky optical components by using miniaturized integrated optical devices, making OCT system smaller, compacter, and lower cost for portable applications.

The evolution of integrated optics has migrated from earlier work in waveguide theory, simulation, and fabrication, to recent efforts in designing and optimizing functional elements in optical interconnection, semiconductor laser diode, integrated bio-sensing, and integrated OCT. In particular, integrated optics is playing more and more important role in optical interconnection, miniaturized optical spectrometer, and wavelength demultiplexing element. The significances of integrated optics in these applications are summarized below.

1.1.1 Integrated Optics for Optical Interconnects

The metallic wires have become the prevailing medium for data communication since their introduction over a hundred years ago [6]. The demand for continually increasing data rates and bandwidth has led to the increase of the speed and complexity of integrated circuits, which has advanced from very large scale integrated circuits to ultra large scale integrated circuits [7]. However, as the continuous increase of signal frequency, the number of signal channels, the number of small components, and the degree of integration, electrical signal on board is limited by its high-frequency propagation loss, crosstalk, bandwidth capacity, electromagnetic interference, and power dissipation, which

eventually limits the scalability of electrical interconnects for high speed communications [8-11].

The severe line attenuation results from the skin effect loss and the propagation loss. The skin effect is the tendency of an electric current to gravitate towards the surface of the conductor as opposed to its core, resulting in the useful cross sectional area of the conductor to decrease and the effective resistance to increase [12]. The propagation loss, which caused by the heating effect on the dielectric media, begin to dominate at frequencies above 1 GHz [13]. So the whole system requires more energy and introduces more power loss when signal rate increases.

The high-density interconnect means narrow line-width and spacing. It increases crosstalk and parasitic capacitance for metallic interconnects. Therefore, longer electrical interconnection lines with high density consume much more power.

Electromagnetic interference is a complex phenomenon that takes place at different levels within electronic systems including the chassis, board, component, and device levels [14-16]. In efforts to reduce power consumption and improve performance, continuous decrease in threshold voltage and power supply levels have increased electrical links' vulnerability to electromagnetic interference. Increasing in clock and bus speed also increases the circuit signal radiation and switching noises.

To overcome the aforementioned problems associated with metallic wire based interconnects, optical interconnects have emerged [17-23]. The use of light to send message has existed a long time ago in free space, such as fire signal, smoke signal, and flashing light. Since the introduction of optical fibers with significant reduction of fiber loss, optical fibers based communication has become the dominant technology for long-

distance and high-capacity communications from 1980's. It is typically used for optical signal transmission for middle range (10-300 m) and long range (multi-km and longer) telecommunication.

The importance of optical communication is not only on the long distance communication but also on shorter distance interconnections especially for high data rate signals. Fig. 1.1 presents several physical communication/interconnection hierarchies [17]. Significantly increased clock rates are rapidly outpacing the electrical backplanes of computing systems favoring the use of alternative optical interconnects (short-reached optical interconnects). With the advantages of low crosstalk, high bandwidth capacity, and minimization of electromagnetic interference, optical interconnects have attracted significant attention in high-density high-speed data transmission for short distance communication.

	MAN/WAN	LAN	System	Rack	Card	Module	Chip
	Metro, long-haul	Campus, enterprise	Rack-to-Rack	Card-to-Card	Module-to-Module	Chip-to-Chip	On-Chip
							
Distance	Multi-km	100's m	10's m	0.3-1 m	0.1-0.3 m	5-100 mm	0-20 mm
Number of lines	1	1-10	100	100-1000	1000	10000	100000
Use of Optics	Since the 1980s	Since the late 1990s	1990s-2010	2010+	2010-2015	Probably after 2015	Later, if ever

Fig. 1.1. Several physical interconnection hierarchies.

For a complex system, a few cards are often plugged into a backplane containing the interconnect links between the cards. Backplane can be completely passive or can contain active switching components [17]. Fiber-based, free-space optical technologies, and planar waveguides have all been considered for use in card-to-backplane and card-to-card optical interconnects.

Fiber-based optical interconnects have been widely used for long distance and mid-range telecommunication. For card-to-card optical interconnects, fiber-based interconnects involve the integration of conventional fibers in low-cost rigid or flexible substrates. It can benefit from the well-established fiber-based technologies. However, due to high cost and dense wiring congestion, fiber-based solution seems impractical.

Free-space optical technologies involve the use of free-space optical elements such as micro-lenses, gratings, and mirror structures to route free-space optical beams over the backplane area. Such system can offer the flexible interconnect routing scheme in three dimensions enabling a large number of optical link within a small system. However, it requires strict fabrication and alignment to achieve high performance operation making it difficult for assembling and packaging. Furthermore, it subjects to vibration sensitivity and environmental noise.

Optical waveguide can be assembled on a board to facilitate the board level optical interconnects. Grating couplers and 45° integrated mirrors have been widely used for surface normal coupling. This approach offers excellent interconnect path stability and low cost fabrication. It is an attractive technique for board level optical interconnects. The dynamic optical interconnection [24-26] is also important since it can facilitate ON/OFF control of the interconnect link eliminating unnecessary interconnect link when not in use. We will present our contribution to the card-to-backplane optical interconnects in this dissertation.

1.1.2 Integrated Optics for Wavelength Division Multiplexing

A wavelength division multiplexing (WDM) technique multiplexes multiple optical carrier signals on a single optical fiber by using different laser wavelengths to carry

different signals, providing an effective and low cost method to dramatically increase the capacity of optical communication [27]. A simple WDM function is schematically illustrated in Fig. 1.2. The key optical components in the WDM system are wavelength multiplexers and demultiplexers. The different signal wavelengths are joined together at the input to the system by the multiplexers and split apart at the output of the system by the demultiplexers.

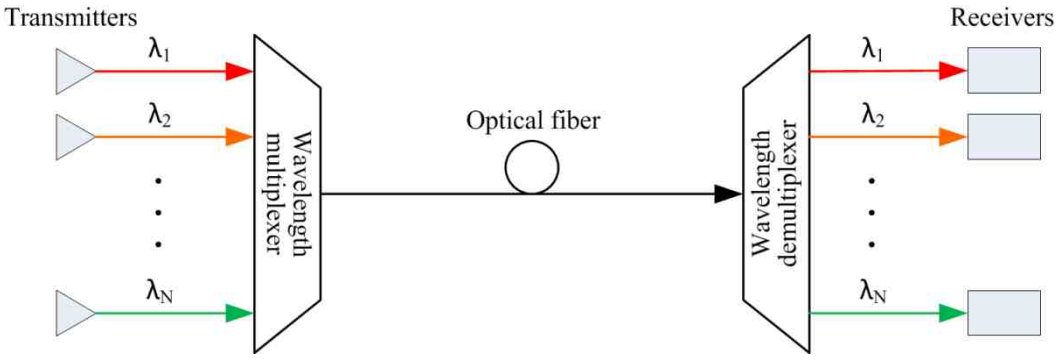

Fig. 1.2. WDM functions schematic.

Especially for long distance fiber link with existing planted optical fibers, the effective use of WDM can increase the channel capacity of the communication link. On the board level such WDM may not be necessary for short distance interconnect. However, since all optically interconnected system would face external connection with fiber link, the WDM device is still necessary to bridge to the external fiber for communication capacity improvement. The wavelength demultiplexer can also be applied for integrated spectrometer because of its wavelength separation property. A conventional spectrometer is a bulky and expensive component in an OCT system, which can be impressively compacted by using a wavelength demultiplexer for integration.

Many different waveguide based wavelength demultiplexers have been proposed, mainly including planar concave grating (PCG) [28], arrayed waveguide grating (AWG)

[29], ring resonator [30], and Mach-Zehnder interferometers. PCG and AWG have been widely researched and made great progress due to their compactness, low cost, large fabrication tolerance and high performance. We consider PCG for WDM system because of its significant size advantage over AWG [31, 32]. PCG device can be as small as only a few mm^2 in local area. We will present our contribution to the PCG based wavelength demultiplexer for WDM system in this dissertation.

1.1.3 Integrated Optics for Miniaturized Spectrometer for Optical Coherence Tomography

Besides the optical interconnection and communication, optical imaging is another important application area that greatly benefits the human life and science. Not to mention the wide spread application of imaging sensor array in cellphone imaging, security monitoring imaging, telescope imaging, and microscope imaging, in the scientific development there are three optical imaging technologies that have recently attracted great medical applications. One is confocal imaging that can explore the three-dimensional (3D) spatial imaging of biological tissues through depth level focusing scanning. This confocal imaging has been used to study real-time detection of skin cancers at the bedside [33]. Another is spectral imaging that explores the 3D imaging of a spatial area along with a spectral dimension. The spectral imaging can enhance the image contrast by selective filtering of interested spectral image frames and enhance the visibility of bio markers. The third imaging technique is the optical coherence tomography [34, 35] that can perform high resolution 3D spatial imaging of biological tissues with greater depth than confocal imaging. The OCT has been widely used in urology, ophthalmology, gastroenterology, and dermatology. Since both the confocal

imaging and spectral imaging rely mostly on bulk optics, the integrated optics however may benefit more to the technological development and compact packaging of OCT system. We now discuss the needs in OCT imaging here.

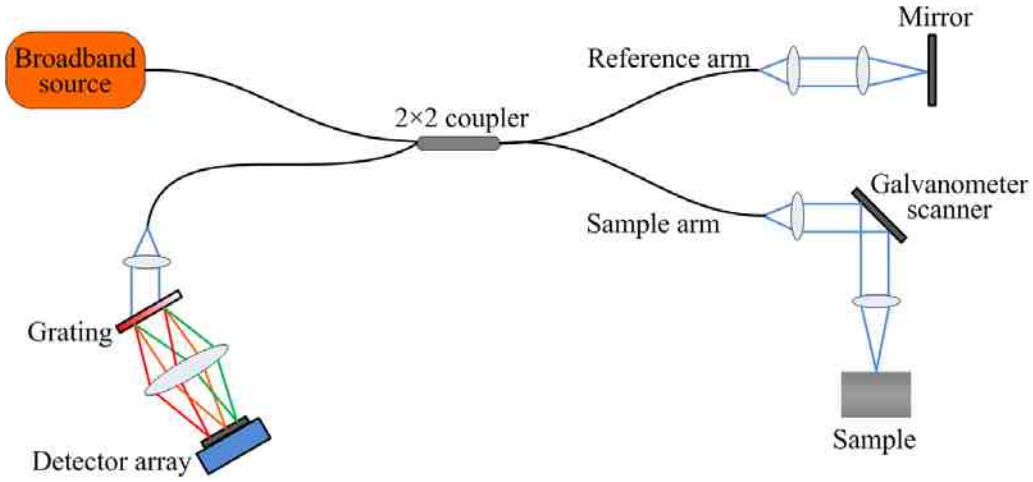

Fig. 1.3. Schematic of a SD-OCT system.

Fig. 1.3 shows a schematic of a generic spectral domain OCT (SD-OCT) system [36, 37]. Light from a low-coherence broad band light source (typically superluminescent diode (SLD)) is coupled into a 2×2 fiber coupler which is utilized as a fiber-based Michelson interferometer. The incident optical power is split by the fiber coupler into the sample arm and the reference arm. Light exiting the reference arm fiber is reflected back by the reference mirror and redirected to the fiber coupler. Light exiting the sample arm fiber is collimated, scanned by a galvanometer scanner mirror pair, and then is focused to the sample. The backscattered light signal from the tissue is collected by the same lenses and the galvanometer scanner mirror pair back to the fiber and to the fiber coupler. The backscattered light from sample and returning light from reference mirror are recombined in the fiber coupler resulting in spectral dependent interference pattern that is revealed by the optical spectrometer in the SD-OCT system. Partial return light coupled to the light

source is ignored by the light source if it does not introduce light source instability. For a sensitive light source, an optical isolator may be used to block the return light to the light source.

Nowadays, OCT system is large, unwieldy, and expensive which contains many bulk optical components such as beam splitters, reference arm optics, and optical spectrometers. Fig. 1.4 shows the bulky SD-OCT system with the SLD light source, the spectrometer, the reference arm, and the scanner in our lab. The most bulky component is the optical spectrometer that often occupies a large portion of the SD-OCT system. Using bulk optics based SD-OCT could not yield a compact book size system for portable clinical applications.

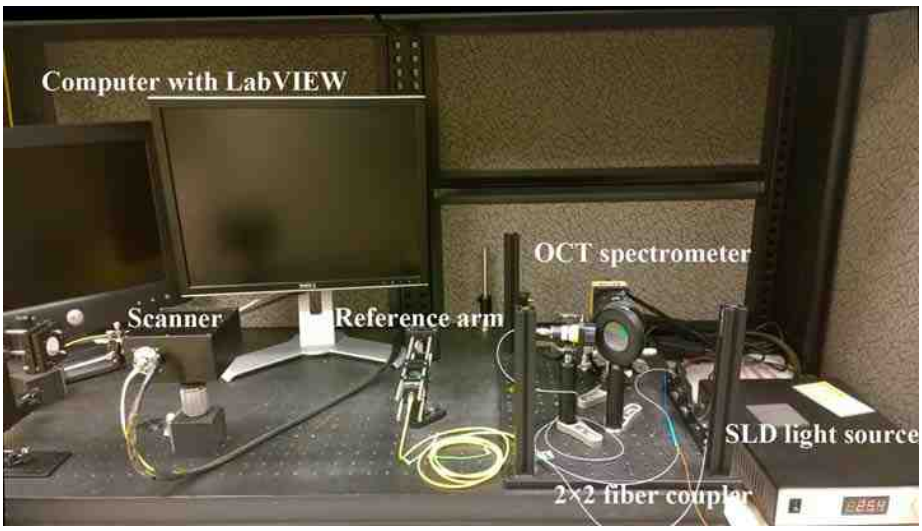

Fig. 1.4. Bulky SD-OCT system in our lab showing optical spectrometer and reference arm optics.

From the SD-OCT system configuration, besides the semiconductor SLD light source, the galvanometer scanner, and focusing lenses at the sample arm, many SD-OCT system components including the 2×2 coupler, reference arm, and optical spectrometer could be

realized by using integrated optics. It is thus of our interest to explore the design of the integrated optics version of the optical spectrometer for the SD-OCT in this dissertation.

1.2 Polymer Waveguide Devices

1.2.1 Selection of Polymer for Our Integrated Optics

The most widely used materials for OICs are silica, semiconductor, $LiNbO_3$, and polymers. Silica, Silicon, other semiconductor, and $LiNbO_3$ are excellent substrate candidates for the fabrication of integrated optics. Silicon and other semiconductors usually have high waveguide core refractive indices that allow sharp waveguide bending and thus can realize ultra-compact waveguide device array on a small area. However, some expensive lithography technique such as deep-ultraviolet (UV) or E-beam lithography is required for waveguide nanowire fabrication due to the submicron cross section. The waveguide also suffers from high propagation loss because of large scattering due to the surface roughness [38]. $LiNbO_3$ and some semiconductors offer high electro-optic coefficients and can support the realization of functional electrically controlled devices for applications such as modulation and switching. Silica has very low light propagation loss, high coupling efficiency with single-mode fiber, and high stability of fabricated integrated optics device [39]. However, a large bending radius is always inevitable due to its low refractive index contrast, which is not available for high integration density and compact optical devices.

Despite these characteristics, these materials have a common drawback that is the substrate is ridged and not bendable and have fabrication process compatibility problem

with printed electronic circuit boards. In other words, they may not be suitable to serve as a flexible optical interconnect ribbon on top of the circuit board.

Polymer waveguide on the other hand offers the possibility of lower cost fabrication and soft lithography replication [26, 40, 41]. It is considered as a promising candidate to address the requirement of optical interconnects especially on the board level and card-to-backplane level [42-47]. Polymer has increased the compatibility with printed circuit boards and flexible substrates [45, 48-51]. It also has a large transparent window from the visible to infrared range of light, which is compatible for wide range of applications. Besides, the refractive index of polymeric material can be easily and widely adjusted through the synthesis processing and heat treatments. Polymer material can also be synthesized to offer a lot of special characteristics, such as thermo-optic effect [52], electro-optic effect [53], photochromic effect [54, 55], and light emission [56], facilitating the formation of many active optical devices.

The quality of the polymer waveguides used to form the transmission medium is central to a polymer-based optical link technology, which is characterized by the optical propagation loss of the polymer waveguides [57]. It comprises the intrinsic absorption loss of the polymer material and the waveguide losses due to fabrication imperfections and surface roughness. Fig. 1.5 presents a comparison of the propagation losses of several reported polymer waveguides with different polymer materials at 850 nm wavelength, including OE4140 (from Dow Corning) [11], WIR 30 Series (from ChemOptics) [58], SU-8 (from MicroChem) [59], and some other polymer materials [51, 60]. It can be concluded that polymer waveguide can offer low loss for optical interconnect applications.

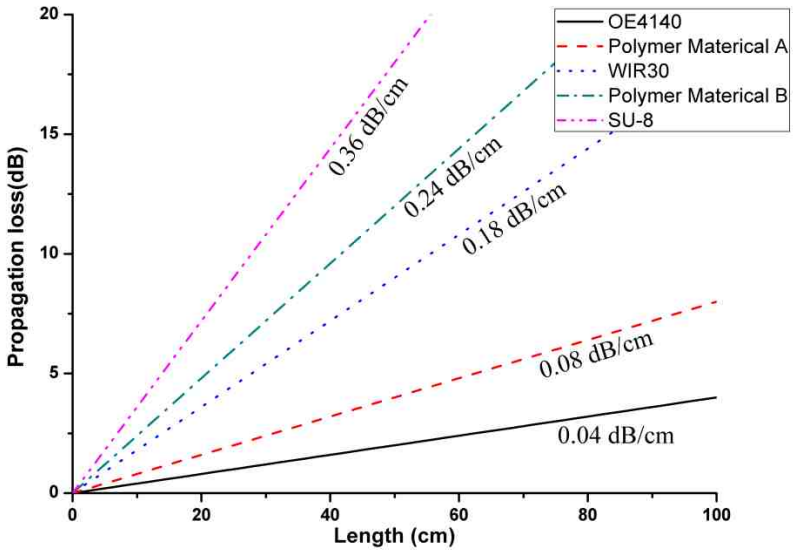

Fig. 1.5. Propagation losses of several reported polymer waveguides with different polymer materials.

In this dissertation, we select polymer waveguide to address the optical interconnection and wavelength separation applications. Our design and fabrication show that polymer based integrated optics is effective for optical interconnection and wavelength demultiplexing.

1.2.2 Fabrication of Polymer Waveguide

Polymer waveguide devices can be fabricated by many techniques, including laser direct writing [61], reactive ion etching [61], electron-beam lithography [62, 63], photolithography [64, 65], and soft lithography [66]. Laser direct writing has the advantage of allowing rapid prototyping without a process of a mask production [67], however it is limited by writing speed and materials selection. Reactive ion etching involving many processing steps is complex and time consuming. Electron-beam lithography is specially used for high-resolution nano/microstructures fabrication, which are time consuming and costly.

Photolithographic process has obvious advantageous over these techniques, which is a powerful and dominant technique for microfabrication, especially in the integrated circuit fabrication [68]. It is suited to form structures of radiation-sensitive materials such as photoresists on the flat glass or semiconductor surfaces [66]. However, there are a few disadvantages of photolithography such as low suitability for nonplanar surface patterning and limitation of photosensitive materials selection, which restricts its application. Soft lithography is an alternative and non-photolithographic microfabrication method. It uses a patterned elastomer as a stamp or mold to generate microstructures, therefore it is a fast and inexpensive replication technique; it can be used for three-dimension structure and nonplanar surface fabrication; and it can use a wide set of materials.

In the dissertation, the polymer waveguide devices such as PCG with the waveguide channel size down to a few micrometers are fabricated by conventional UV lithography. The polymer waveguides with integrated mirrors with the waveguide channel size of tens of micrometers are achieved by vacuum assisted microfluidic (VAM) soft lithographic techniques. The master pattern for VAM soft lithography is fabricated by a prism-assisted inclined UV lithography [69, 70].

VAM [71-73] is a new microfluidic based replication technique which can be widely used for polymer optical waveguide fabrication. It can be utilized to improve the performance of imprinted devices by eliminating the residue planar layer and accomplish complex devices incorporating different materials in the same layer.

Prism-assisted inclined UV lithography can be used for the fabrication of 3D microstructures in a photoresist, such as waveguide with 45° integrated mirrors. A prism

is used as a refractor to deflect the incident UV light and expand the exposure beam angle range in the resist film. The sample internal surface reflection of the exposing UV light can facilitate the fabrication of symmetric structures. Prism with multidirectional side surfaces can be used to achieve one-step exposure fabrication of multidirectional slanted structures.

1.2.3 Polymer Waveguide with Integrated Mirrors

Many optical interconnect architectures have been reported, such as card-to-backplane optical interconnects [44], backplane optical data busses [46], and multilayer optical interconnected circuits [45, 74-76]. Polymer waveguides with 45° micro-mirrors play a significant role in these architectures for surface normal coupling. The 45° slanted waveguide surfaces can be constructed by various techniques, such as sawing [77], laser ablation [78], reactive ion etching [79], ultra-precision machining [75], and deep proton writing [80]. The common disadvantage of these techniques is the complex multi-step fabrication process that the mirror fabrication is separated from the waveguide fabrication. For photolithography fabrication of the inclined surface mirror, the slanted surface angle is limited due to refractive beam path bending in the photoresist. It is possible to construct the 45° inclined surfaces by immersion of photoresist in an index matching liquid, such as water, heptane, or glycerol [81-84]. However, it demands a sample settlement time in the index matching liquid to avoid bubble formation and an uneven liquid surface. The presence of some index matching liquid such as water may also affect the UV exposure properties of the photoresist. Prism-assisted inclined lithography technique [69, 70, 76] can be utilized to achieve 45° slanted surfaces without immersing the sample in an index matching liquid.

In this dissertation, we will show an effective technique to fabricate the polymer waveguide with slanted surfaces that can serve as integrated mirrors.

1.3 Dissertation Overview

This dissertation summarizes our resent research works on polymer waveguide based optical interconnects, spectral separation elements for WDM, and waveguide optical spectrometer. We also summarize related fabrication techniques.

In Chapter 2, multiple imprint techniques of soft lithography are discussed. Since we have selected polymer for our device implementation to support optical interconnects and spectral separation (WDM and optical spectrometer), the polymer waveguide device fabrication can be done by conventional UV lithography and VAM soft lithography techniques. The conventional UV lithography have been well documented by various publications in the open literatures [65, 67] and will not be detailed here. In this chapter, the VAM technique will be discussed in greater detail. It can be utilized to improve the performance of imprinted devices by eliminating the residue planar layer and accomplish complex devices incorporating different materials in the same layer. The polymer waveguide resins have been successfully synthesized, which have the properties of being low enough in viscosity for microfluidic propagation through the mold channels, having an adjustable refractive index for the core and cladding layer, and the capability of curing when exposed to UV light.

In Chapter 3, a prism-assisted inclined UV lithography technique is introduced for the fabrication of 3D microstructures. Slanted structures with exposure angles ranging from 0° to 60° in SU-8 photoresist have been easily achieved without immersion in the index

matching liquid. The fabrication process of multidirectional slanted structures can be simplified by one-step UV exposure using a prism with multidirectional side surfaces such as a corner prism and a cone prism. This method has also been utilized to fabricate master pattern of waveguide structures with 45° slanted surfaces for optical interconnects as discussed in Chapters 4 and 5.

In Chapter 4, we present the fabrication of flexible polymer waveguide with 45° integrated mirrors using the VAM soft lithography technique for optical interconnects. Varying the inclined surface depth can result in different needed light coupling efficiency. The fabricated polymer waveguides with 45° mirrors demonstrated a propagation loss of -0.24 dB/cm, and a coupling efficiency of 75% and 38% for full and half mirrors, respectively. Such passive optical interconnection is useful for optical interconnect link with fixed point-to-point topology and shared bus topology. The more energy efficient method is using dynamic optical interconnects system to facilitate ON/OFF control of the interconnect link, as discussed in Chapter 5.

In Chapter 5, a dynamic card-to-backplane optical interconnects system is demonstrated based on polymer waveguides with tunable optofluidic couplers. The operation of the tunable optofluidic coupler is accomplished by controlling the position of air bubbles and index matching liquid in the perpendicular microfluidic channel for refractive index modulation. The dynamic activation and deactivation of the backplane optofluidic couplers can save the optical signal power for card-to-backplane optical interconnection. 10 Gbps eye diagrams of the card-to-backplane optical interconnect link have been demonstrated showing the high performance of the interconnect structures.

In Chapter 6, we present our design and fabrication of PCG for the waveguide WDM system. With an innovative design, we have achieved a flat spectral response for the WDM making it less sensitive to small spectral shift which is common in a practical system. The flattened spectral response to spectrally separated channels is accomplished by using an optimized multi-mode interference (MMI) coupler as the input aperture to the PCG. The WDM device with improved communication channel capacity has small footprint and can be practically used in the optical interconnect especially for external interconnection to optical fiber network.

The same PCG design with a larger footprint (500 mm^2) could support larger channel counts for waveguide optical spectrometer that can be used in the integrated optics version of SD-OCT system. We designed a 200-channel PCG spectrometer with 0.5 nm channel spacing and a 1024-channel PCG spectrometer with 0.1 nm channel spacing for SD-OCT application. The simulation results show that they both have low crosstalk, small channel loss, and good uniformity, with chip size of 3 cm × 3 cm and 8 cm × 8 cm, respectively. The maximum imaging ranges are 0.85 mm and 4.3 mm with 9.47 μm axial resolution in theory, respectively. The design of PCG spectrometers moves an important step toward on-chip SD-OCT system. An alternative solution to compact and portable SD-OCT is designing a compact spectrometer by minimizing the beam expansion perpendicular to the spectral dispersion plane as originally planned by using integrated optics. By containing the beam within 3 mm to the plane in free space, the optical spectrometer is found effective and can minimize the insertion loss and crosstalk associated with waveguide devices. This is a valid compact packaging approach by only

increasing effective device thickness from 1 mm (substrate with waveguide) to about 3 mm beam size perpendicular to the plane.

Chapter 2

Lithography Fabrication of Polymer Waveguides

Polymer waveguides and devices using polymer material are attractive because of their potential application in optical interconnection and integrated optics. It offers lower cost, high signal transmission, and increased compatibility with printed circuit boards and flexible substrates [40, 67, 85].

Many techniques can be used for polymer waveguides fabrication, such as laser direct writing, reactive ion etching, and electron-beam lithography. However, these methods are time consuming, low yield, and high cost [65]. Photolithography is a low cost, high efficient and high yield rate process. It is a powerful and dominant technique for microfabrication, especially in the integrated circuit fabrication. It is suited to form structures of radiation-sensitive materials such as photoresists on the flat glass or semiconductor surfaces [66]. However, its applications are also restricted owing to low suitability for nonplanar surface patterning and limitation of photosensitive materials selection. Soft lithography is an alternative and non-photolithographic microfabrication method which can avoid many of these problems. It uses a patterned elastomer as a stamp or mold to generate microstructures, therefore it is a fast and inexpensive technique; it can be used for the 3D structure and nonplanar surface fabrication; and it can utilize a wide set of materials [86].

Polymer materials exhibit high transparence, good thermal stability, easy processing, and good adhesion on a wide range of substrates [65]. Two kinds of custom made

materials have been synthesized with low viscosity and well-controlled refractive indices for VAM technique application.

2.1 Photolithography Fabrication of Polymer Waveguides

The photolithography is a powerful and dominant technique for microfabrication and can be used for polymer waveguides fabrication. Fig. 2.1 schematically illustrates the process of photolithography fabrication on a flat substrate.

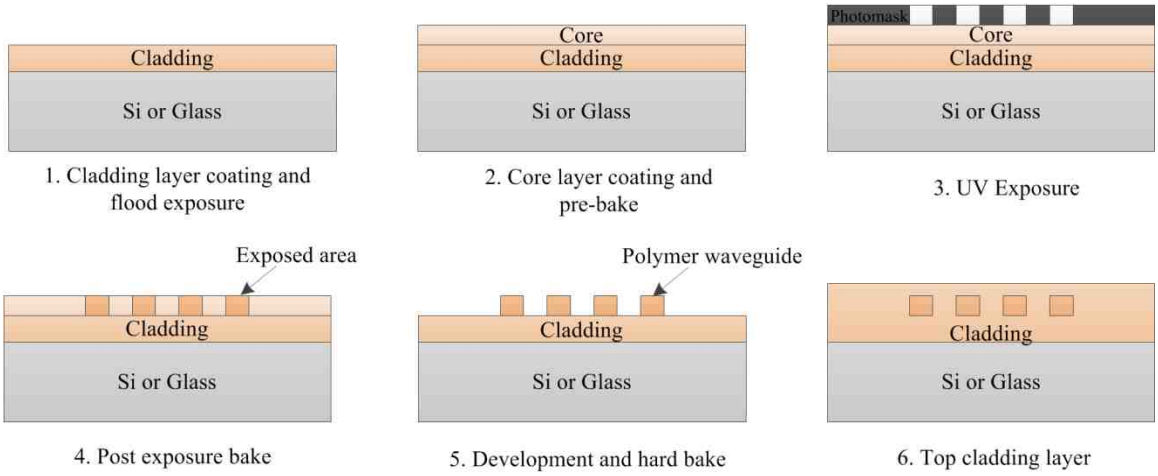

Fig. 2.1. Schematic illustration of the process of photolithography fabrication.

A cladding layer is first spin coated on a cleaned substrate and cured by flood UV exposure. The cladding layer should have lower refractive index compared with the core layer and be thick enough to avoid waveguide beam leakage to the substrate. The core layer polymer is then formed on the top of cladding layer by spin-coating. The substrate with core and cladding layer is pre-baked on a hotplate to evaporate the solvent. Then the patterns on the photomask are transformed to the core layer by photolithography. The substrate with the exposed polymer thin film is then post-baked to finish the polymer cross-linking process. Following development and rinsing, the final polymer waveguide

structures are obtained. Hard baking can be used to stabilize the polymer waveguide and smoothen the waveguide sidewalls. A top cladding layer with lower refractive index than the waveguide core can be spin coated and UV cured to keep the polymer waveguide patterns inside, without exposing to air, for protecting the polymer waveguides and related optical devices against environmental dusts and finger print related handling damages.

2.2 Vacuum Assisted Microfluidic Fabrication of Polymer Waveguides

Aforementioned contact or projection photolithography is limited to fabrication on flat substrates. Soft lithography is a fast and convenient replication technique that can realize patterned structures on non-flat substrates such as flexible ribbons [87]. For soft lithography, an elastomeric stamp or mold is used for pattern definition from a master with relief structure. A master should be fabricated first by microlithography methods such as photolithography, micromaching, or electron-beam lithography. After the mold fabrication, the defined pattern can be easily transferred and replicated according to practical application requirements.

Poly(dimethylsiloxane) (PDMS) elastomer is widely used for stamp or mold in soft lithography because of its good chemical stability, good thermal stability, low interfacial free energy, and high optical transparency down to 300 nm. The PDMS pre-polymer resin we used is generated by Sylgard 184 (Dow Corning) with an elastomer resin part and a photoinitiator part, which are vigorously mixed with a 10:1 ratio.

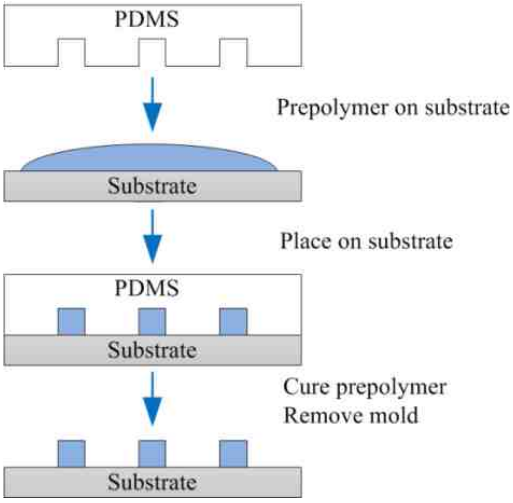

Fig. 2.2. Schematic diagram of theoretical μTM fabrication process.

One of the most prominently used methods in soft lithography is microtransfer molding (μTM), which is convenient and low cost and can produce high quality side walls [6, 88]. Fig. 2.2 shows a schematic diagram of theoretical μTM fabrication process. By pressing the elastomeric mold on a non-hardened polymer layer followed by UV curing the polymer and removing the mold, we can achieve a high quality structural pattern replication, for the purpose of polymer waveguide fabrication.

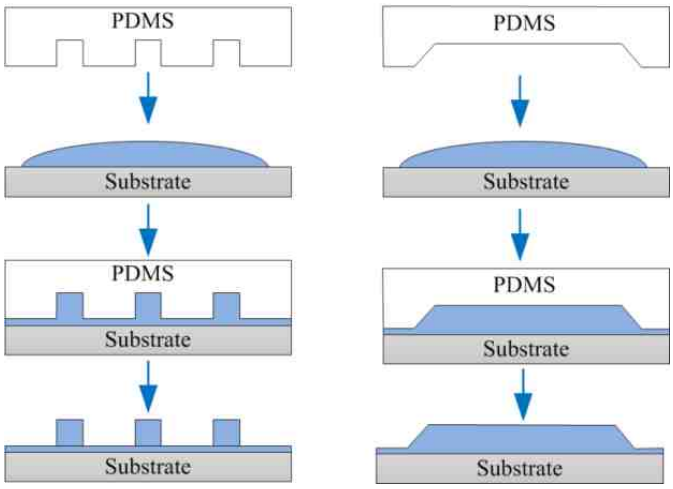

Fig. 2.3. Schematic of practical μTM fabrication process with remnant planar layer.

Because the mold pressing cannot fully expel the polymer resin in area as required, this method often results in a remnant planar layer between the anticipated optical waveguides and the substrate [86] that degrades the waveguide mode confinements, introduces extra propagation loss and crosstalk, as shown in Fig. 2.3. If the waveguide has a 45° integrated mirror, the presence of the remnant planar layer will also greatly decrease mirror coupling efficiency.

VAM [71-73] is a new microfluidic based replication technique introduced by our group that can be widely used for polymer optical waveguides fabrication. It can be utilized to improve the performance of imprinted devices by eliminating the residue planar layer and accomplish complex devices incorporating different materials in the same layer. The VAM soft lithography fabrication of polymer waveguides requires a PDMS mold with microfluidic hollow channel structures to guide the polymer resin flow. Usually, there are an inlet hole and an outlet hole located on opposite side of the microfluidic hollow channel structure. The UV curable resin can be injected to the inlet hole and vacuum suction can be applied to the outlet hole assisting the resin flow inside the hollow channel.

Fig. 2.4 schematically shows the VAM fabrication process. A master pattern with the structures of channel waveguides is first fabricated. A PDMS mold with microfluidic hollow channels which is a negative imprint from the master pattern can be subsequently created, as shown in Fig. 2.4(a). The desired waveguides are then realized via VAM soft lithography using the synthesized UV curable resins as illustrated in Fig. 2.4(b).

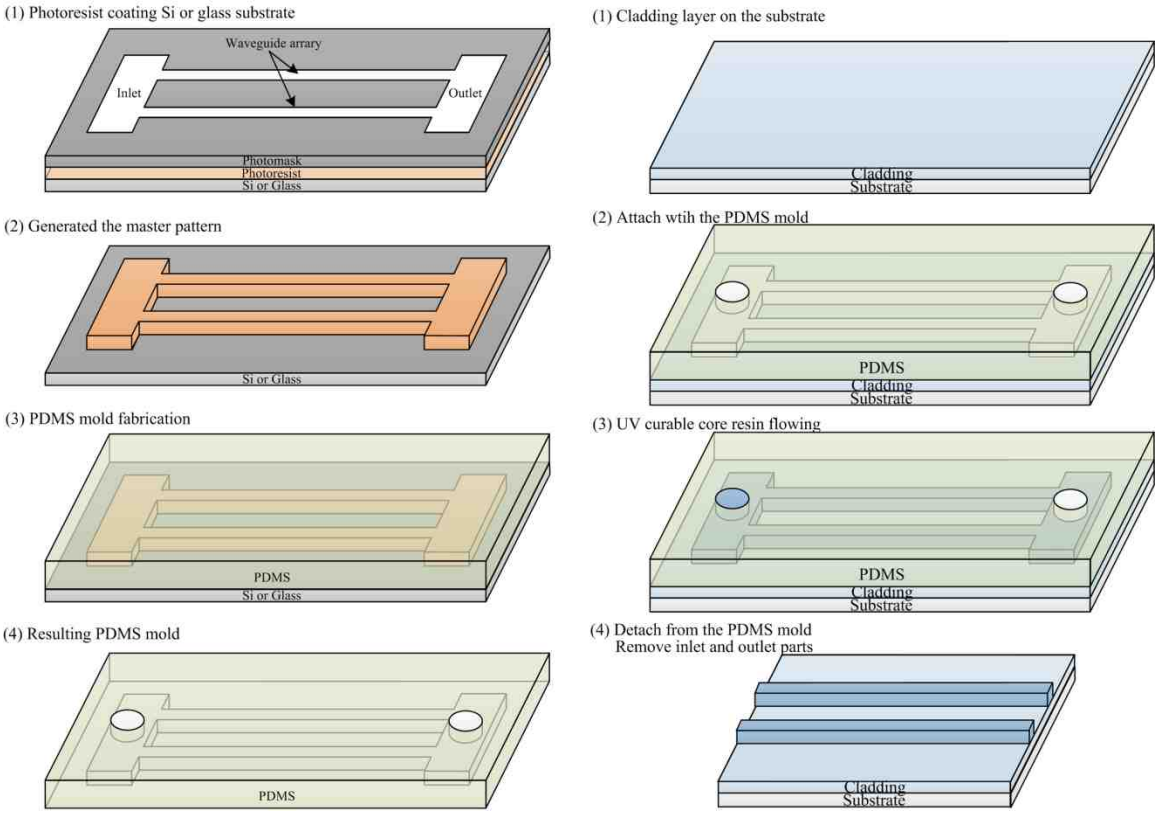

Fig. 2.4. Schematic illustration of the whole process of (a) PDMS mold fabrication and (b) polymer waveguide imprint.

2.2.1 Master and PDMS Stamp Fabrication

The key element in VAM technique is an elastomeric stamp or mold with relief structure defined by a master pattern. The master should be fabricated first by microlithography methods such as photolithography, micromaching, or electron-beam lithography. Fig. 2.5 shows the master fabrication using UV lithography on silicon wafer or glass. The fabrication of the master with slanted structures can be realized by the prism-assisted inclined UV lithographic method, to be detailed in chapter 3.

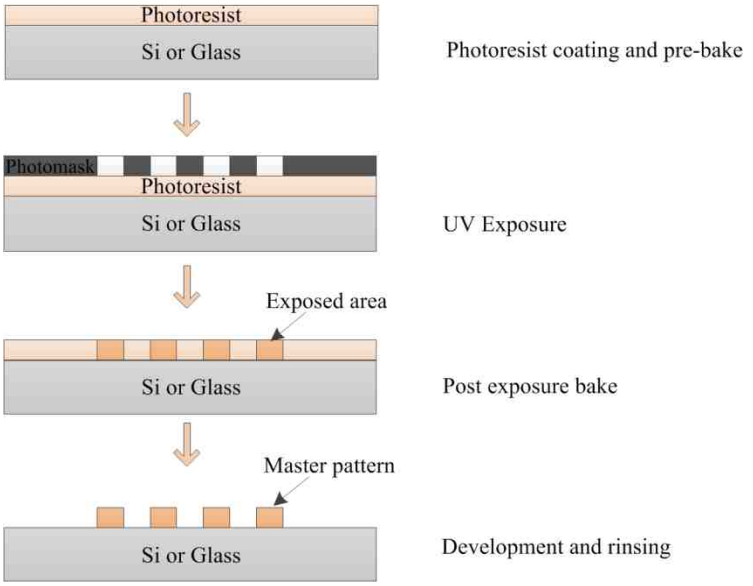

Fig. 2.5. Schematic of the fabrication process of the master.

For master pattern fabrication, a photoresist is first spin coated on a silicon or glass substrate. The substrate with photoresist layer is pre-baked on a hotplate to evaporate the solvent. Then the patterns on the photomask are transformed to the photoresist layer by photolithography. The substrate with the exposed photoresist thin film is then post-baked to finish the polymer cross-linking process. Following development and rinsing, the master pattern is obtained. The master pattern cannot be directly used for VAM soft lithography because of the high viscosity of the photoresist. We must use it to generate a stamp with surface relieve patterns.

The fabricated master is then transferred to a negative replica PDMS stamp. The liquid PDMS is poured on the generated master which is encased by aluminum freezer tape, as shown in Fig. 2.6. It is left to settle for 2 hour to eliminate bubbles and then baked at 85°C for 3 hours. After that, the PDMS mold is peeled off and inlet and outlet holes are then subsequently drilled for VAM lithography. Fig. 2.7 presents an image of a fabricated PDMS mold, as an example.

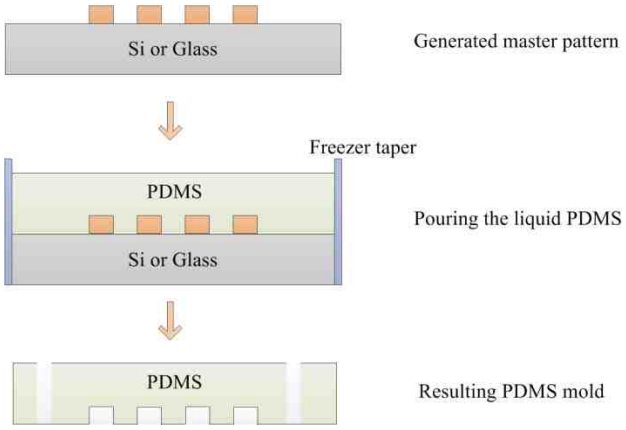

Fig. 2.6. Schematic of the fabrication process of the PDMS mold.

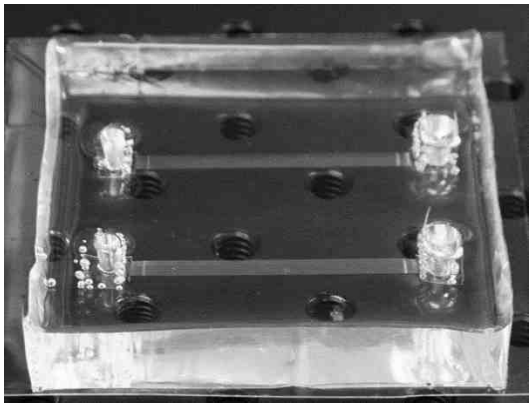

Fig. 2.7. Image of a fabricated PDMS mold.

2.2.2 VAM Fabrication of Multi-mode Polymer Waveguides

The schematic process of VAM fabrication of multi-mode polymer waveguide is given in Fig. 2.8. First, a cladding resin layer is spin coated on a substrate such as silicon, glass, printed circuit board, or flexible plastic film, followed by UV curing. The PDMS mold is then placed in conformal contact with the cladding layer. The UV curable core waveguide resin is injected into the inlet hole, and suction is provided to the outlet hole using a vacuum pump to assist the microfluidic flow of the resin in the PDMS channels. Following UV curing, the PDMS mold is removed to reveal the channel waveguides. The

inlet and outlet tubes are then removed. With careful use, the PDMS mold can be good for more than 100 replications that can reduce the cost of device fabrication.

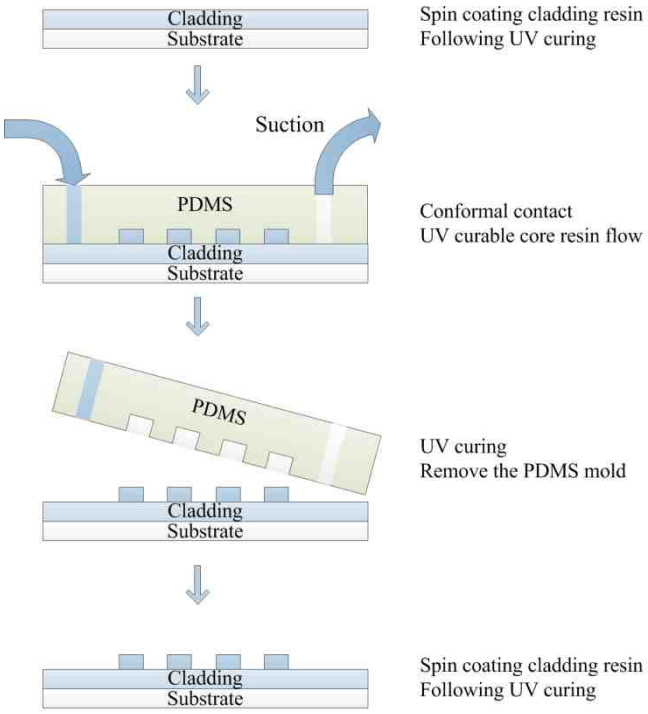

Fig. 2.8. Schematic process of VAM fabrication of polymer waveguides.

The image of an experimental setup of VAM fabrication is shown in Fig. 2.9. Fig. 2.10 shows a scanning electron microscope (SEM) image of imprinted polymer waveguides with quite smooth side surfaces.

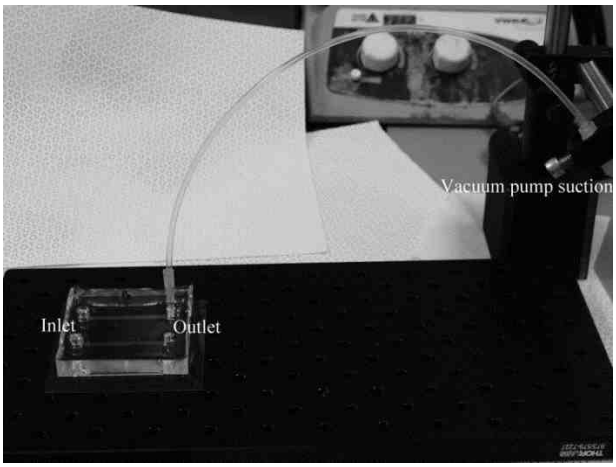

Fig. 2.9. Image of experimental setup of VAM fabrication.

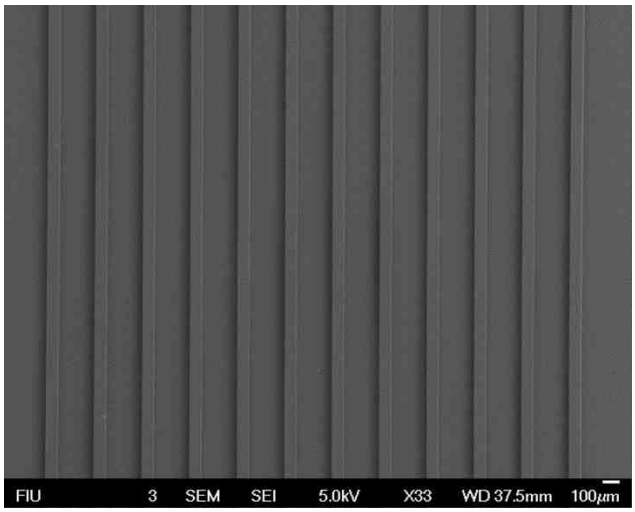

Fig. 2.10. SEM image of imprinted polymer waveguides.

2.2.3 VAM Fabrication of Single-Mode Polymer Waveguides

The VAM technique is relatively easy to fabricate multi-mode channel waveguides with length of over 30 cm, because the relatively large waveguide cross-sectional dimension (larger than 20 μm × 20 μm) can facilitate easy UV curable core waveguide resin flows in the guiding PDMS flow channels [89]. However, it is difficult to produce single-mode channel waveguide with a small cross-sectional dimension (smaller than 10 μm × 10 μm). Our experiment has demonstrated that the microfluidic flow length is quite short (~2 mm) at such small cross-sectional dimension due to the cogging caused by the viscosity of the resins [90].

Sectional flow tapers has been introduced into the microfluidic channels to prevent clogging and overcome this viscosity limitation. Fig. 2.11 shows a schematic of the PDMS mold for the VAM system, which consisting of a narrow flow channel, two wide flow channels, and sectional flow tapers. The narrow flow channel is the desired single-mode waveguide channel and two wide flow channels are parallel surrounding the narrow

channel. The perpendicular sectional flow tapers was designed to connect the narrow channel with the wide flow channels.

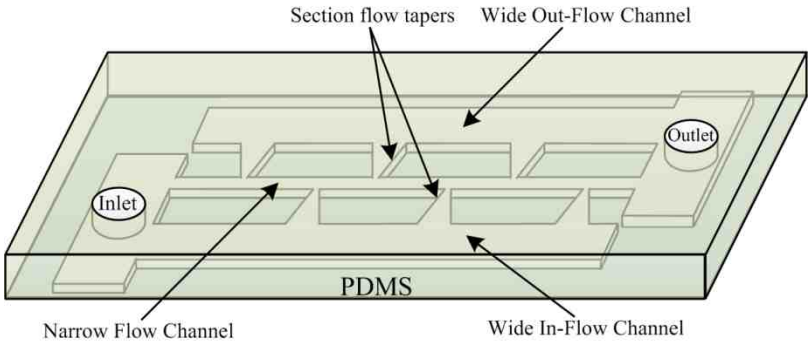

Fig. 2.11. Schematic of the PDMS mold for the VAM system.

The UV curable polymer resin flows through the structure starting from the inlet hole. The presence of wide flow channels supports the flow of the resin through the VAM structure from inlet to wide in-flow channel, to narrow flow channel, to wide out-flow channel, and finally to outlet. Because the resin may have trouble fully propagating through the narrow flow channel even under vacuum assistance, the added sectional flow tapers can help fill the narrow channel with the resin section by section.

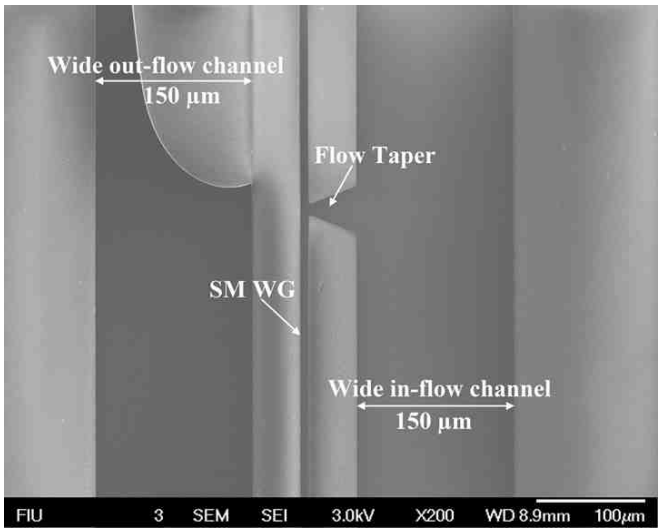

Fig. 2.12. SEM image of the fabricated single-mode channel waveguide [90].

Fig. 2.12 presents the SEM image of the fabricated single-mode channel waveguide with length of 30 mm and cross section dimension of 7 μm × 7 μm by VAM technique. The achieved waveguide length of 30 mm is significantly longer than the previously demonstrated 2 mm without using the sectional flow tapers.

2.2.4 VAM Fabrication of Multi-section Polymer Waveguides Incorporating Different Materials

Almost all lithography fabrications can only realize desired patterns of same material on a substrate. For the fabrication of polymer waveguides, they can only fabricate waveguide patterns using a single core polymer resin. The waveguide core can be passive, light sensitive, electro-optic, light emitting, or light sensing, but not in combination. It is not possible to fabricate different polymer waveguides on the same substrate because of current lithography fabrication limitation.

The introduction of VAM fabrication, on the other hand, alleviates such lithography fabrication limitation. Different polymer resins can be used in different portion of the waveguide on the same substrate by using different microfluidic channels. It is thus possible to fabrication polymer waveguides of passive, light sensitive, electro-optic, light emitting, and light sensing on the common substrate to demonstrate monolithically integrated functional system.

To demonstrate polymer waveguides with different materials, we can inject different resins into different inlet holes and fill different microfluidic hollow channels with different resins. Fig. 2.13 shows a design of the VAM system for the fabrication of polymer waveguides with two different waveguide core material sections. Each section has an inlet hole, an out let, and a microfluidic hollow channel. A waveguide device filled

with different polymer resins have been realized as shown in Fig. 2.14. Here, one waveguide is a UV cured passive polymer waveguide while the other waveguide is UV cured light sensitive waveguide that can support the fabrication of waveguide holographic gratings for filtering and all-optical switching functions. The technique can be extended to include other functional device elements on the common substrate.

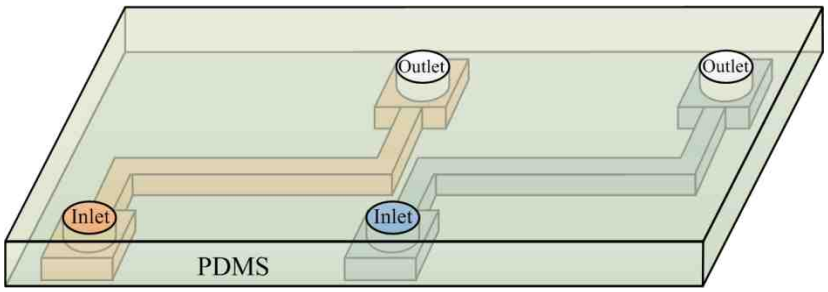

Fig. 2.13. A design of the VAM system for multi-section polymer waveguides fabrication.

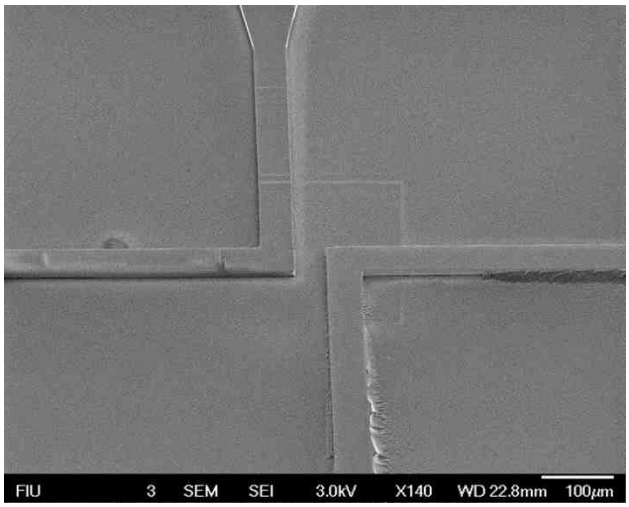

Fig. 2.14. SEM image of the fabricated multi-section polymer waveguides [91]

2.3 Synthesized Polymer Waveguide Resins Supporting Soft Lithography Fabrication

To support the VAM fabrication of polymer waveguides for optical interconnection, the polymer resin must have proper refractive index control, low propagation loss at the

desired interconnect wavelength, UV light sensitive for curing after VAM channel filling, and with controlled viscosity. In addition, if we need the polymer waveguide to be light sensitive, we should also be able to add suitable light sensitive inhibitor. The material design and synthesis is thus an important issue.

The commercially available UV curable resins cannot meet all these requests. We have thus custom developed UV curable resins for both core and cladding resins with low viscosity and controllable refractive index. The procedure and chemicals for synthesizing both core and cladding resins are listed below [89, 90].

1. 2,6-Di-t-butyl-4-methyl-phenol was first mixed in a vial with Bis(3,4-epoxy cyclohexylmethyl) adipate for one hour.
2. Poly[(o-cresylglycidyether)-co-formaldehyde] was then added and mixed until all the crystals dissolved.
3. 3,4 Epoxycyclohexyl methyl-3,4 – epoxy cyclohexane carboxylate was then added and mixed for one hour.
4. Finally, 3-glycidoxyprpyl trimethoxy silane, UVI-6992 Cyracure, and 1,6 Hexanediol diacrylate, tech 800 were added and mixed together until a homogeneous low viscosity solution was formed.

All of the above mentioned steps were done at a temperature of 65 °C, while being magnetically stirred at 300 RPM. We can adjust the refractive index of the synthesized UV curable resins based on the quantity of the material 1,6 Hexanediol diacrylate, tech 800. The refractive indices of synthesized materials were measured by an ellipsometer from Angstrom Sun Technologies, which show a wide range from 1.50 to 1.515 at 850 nm wavelength.

Fig. 2.15 shows the spectral transmittance of the UV curable core resin as it was measured using a spectrometer (Ocean Optics USB 2000) indicating a very high transmittance in the visible to NIR spectral region.

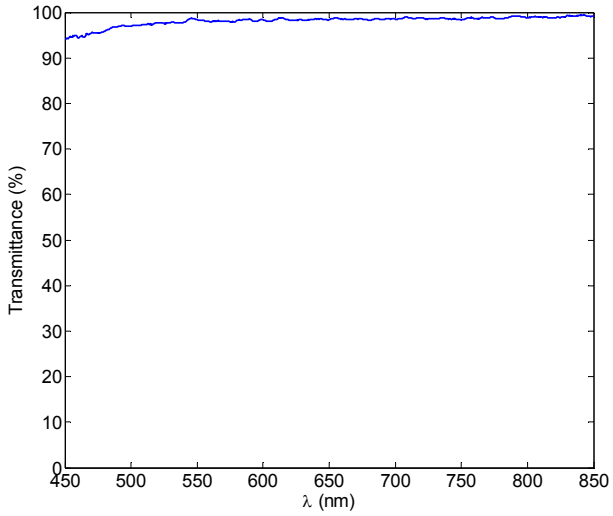

Fig. 2.15. The transmittance properties of the synthesized UV curable core resin of 15 μm thickness [90].

To support light sensitive multi-sectional waveguide fabrication discussed in Sec. 2.2.4, special UV curable resin is synthesized to facilitate the fabricated waveguide to be light sensitive for instant holographic grating recording. The preparation method for the UV cured light sensitive waveguide resin is slightly different from the normal core waveguide resin and is listed as follows [91]:

1. Core waveguide resin was first mixed with lauryl methacrylate and methyl methacrylate (1/1 wt) at room temperature for one hour.
2. Then, styrene and Disperse Red 1 were added and ground in a ceramic mortar for about 15 min. Following that, crosslinking agent divinyl benzene was added.

3. Finally, trace amount of 3-(trimethoxysilyl)-propyl acrylate and RM 257 were added and then mixed together until a homogeneous flowable mixture was formed, and kept at ~4 °C.

We used the ellipsometer to evaluate the refractive index change induced by flood illumination with a 532 nm laser beam. The sample was prepared by spin coating the light sensitive resin followed by UV curing at 25,000 mW/cm^2 illumination intensity for 10 min. The planar film thickness is determined by Tencor Alpha Step 100 at film and non-film boundary to be 14.5 μm. The measured film refractive index at 850 nm wavelength without 532 nm laser exposure is 2.1364. Upon continuous laser exposure the refractive index is similarly determined. The relationship between the refractive index change and laser exposure intensity is given in Fig. 2.16 showing that the refractive index change as large as 0.0014 can be achieved.

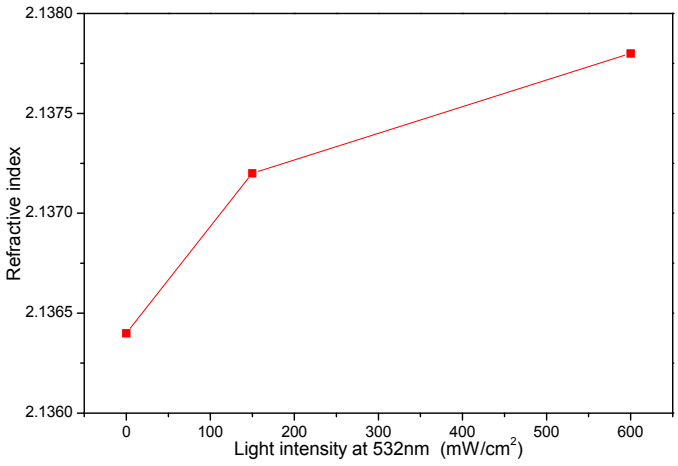

Fig. 2.16. The refractive index change of light sensitive resin.

The recording light sensitivity is revealed through the absorption spectrum of the UV cured light sensitive resin as shown in Fig. 2.17. Clearly, blue to green light wavelengths

are all effective for the holographic recording while the resin is transparent to the 850 nm laser beam. The present sample film thickness is ~ 40 μm.

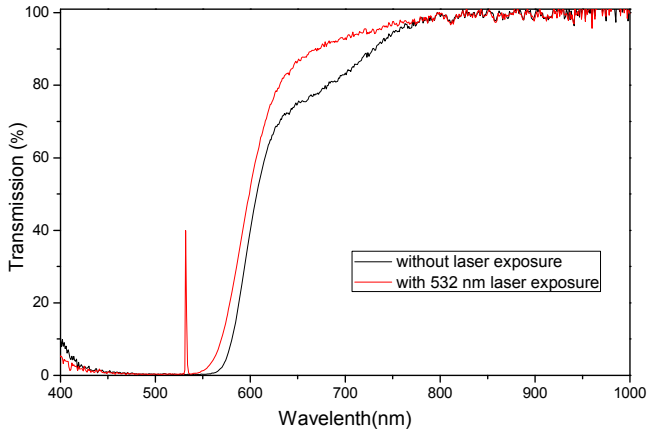

Fig. 2.17. The absorption spectrum of the UV cured light sensitive resin. The sharp peak at 532 nm is due to the laser beam.

2.4 Summary

Polymers are selected for our device implementation to support optical interconnects and spectral separation (WDM and optical spectrometer). Polymer waveguides can be fabricated by conventional UV lithography and VAM lithography techniques. The VAM technique for high quality waveguide fabrication has been discussed in greater detail in this chapter. It can improve the performance of the imprinted devices by eliminating the residue planar layer and accomplish complex devices incorporating different materials in the same layer. The single-mode polymer waveguide can also be fabricated by introducing the sectional flow tapers. Multi-section polymer waveguides of different waveguide core materials have also been demonstrated.

We have also reported the composition and procedures for preparing the polymer waveguide resins to support the VAM fabrication. The polymer resins must be refractive index controlled, low absorption loss at interconnect wavelength, UV curable, low viscosity, and if desired can be made light sensitive.

With the polymer resins and lithography fabrication preparations, we need to further explore the fabrication of angled waveguide surfaces for the realization of integrated waveguide mirrors to support the surface normal optical coupling which is critical to card-to-backplane optical interconnects. In Chapter 3, we will discuss our work on fabricating angled surfaces and 3D microstructures by the prism-assisted inclined UV lithography.

Chapter 3

Prism-assisted Inclined UV Lithography for 3D Microstructure Fabrication

Angled surfaces in waveguides are required in card-to-backplane optical interconnection. It can provide the needed surface normal light coupling. The fabrication of slanted surface structures are also important in the realization of various 3D microstructures to support applications in optical display, optical memory, medical fluidic filtering devices, drug delivery devices, solar energy devices, and photonic crystal based light filtering/routing devices.

The fabrication of microstructures has traditionally been performed by lithography including photolithography, laser direct write maskless lithography, e-beam lithography, deep-UV lithography, X-ray lithography, and soft lithography. Traditional photolithography, laser direct write maskless lithography, and gray-scale lithography are suitable for micro-structural patterning. E-beam lithography, deep-UV lithography and X-ray lithography employing shorter wavelength beams can help improve pattern resolution for fabrication of finer scale nano-structures. Contact lithography including soft lithography and nano-imprint lithography offers capability of higher resolution nano-structure fabrication. However, most of these existing lithography tools are limited to the fabrication of two-dimensional (2D) micro- and nano-structures. Multilayer 2D patterning using the photo and e-beam lithography tools can yield 3D layered structures. The multilayer lithography would be very difficult to achieve high resolution layered thickness control and layer to layer alignment for finer resolution 3D microstructures.

In this chapter, we will present our innovative prism-assisted inclined UV lithography for the fabrication of 3D microstructures in SU-8 photoresist. A prism is used as a refractor to deflect the incident UV light and expand the exposure beam angle range in the resist film. The sample internal surface reflection of the exposing UV light can facilitate the fabrication of symmetric structures. Prism with multidirectional side surfaces can be used to achieve one-step exposure fabrication of multidirectional slanted structures. The technique can support the fabrication of the needed angled surface in polymer waveguides for card-to-backplane optical interconnects.

3.1 Microstructure Fabrication

Many practical applications of 3D microstructures have been reported, such as V-grooves for fiber holder [92], mesh structures for microfilter [93], inclined surfaces for the optical pick-up head [84], pyramid array for optical display [94, 95], and some complex microstructures for micromixer [96, 97] and drug delivery [83, 98]. Inclined UV lithography has recently been used for the fabrication of 3D microstructures [95, 99-102]. It has demonstrated effective production of various 3D patterns for many practical applications. Two critical problems, namely limited exposure angle and complicated rotation process, have so far restricted the widespread use of the inclined UV lithography in the fabrication of 3D microstructures.

Many devices, such as optical pick-up heads [84], embedded waveguide mirror [58], and sharped microneedles [83], require microstructures with large side surface angles measured from the normal direction of the resin surface. The widely used negative photoresist SU-8 (refractive index n = 1.67 at 365 nm wavelength) from MicroChem as

an example when exposed directly in air, as shown in Fig. 3.1, the inclined exposure angle in the lithographic resin can in general be easily adjusted by changing the slanted stage angle. However, the refractive beam path bending associated to the large index difference between the air and photoresist has limited the exposure angles in the resin and thus the realization of large angle side surfaces. Governed by the Snell's law, for exposure in air the slanted exposure beam inside the SU-8 is limited to about 36.8°.

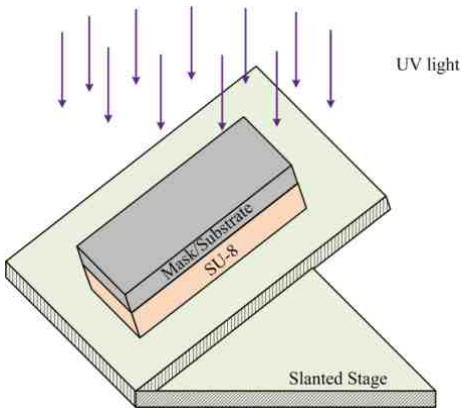

Fig. 3.1. Schematic diagram of inclined UV lithography in the air.

In order to expand the exposure angle in the resin, one way is to immerse the lithographic resin in an index matching liquid [83, 84, 92], such as deionized (DI) water (n = 1.33), heptane (n = 1.39), or glycerol (n = 1.6), which can effectively minimize the light beam path bending, as shown in Fig. 3.2(a). Fig. 3.2(b) presents the simulation results of the exposure angle θ in the SU-8 versus slanted stage angle β in air, water, heptane and glycerol, respectively. The exposure angle can be easily increased beyond 45° with the use of an index matching liquid. However, this immersion method demands a sample settlement time in the index matching liquid to avoid uneven liquid surface and bubble formation. The presence of index matching liquid may affect the UV exposure properties of the resin, because of its influence of certain characteristics of the lithographic resin, such as water content.

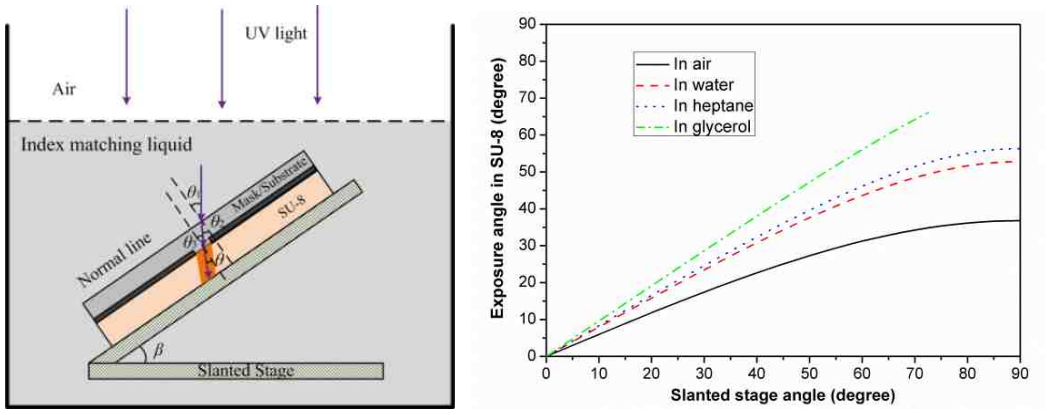

(a) (b)

Fig. 3.2. (a) Schematic diagram of inclined UV lithography in an index matching liquid and (b) simulation of the exposure angle versus slanted stage angle in air, water, heptane, and glycerol.

Multi-directional inclined structures are normally applied in some more complex devices, such as microfilter and micromixer. Multi-step UV exposure with sample rotation has been proved effective. The slanted sample/mask holder of Fig. 3.3 can be used for such purpose. It would be more attractive to introduce a one-step fabrication technique for the realization of 3D microstructures with multi-directional inclined angles.

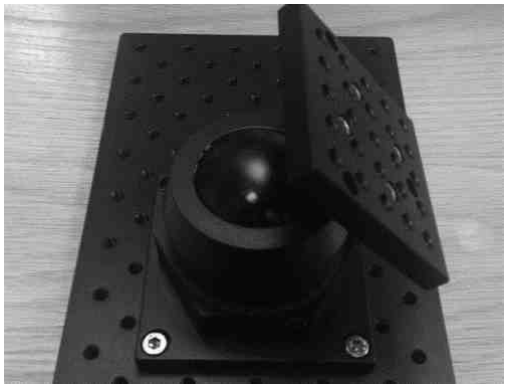

Fig. 3.3. The sample/mask plate holder with rotation features for multi-directional inclined UV exposure.

3.2 Prism-assisted UV Lithography for Slanted Structures with Large Exposure Angles

As schematically presented in Fig. 3.4, the prism-assisted inclined UV lithography can expand the exposure angle of slanted structures in the resin. A glass prism (refractive index 1.53 at 365 nm) acts as a refractor to deflect the direction of the incident UV light in the resin for the inclined UV lithographic exposure. This overcomes the exposure angle limitation due to the original large index difference between air and photoresist. The back-side UV exposure is applied here for accurate patterning benefiting from the intimate contact between the photomask/substrate and the resin. The prism side surface to bottom surface angle is α. PDMS serves as a good candidate for fast custom prototyping of the prism in house [103] with needed prism angle, benefiting from its low cost, molding flexibility, and easy angle control. The slanted stage provides an inclined angle β to the horizontal plane. The incident UV light at 365 nm i-line wavelength is perpendicular to the horizontal plane.

In the lithographic exposure process, the refractions of UV light happen at air/prism, prism/mask, and mask/SU-8 interfaces, as schematically illustrated in Fig. 3.4(b). The relationships between the incident and refractive angles on all interfaces can be obtained based on the Snell's law. The exposure angle θ in SU-8, as a function of the prism angle α and slanted stage angle β, can be written as

$$\theta = \sin^{-1}\left\{\frac{n_{prism}}{n_{su-8}}\sin\left[\alpha - \sin^{-1}\left(\frac{n_{air}}{n_{prism}}\sin(\alpha-\beta)\right)\right]\right\}, \tag{3.1}$$

where n denotes the refractive index of each medium.

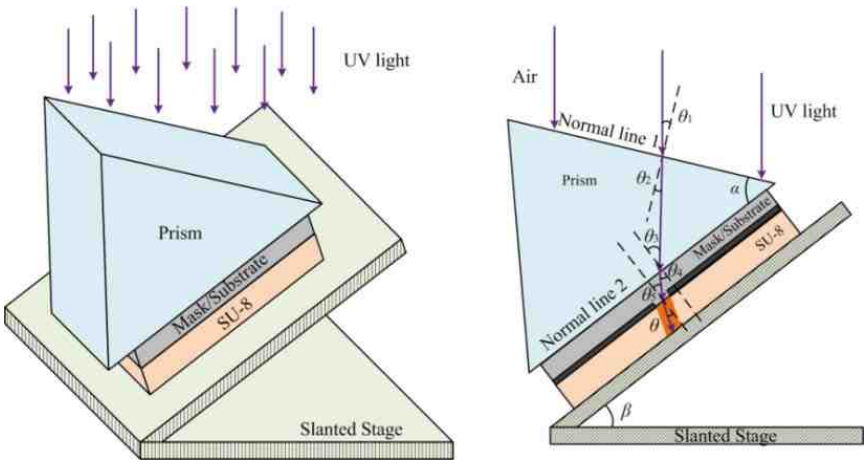

(a) (b)

Fig. 3.4. (a) Schematic diagram of prism-assisted UV lithography for the expansion of the exposure angle in the resin. (b) Schematic of cross-sectional view of the UV light path bending.

The calculated relationships of exposure angle θ, the prism angle α, and the slanted stage angle β are shown in Fig. 3.5. The exposure angle in SU-8 can be easily expanded beyond 60° by using this method. Different combinations of α and β to realize 15° (green dash-dot line), 30° (black solid line), 45° (red dotted line), and 60° (blue dashed line) inclined surfaces are also highlighted in this figure. Obviously, we can expand and control the exposure angle in SU-8 by flexibly varying the combination of the prism angle and the slanted stage angle.

Using this technique, we have fabricated 3D slanted structures with different inclined angles of 15°, 30°, 45°, and 60° as illustrated in Fig. 3.6. A 45° prism was used in the fabrication process, and the slanted stage angles were set to 0°, 27°, 54°, and 85°, respectively. Some functional and interesting inclined structures with 45° exposure angles (see Fig. 3.7) can be easily fabricated using this method.

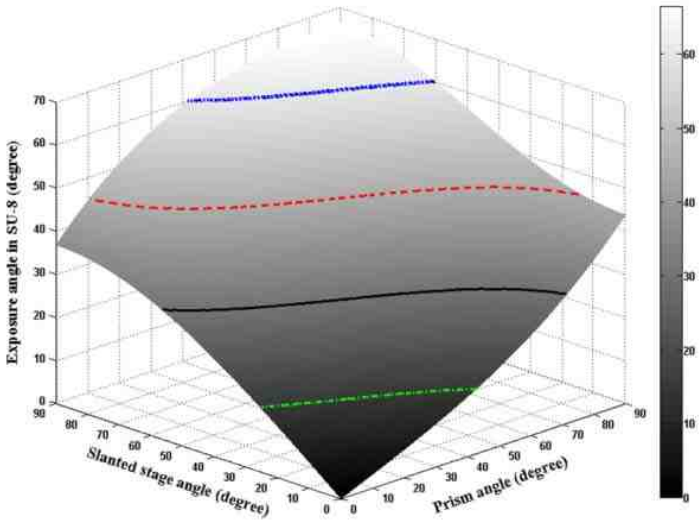

Fig. 3.5. The exposure angle θ in SU-8 as a function of the prism angle α and slanted stage angle β.

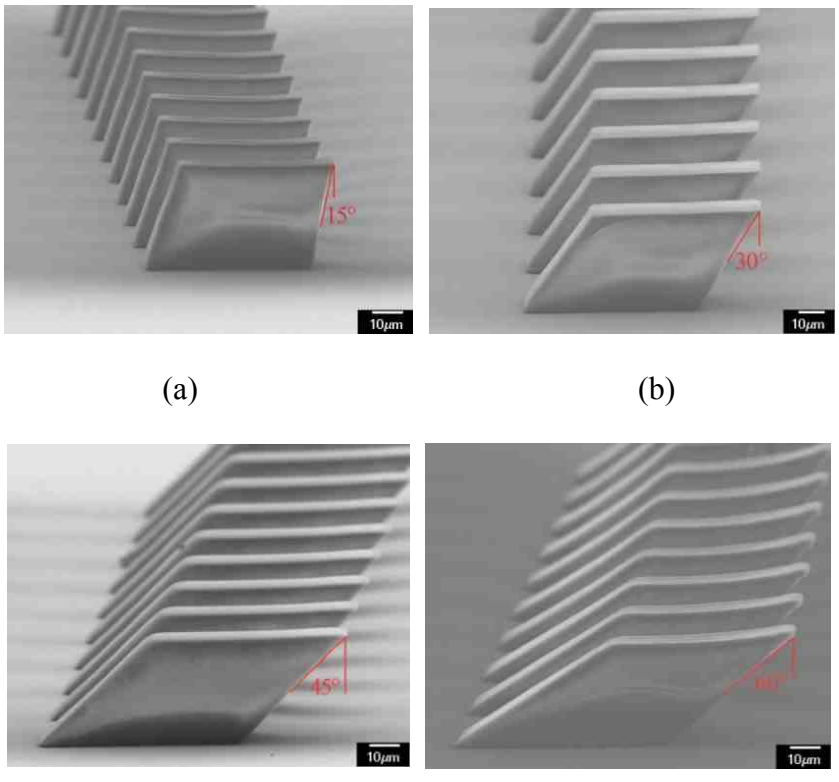

(a) (b)

(c) (d)

Fig. 3.6. SEM images of the fabricated inclined structures with different exposure angles.

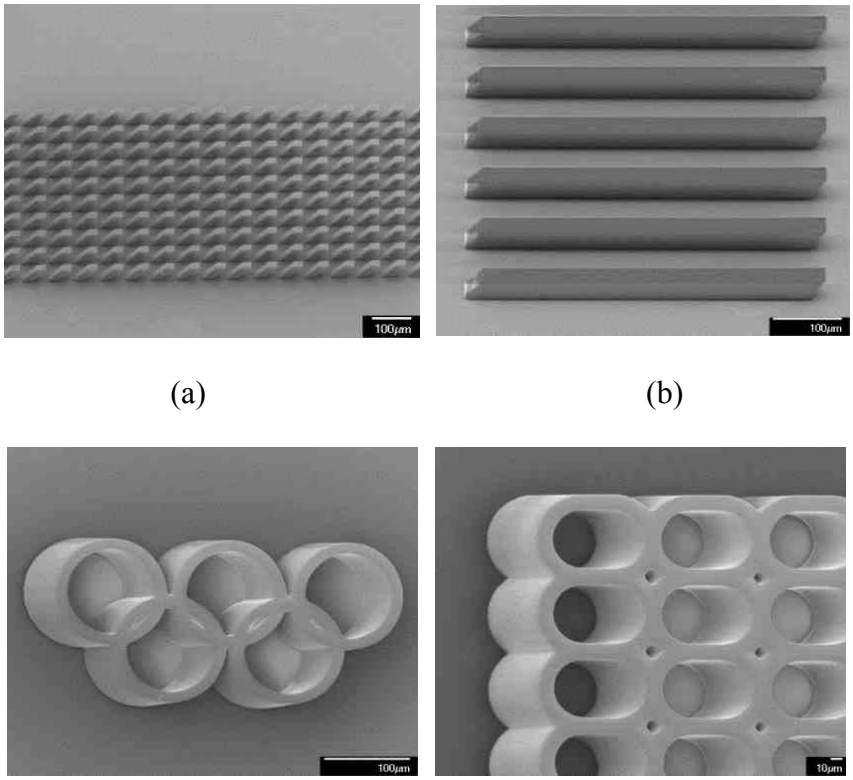

(a) (b)

(c) (d)

Fig. 3.7. SEM images of the fabricated 3D inclined microstructures with 45° exposure angles.

The concept of utilizing the sample internal surface reflected exposing UV light to initiate cross-linking of the photoresist by increasing exposure times at a fixed UV light power [101, 104] is given in Fig. 3.8. This is a simple yet efficient way to fabricate symmetric microstructures instead of twice exposures. The SEM images of the fabricated symmetric microstructures with 45° slanted surfaces on both sides are shown in Fig. 3.9.

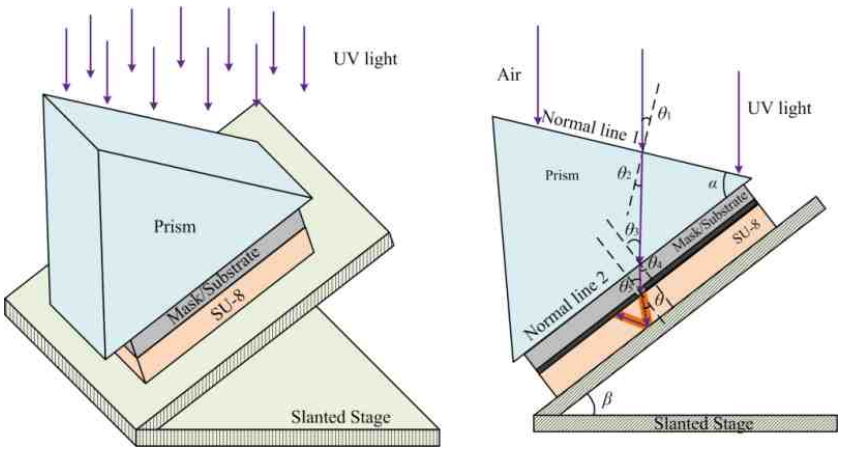

(a) (b)

Fig. 3.8. (a) Schematic of initiating cross-linking of the resin. (b) Schematic of cross-section view of the UV light path bending showing both incident and reflection exposures.

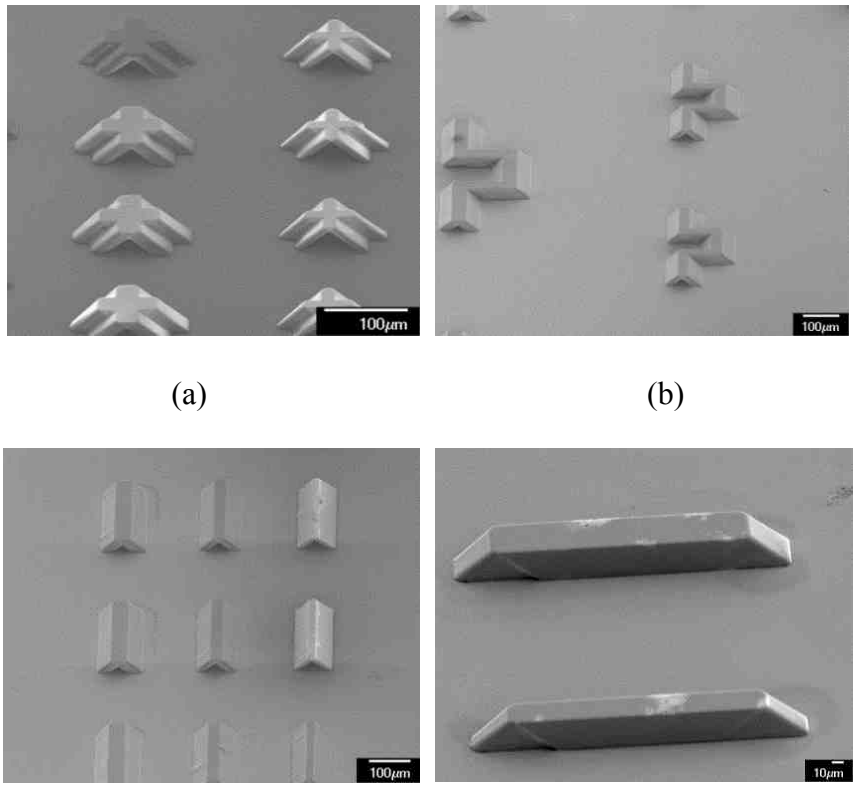

(a) (b)

(c) (d)

Fig. 3.9. SEM images of the inclined structures with 45° exposure angles fabricated by internal reflected UV exposure beams.

3.3 Prism-assisted One-step UV Lithography for Multidirectional Inclined Structures

Besides the expansion of the exposure angle, the prism-assisted UV lithography is also attractive in one-step exposure fabrication of 3D structures with multi-directional inclined angles. The fabrication of V-cut structures with a right angle prism has been reported [105]. A multi-surface optical prism of a polyhedron pyramid structure (a polyhedron pyramid prism) is introduced here to assist the fabrication of some particular microstructures as depicted in Fig. 3.10(a). Different side surfaces of the prism will simultaneously deflect UV light to different directions. Therefore, a set of slanted exposure beam columns will be formed by a set of refracted exposure beams from these side surfaces. It is thus possible to fabricate a complex multi-directional slanted structure in one step. Here, the slant stage angle β is set to be 0°. To illustrate this concept, we show the bending UV light paths from two side surfaces of the prism in Fig. 3.10(b).

A corner prism in Fig. 3.11 (a) was used in our experiment. It has a refractive index of 1.53 at 365 nm and a prism angle of 54.7° for all three side surfaces. The exposure angle θ in SU-8 caused by the refracted UV beams from each side-surface is 21°. When using a separated circular hole mask pattern, three slanted exposure beam columns are formed simultaneously by the refracted exposure beams from these three side surfaces. Thus, the exposure structure is an upside-down tripod structure. Fig. 3.11(b) and (c) present the fabricated upside-down tripod structures with different heights. Fig. 3.11(d) is the side view of the tripod structure when placing on its side which is dimensionally similar to that of Fig. 3.11(c).

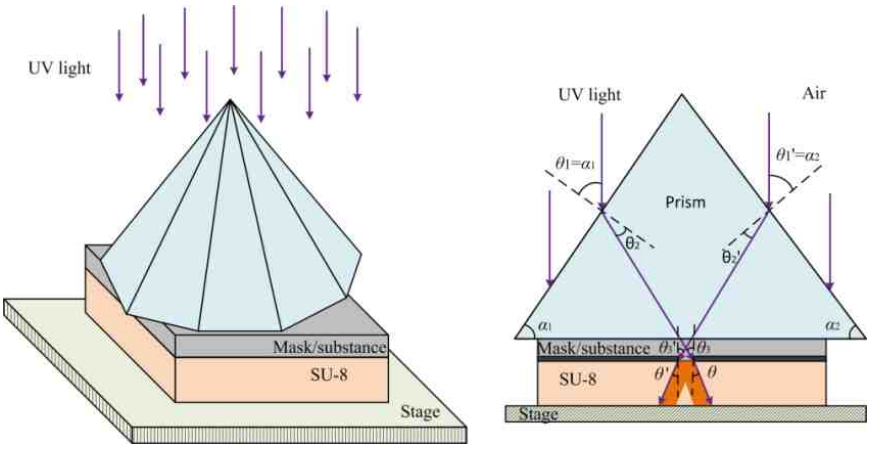

(a) (b)

Fig. 3.10. (a) Schematic diagram of fabricating multi-directional structures using a polyhedron prism. (b) Schematic of a cross-sectional diagram showing the UV light paths.

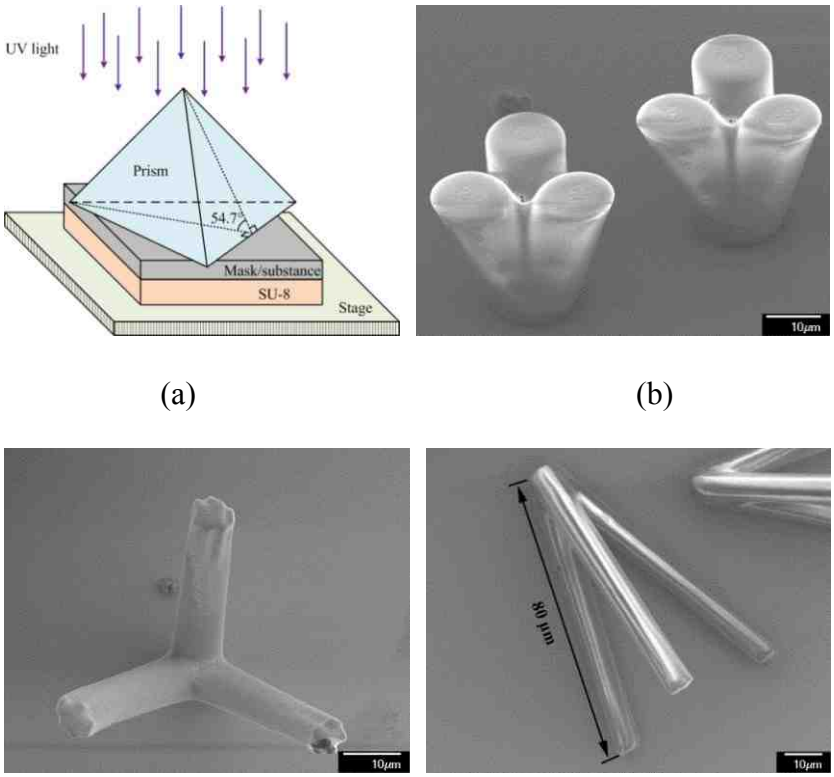

(a) (b)

(c) (d)

Fig. 3.11. Fabrication of upside-down tripod structure by one-step exposure using a corner prism.

By arranging the basic upside-down tripod structures side by side, more complex 3D microstructures can be obtained. We use a mask pattern of an equilateral triangular lattice of circular holes in the experiment. If one base side of the prism is parallel to one side of the triangular lattice (see Fig. 3.12(a)), the nearest three upside-down tripod structures will intersect as shown in Fig. 3.12(b). If the prism is rotated in-plane by 90°, one base side of the prism will be vertical to one side of the triangular lattice (see Fig. 3.12(c)). The nearest three upside-down tripod structures will not intersect with each other and a new structure as illustrated in Fig. 3.12(d) is obtained.

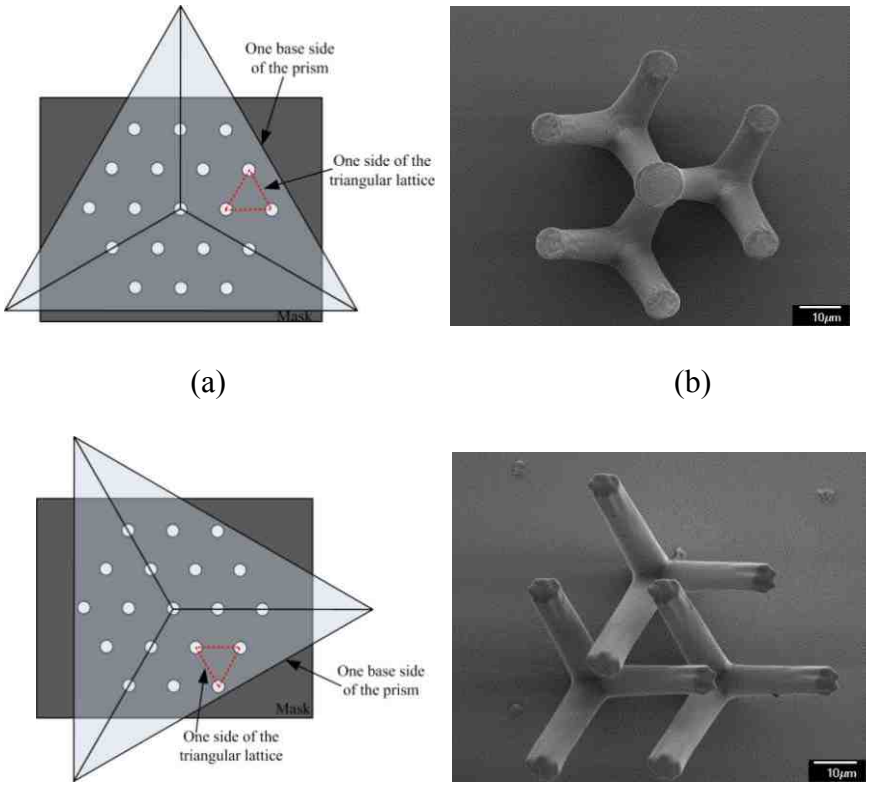

Fig. 3.12. Two specific ways for the arrangement of the basic upside-down tripod structures.

With the setup in Fig. 3.12(a), the structure in Fig. 3.13(a) which owns a new layer with an equilateral triangular lattice of circular holes is formed when the height of the structure is 55 μm and the side length of the triangular lattice on the mask is 36 μm. If we change the setup as shown in Fig. 3.12(c), the 3D mesh structure highlighted in Fig. 3.13(b) is realized when the side length of triangular lattice on the mask is 28 μm and the height of the structure is 72 μm. This structure consists of three independent parts similar to that of Fig. 3.13(a). The three independent parts can be easily distinguished by following the color arrows indicated in Fig. 3.13(b), red arrows (the first part), blue arrows (the second part), and black arrows (the third part). Since this 3D mesh structure has three independent parts that are weaved closely together without intersecting, it may have a great strength and a greater flexibility. Therefore, this technique may be used to fabricate carbon fiber sheets with certain extensibility.

Fig. 3.13(c) and (d) presents a structure having one more layer than that of Fig. 3.12(a) which is achieved by adjusting the height of the structure to be 85 μm and the side length of the triangular lattice to be 28 μm. The periodicity of this 3D microstructure in the vertical direction can be realized by increasing the height of the structures or decreasing the side length of the triangular lattice on the mask. This method may be applied to the fabrication of 3D photonic crystals at optical wavelengths if its size and periodicity can be further reduced.

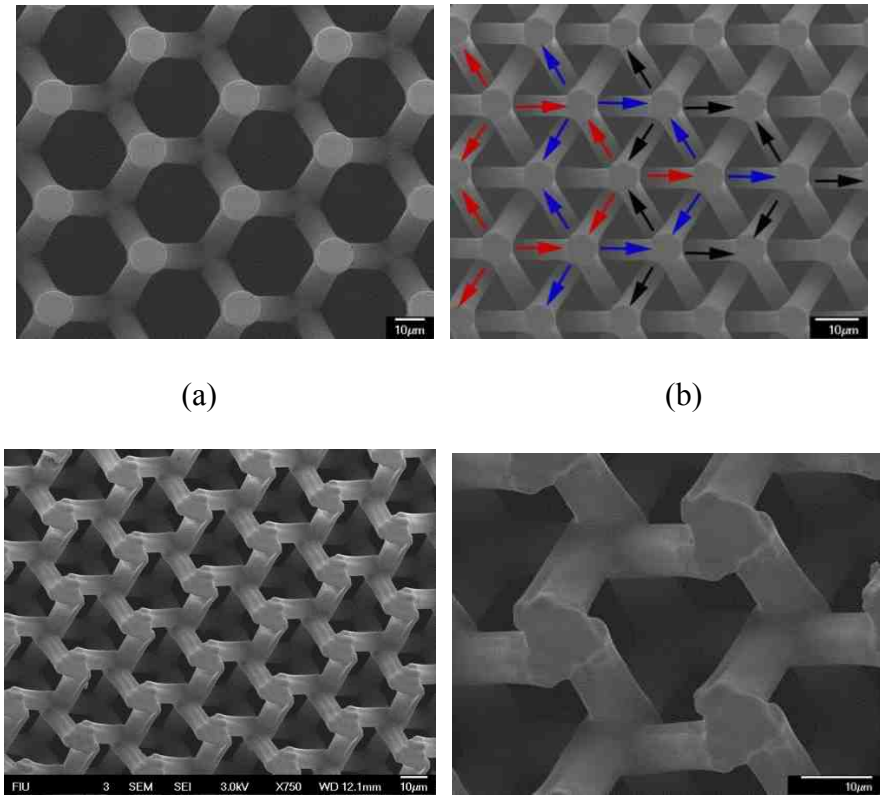

(a) (b)

(c) (d)

Fig. 3.13. SEM images of the fabricated complex 3D microstructures using a corner prism.

If we replace the corner prism in Fig. 3.11(a) with a cone prism as illustrated in Fig. 3.14(a), circular symmetric 3D structures can be obtained. In the experiment, the cone prism (refractive index 1.53 at 365 nm) has a 60° prism angle. Since all refracted UV light beams from cone surface intersect at the center of the base plane, by position a circle hole mask pattern at the base center of the prism, the exposure pattern on the photoresist will show a horn structure. The fabricated horn structure is presented in Fig. 3.14(b) when using a mask with a 20 μm diameter circular hole pattern. The defects on the fabricated horn structure may be attributed to the misalignment between the center of circle pattern and the base center of prism and/or the imperfections of the cone prism.

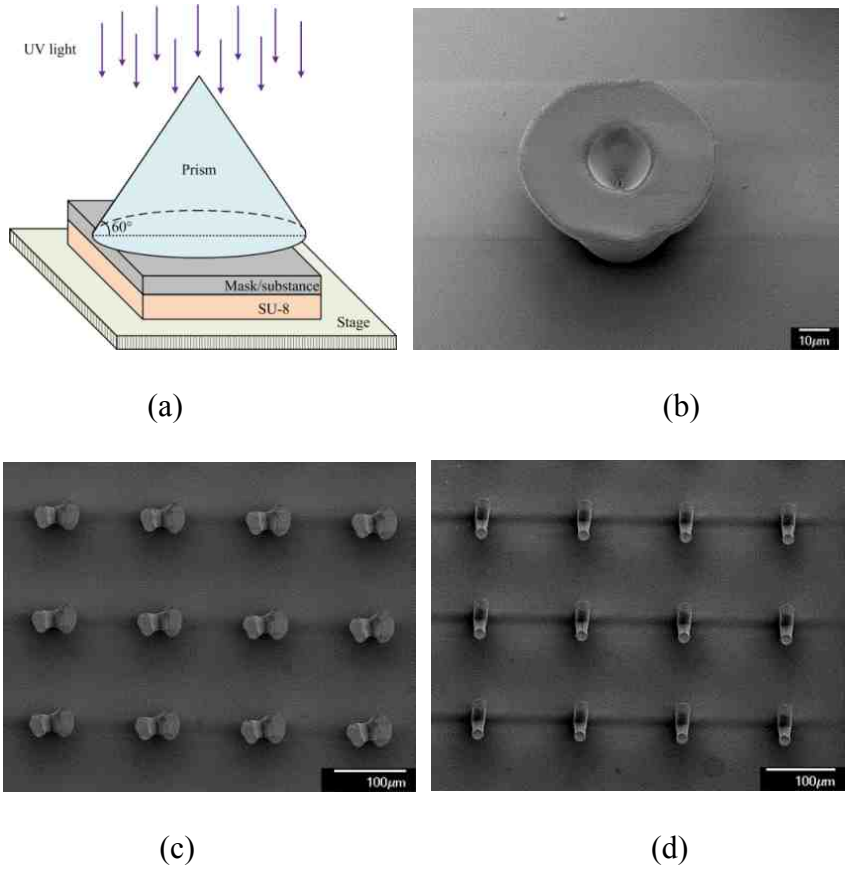

Fig. 3.14. Fabrication of horn and fan-shaped structures by one-step exposure using a cone prism.

If the circle hole mask pattern is not located at the center of the cone prism, the refracted UV light beams from cone surface to different directions will be asymmetric when passing through the circle hole mask pattern, so yielding asymmetric fan-shaped 3D structures. Fig. 3.14 (c) and (d) presents the asymmetric exposure patterns on the photoresist, when the circle holes mask pattern is 3 mm and 10 mm away from the base center of the prism, respectively. Because these holes are close to each other as a group but much farther away from the base center of the prism, these holes received similar asymmetric exposure and thus resulted in similar lithographic patterns. Clearly, different

displacement from the base center of the prism will result in different asymmetric exposures.

When using a polyhedron pyramid prism for one-step UV lithographic fabrication of 3D multi-directional slanted structures, attention should be paid on the exposure dosage. There is certain beam energy lost as the UV light passes through the prism and interfaces. The exposure energy should be well controlled in the experiment. Fig. 3.15 shows the fabrication result of a similar structure as shown in Fig. 3.13(b) without enough exposure dosage. The structure consists of three independent parts, as we mentioned earlier. However, after photoresist developing, the inclined pillars cannot support the intersection resulting in the structural collapse. Over exposure may avoid the structural collapse but will introduce surface reflection exposure and structure size expansion that is also not desirable.

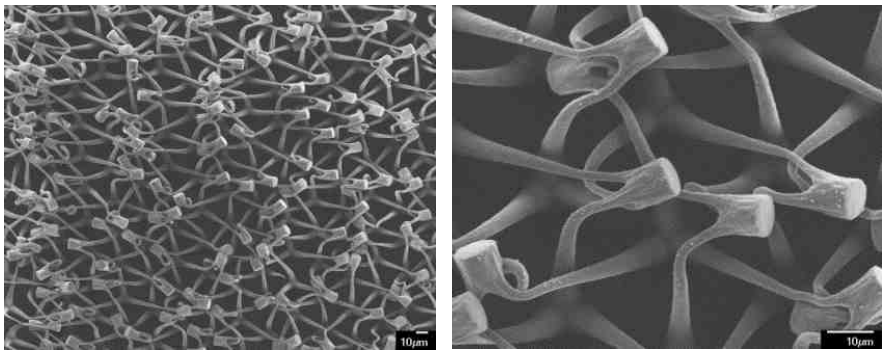

(a) (b)

Fig. 3.15. SEM images of the fabricated similar structure of Fig. 3.13(b) without enough exposure dosage with (b) as magnified view of a local portion of (a).

For multi-directional exposure, attention should also be paid on the effective exposure area of the prism, which also has a great influence on the formation of multi-directional slanted structures. Each side surface has its own projected exposure area (the projection

of the side surface to the prism base), so the total effective exposure area means the common area of these projected exposure areas. Take a rotationally symmetric polyhedron pyramid prism as an example, the effective exposure area is determined by the slanted angle α of the prism, the number of side surfaces n, and the circumradius r of the polygonal base. Fig. 3.16(a) shows the calculated results of effective exposure area (blue circles) and its percentage on the base area (red triangles) as a function of the number of side surfaces, at $\alpha = 60°$ and $r = 25$ mm. The effective exposure area and its percentage decrease rapidly as the increase of the number of the side surfaces. Fig. 3.16(b) (blue solid line with $\alpha = 60°$ and $n = 3$) shows that the effective exposure area can be enlarged by increasing the circumradius of the polygonal base when the number of the side surfaces is fixed. We also found that the percentage of the effective exposure area is independent of the circumradius of the base, as indicated in Fig. 3.16(b) (red dashed line). Therefore the number of side surfaces and the circumradius of the base need to be reasonably selected in structural fabrication design.

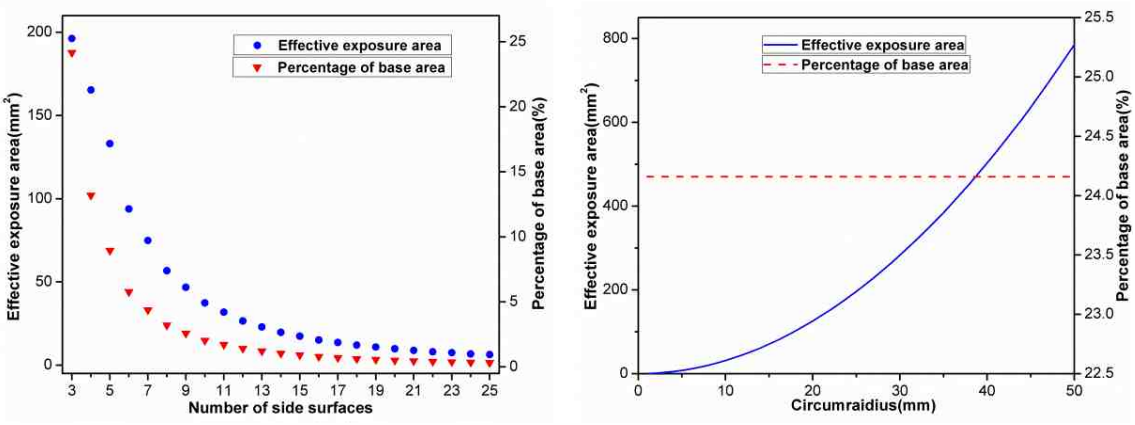

(a) (b)

Fig. 3.16. The effective exposure area and its percentage of base area (a) depend on the number of side surface and (b) depend on the circumradius of the base.

3.4 Summary

The prism-assisted inclined UV lithography is a flexible lithographic technique for the fabrication of 3D microstructures with large and small side surface angles. The one-step multi-directional exposure fabrication is attractive for fabricating complex 3D microstructures.

This method can be widely used for the fabrication of optical pick-up heads, embedded waveguide mirror, and sharped microneedles. In this ensuing chapter we demonstrate our exploitation of polymer waveguides with integrated 45° mirrors fabricated by the prism-assisted inclined UV lithography.

Chapter 4

Flexible Polymer Waveguides with Integrated Mirrors for Optical Interconnects

As discussed earlier, card-to-backplane optical interconnects can benefit from the use of flexible polymer waveguides on the backplane. The polymer waveguides can be attached to the backplane after the electronic circuit fabrication/packaging, thus minimizing changes to existing circuit board fabrication industry. As discussed in Chapter 2, the polymer waveguides can be fabricated by UV photolithography and in particular by vacuum assisted microfluidic soft lithography. We have synthesized the UV curable polymer resins with controllable refractive index. In Chapter 3, we have demonstrated slanted surface fabrication by prism-assisted inclined UV lithography. This technique can be used to fabricate waveguide mirrors for surface normal optical coupling which is needed in card-to-backplane optical interconnection.

In this chapter, we are now ready to present the fabrication of polymer waveguides with 45° integrated mirrors using the VAM soft lithographic technique to support card-to-backplane optical interconnects. The SU-8 master with 45° inclined surface structures was fabricated by the prism-assisted UV light exposure. A PDMS mold with a negative imprint was subsequently created. The desired waveguides having 45° integrated mirrors were realized via VAM soft lithography using our synthesized UV curable resins. The fabricated polymer waveguides with 45° integrated mirrors demonstrated a propagation loss of -0.24 dB/cm, and a coupling efficiency of 75% and 38% for full and half mirrors, respectively.

4.1 VAM Soft Lithography Fabrication of Polymer Waveguides with Integrated Mirrors

VAM is a new microfluidic based replication technique which can be widely used for polymer optical waveguide fabrication. It can be utilized to improve the performance of imprinted devices by eliminating the residue planar layer and accomplish complex devices incorporating different materials in the same waveguide layer. Different from Chapter 2 which shows how the channel waveguide is formed by VAM, in this chapter we show the practical realization of polymer waveguides with 45° waveguide mirrors and their use in card-to-backplane optical interconnection along with coupling efficiency.

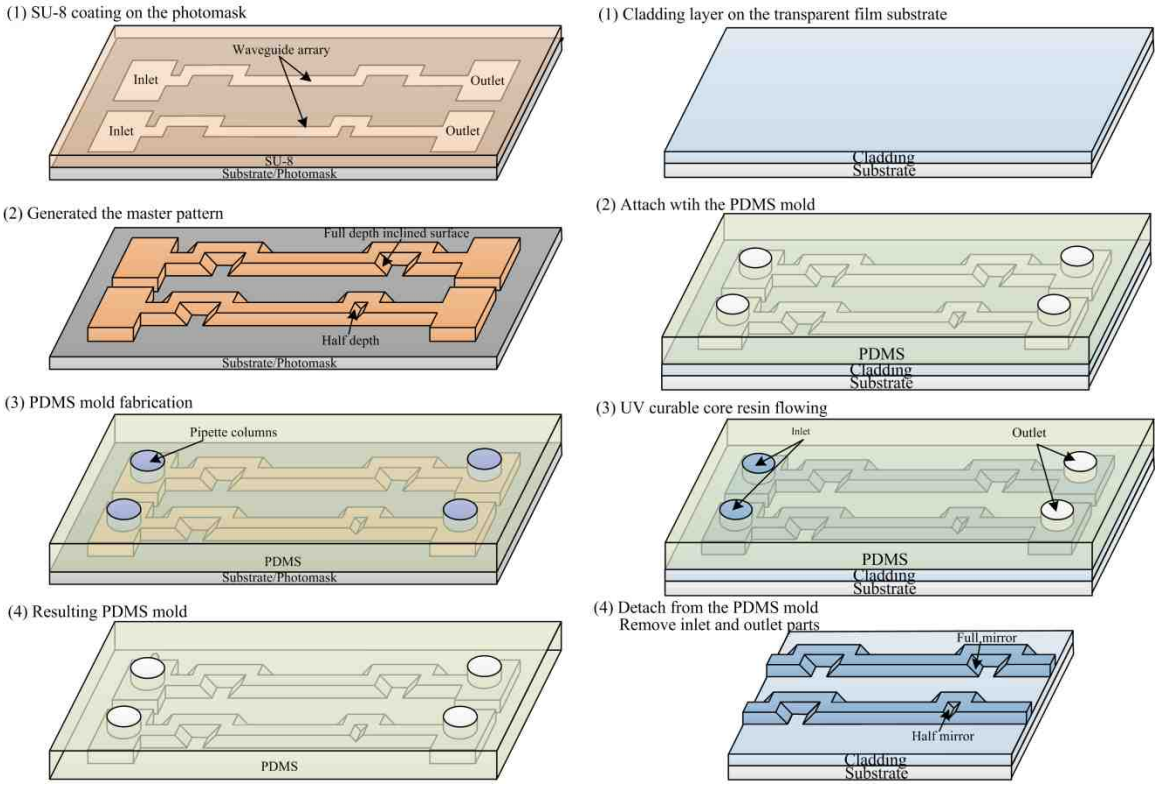

(a) (b)

Fig. 4.1. Schematic illustration of the whole process of (a) PDMS mold fabrication and (b) polymer waveguide imprint.

The VAM soft lithography fabrication of polymer waveguides with 45° integrated mirrors requires a PDMS mold with microfluidic hollow channel structures to guide the polymer resin flow. The master pattern with the structure of channel waveguides also has the needed 45° slanted mirrors. The fabrication of the master pattern uses the prism-assisted UV lithography as shown in Fig. 3.8 and Fig. 4.2. A PDMS mold with microfluidic hollow channels which is a negative imprint from master pattern can be subsequently created. The desired waveguides with 45° integrated mirrors are then realized via VAM soft lithography using synthesized UV curable resins. The whole processes about PDMS mold fabrication and polymer waveguide imprint are schematically illustrated in Fig. 4.1(a) and (b), respectively.

4.1.1 SU-8 Master and PDMS Mold Fabrication

For the master pattern fabrication, a negative photoresist SU-8 (from MicroChem) was spin coated on a substrate. Because of the large index difference between air and SU-8, the exposure angle inside the SU-8 (refractive index 1.67 at 365 nm) is limited to below 36.5° with inclined UV lithographic exposure. To achieve 45° exposure angle in the SU-8, we used a prism (refractive index 1.53 at 365 nm) as a refractor to deflect the incident exposure UV light as shown in Fig. 4.2(a). We can realize accurate patterns through back-side UV exposure due to intimate contact between the photomask/substrate and the SU-8. The prism and the mask/substrate were well attached by using the index matching material (De-ionized water) at their interface. The UV light reflected by the sample internal surface was utilized to eliminate undercut structures and to realize 45° inclined surfaces on both ends of the straight channel segments via one-step UV exposure, as shown in Fig. 4.2(b).

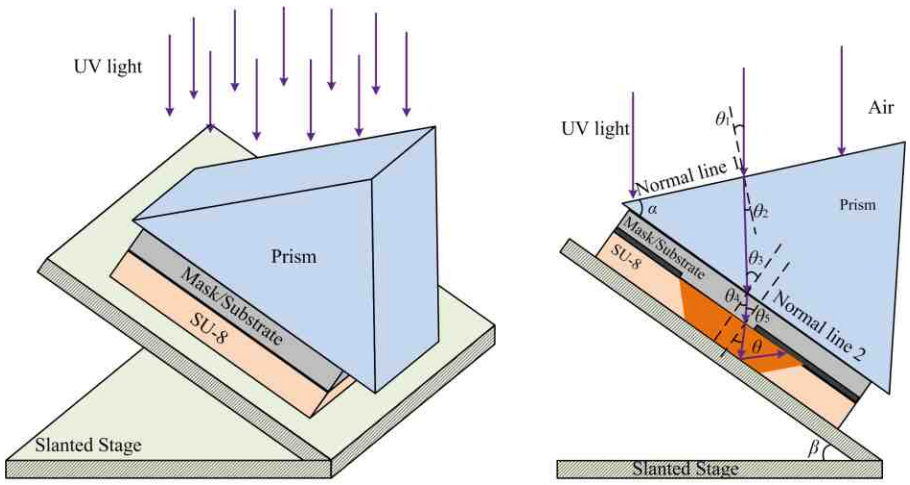

(a) (b)

Fig. 4.2. (a) Schematic diagram of prism-assisted inclined UV lithography. (b) Schematic of cross-section view of the UV light path bending.

The associated UV light refracts at the air/prism, prism/mask and mask/SU-8 interfaces resulting in a final UV exposure beam angle within the SU-8 photoresist. The exposure angle θ in the photoresist is related to the prism angle α, the slanted stage angle β, and refractive index of each medium n by Eq. (3.1). When the slanted stage angle is 54° and the prism angle is 45°, the exposure angle in the SU-8 will be the required 45°.

An UV transparent glass, which also bears a prepatterned photomask layer, was used as the substrate, as shown in Fig. 4.3. The pattern on the photomask consists of an inlet part, an outlet part, and straight waveguide channels. The small bends were used at both ends of waveguide for continuous microfluidic flow, which have negligible influence on the light propagation as confirmed by BeamPROP (Rsoft) simulation. The distance D between the two adjacent parts in each waveguide can be adjusted during photomask design to control the depth of the resulting inclined surface. The schematic view of the fabricated full depth and half depth inclined surfaces are shown in Fig. 4.1(a). This can help achieve the inclined mirrors of different sizes that eventually determine the

percentage of light in the waveguide to be reflected to the surface normal. The percentage of light reflection by the inclined surface mirror is also governed by the mirror quality as well as the overlap between the propagating waveguide modes and the mirror structure.

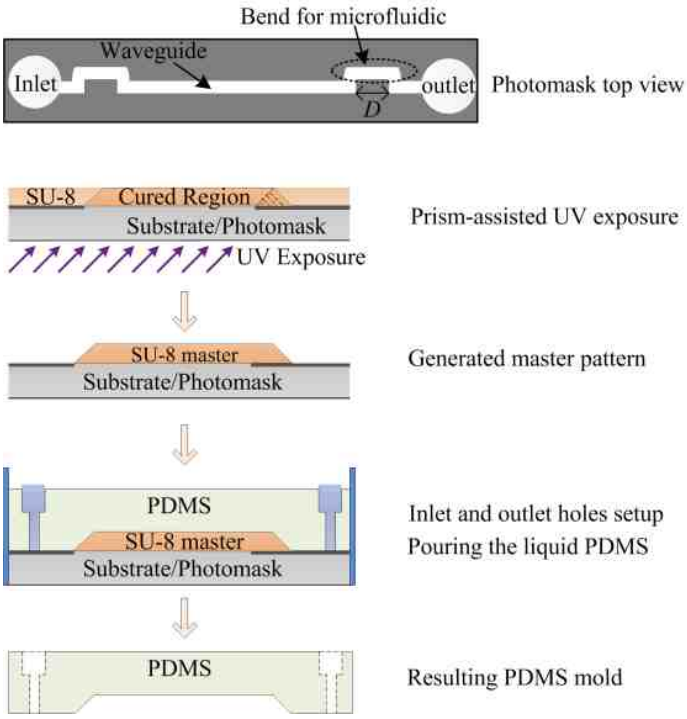

Fig. 4.3. Schematic of the fabrication process of the SU-8 master and the PDMS mold.

The SU-8 master and PDMS mold fabrication process is illustrated in Fig. 4.3. First, the SU-8 2035 photoresist was spin coated on the substrate/photomask with a thickness of 40 µm followed by pre-baking. The size of the waveguide structures on the photomask was designed to be 50 µm waveguide width and 35 mm mirror-to-mirror waveguide length. The reverse-side inclined UV exposure at the required incident angle was then performed to achieve the needed 45° exposure in the SU-8 photoresist. Increasing exposure time yielded 45° inclined surfaces on both ends of the mask channel pattern through internal UV surface reflection as illustrated in Fig. 4.2(b). Followed by subsequent post baking and photoresist developing, the SU-8 master with waveguide

channel patterns and 45° inclined surfaces was obtained. The fabricated master was transferred to the PDMS mold. It was prepared by pouring the liquid PDMS on the master encased by aluminum freezer tape and with inserted plastic pipette columns as inlet and outlet holes. After settling for 3 hours at 85°C, the PDMS mold was then peeled off and ready for use.

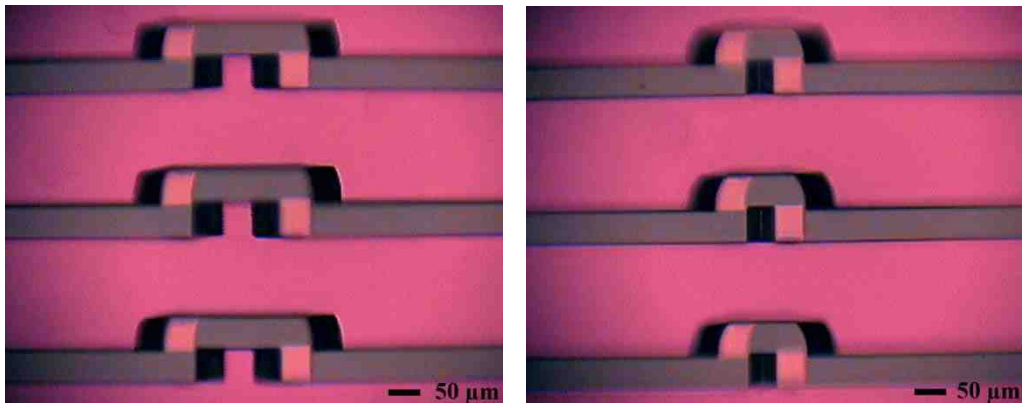

(a) (b)

Fig. 4.4. Top view of the fabricated SU-8 master with full depth inclined surfaces (a) and half depth inclined surfaces (b).

Fig. 4.4 shows the microscope images of the SU-8 master on the mask/substrate. The full and half depth inclined surfaces were both fabricated. The shown black rectangles at the end of waveguide segments are due to the imaging light not reflected back by the inclined surfaces to the observation microscope. The observed lighter rectangles (and background) are caused by the presence of chrome layer on the bottom. This results in more imaging light being reflected by chrome layer to the observation microscope. The fabricated slanted surfaces angles were measured from SU-8 master pattern [106], ranging from 44.5° to 45.5°, with a ±1% deviation from the designed angle.

4.1.2 Polymer Waveguides with Integrated Mirrors Imprint

UV curable polymer resin is critical for the VAM waveguide fabrication. The core waveguide resin must have a higher refractive index than the cladding while the core resin must have low enough viscosity to facilitate the channel flow guided by the PDMS mold. The suitable core and cladding resins were synthesized and the refractive indices at 850 nm were found to be 1.515 and 1.500 respectively, as measured by an ellipsometer (Angstrom Sun Technologies). So the corresponding numerical aperture of the fabricated waveguide will be 0.21.

The polymer waveguides imprint process by VAM soft lithography is shown in Fig. 4.5. First, a cladding resin layer of about 20 μm thickness was spin coated on the OC Grade Polymer Film (Grafix Plastics) followed by UV curing at 100 mW/cm^2 power level for 2 min. The PDMS mold was then placed in conformal contact with the cladding layer. The UV curable core waveguide resin was injected into the inlet hole, and suction was provided to the outlet hole using a vacuum pump to assist the microfluidic flow of the resin in the PDMS channels. The flow speed was controlled through vacuum adjustment to be about 2 mm/min in our experiment for a better performance of the fabricated polymer waveguide. Following UV curing at the same 100 mW/cm^2 power level for 4 min, the PDMS mold was removed to reveal the channel waveguides with 45° integrated mirror surfaces. The inlet and outlet tubes were then removed. In our experiment, the PDMS mold which has been used for more than 20 times did not present any noticeable degradation while observed by using a microscope. With careful use we believe the PDMS mold should be good for more than 100 replications that can reduce the cost of device fabrication.

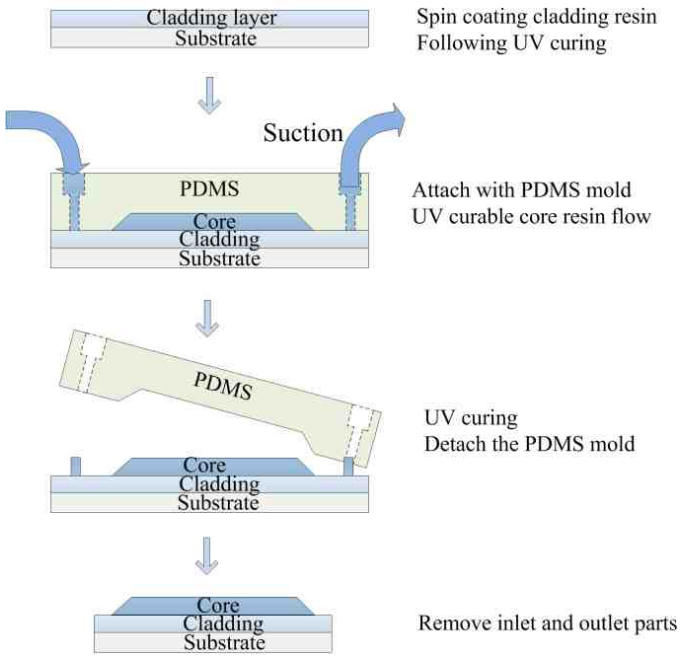

Fig. 4.5. Schematic process of polymer waveguides imprint.

The image of the flexible polymer waveguides with 45° integrated mirrors on the substrate polymer film is shown in Fig. 4.6. The SEM images are given in Fig. 4.7. Fig. 4.7(a) and (b) show the top view and side view of the imprinted polymer waveguides with a full depth (40 μm) inclined mirror surface (full mirror), respectively. Fig. 4.7(c) and (d) present respectively the top and side views of a half depth (20 μm) inclined mirror surface (half mirror).

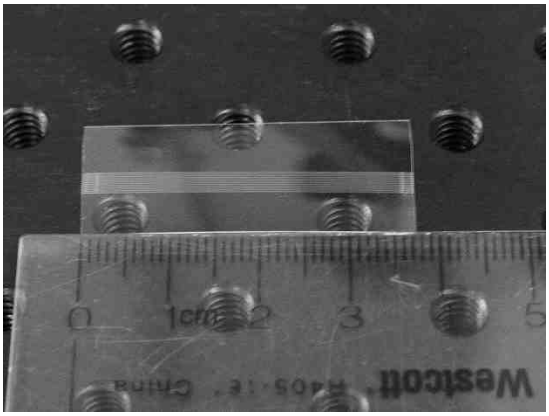

Fig. 4.6. The image of the flexible polymer waveguides with 45° integrated mirrors.

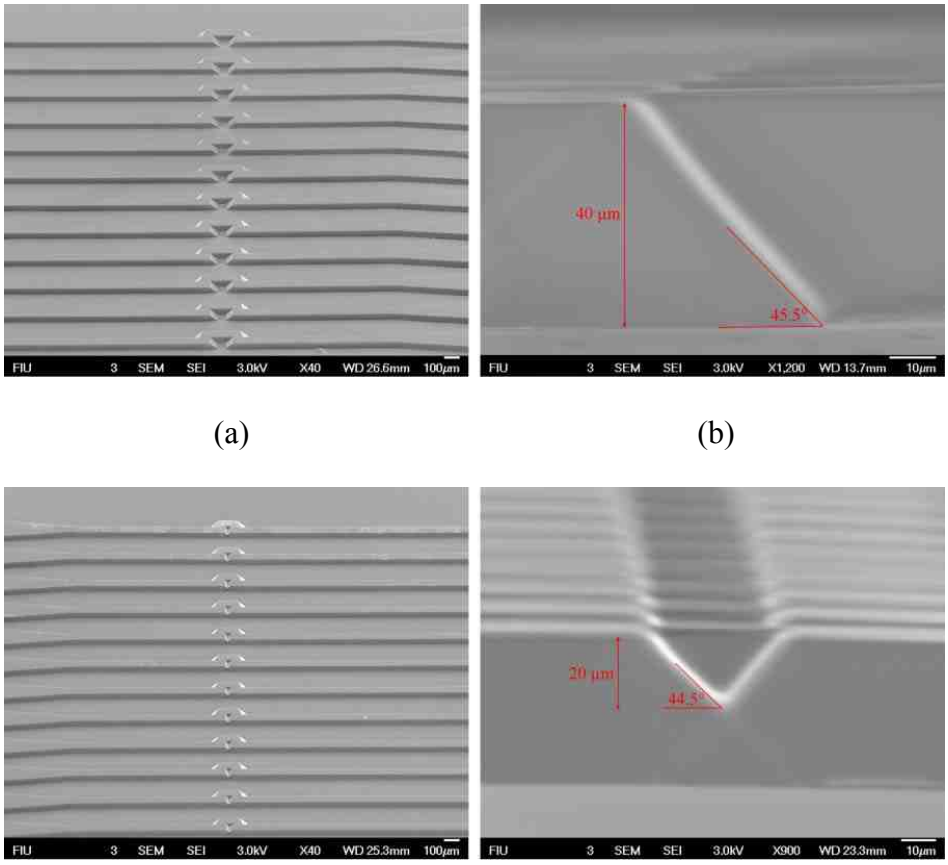

(a) (b)

(c) (d)

Fig. 4.7. SEM images of imprinted polymer waveguides with full mirrors and half mirrors.

4.2 Optical Test

The optical couplings by the integrated full mirrors and half mirrors based on total internal reflection have been demonstrated. In our experiment, 12-channel waveguide array A has full mirrors on both sides of each waveguide, while 12-channel waveguide array B has full mirrors on one side and half mirrors on the other side of the waveguides. A 632.8 nm wavelength laser light was coupled into one waveguide through one full mirror by a standard 9/125 μm single-mode fiber (SMF) with a numerical aperture of

0.13 to observe the surface normal output pattern from the other side. The end of the SMF was fixed above the input 45° mirror region of the waveguide array.

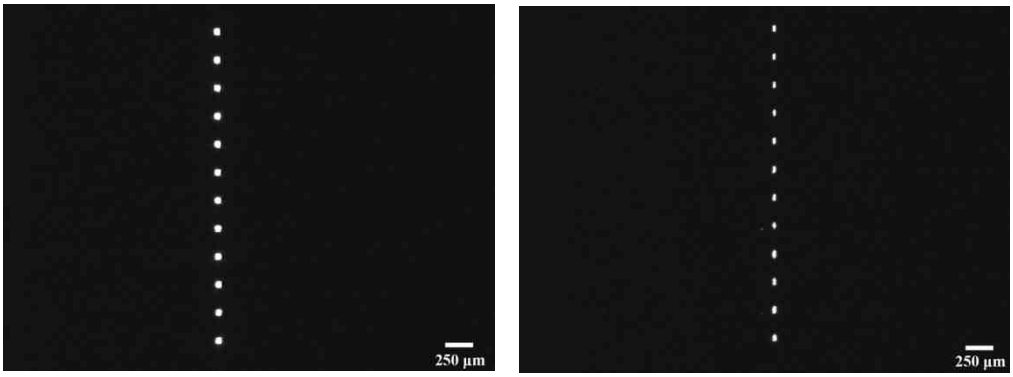

(a) (b)

Fig. 4.8. Light spots detection of the polymer waveguides for (a) full mirrors and (b) half mirrors.

We used a CCD camera to image the output mirrors of the other side of the waveguide array. The input laser beam was shifted one by one from the 1st channel to the 12th channel of the waveguide array to acquire all 12 output beam spots from the output mirrors. Fig. 4.8(a) and (b) show light spots of the polymer waveguides with full and half mirrors, respectively. Clearly, under the same input light illumination power, the size of beam spots of full mirrors is almost twice that of half mirrors measured by a laser beam profiler.

An 850 nm laser light was then coupled into the waveguide in the same way for optical coupling efficiency evaluation since 850 nm light will be used for optical interconnection. The output intensity was measured by a Si photodetector with a fixed distance above each output mirror. The total insertion loss of the mirrors is calculated by the ratio of the output power of each waveguide and the input power at the SMF output end.

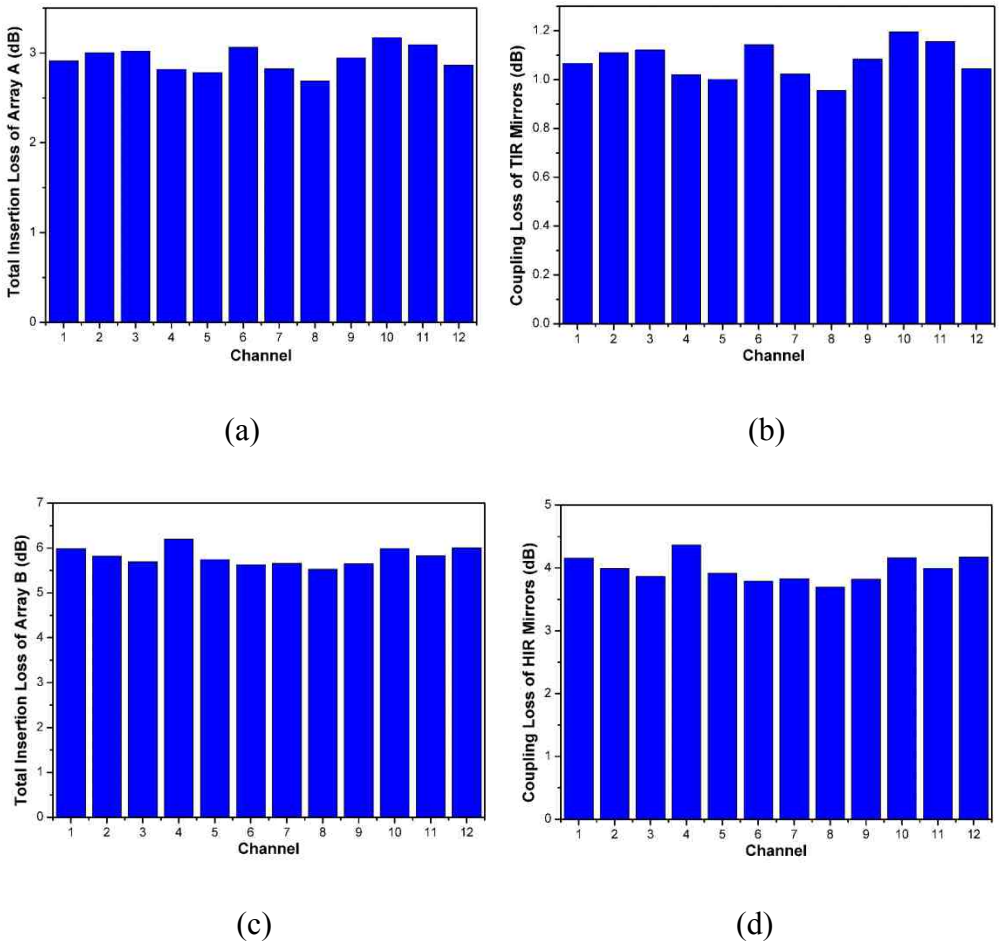

Fig. 4.9. Total insertion loss (a) and coupling loss (b) for full mirrors. Total insertion loss (c) and coupling loss (d) for half mirrors.

Fig. 4.9 (a) and (c) show the total insertion loss of waveguide arrays A and B, respectively. The waveguide propagation loss was measured by conventional cut back method. The straight waveguide array was cut from 3.0 cm to 1.5 cm. The measured average propagation loss for twelve waveguide channels was about -0.24 dB/cm. Assuming the full mirrors on both side of each waveguide have the same coupling efficiency, the average coupling loss of the reflection mirrors was ~ -1.24 dB (Fig. 4.9(b)), which means the corresponding mirror coupling efficiency was ~75%. Assuming the full mirrors of waveguide array B have the same input coupling efficiency as A, the average

coupling loss of half mirrors was ~ -4.15 dB (Fig. 4.9(d)), which means the corresponding mirror coupling efficiency was ~38%. The measurement results are comparable to those fabricated by other techniques [46, 58, 81], yet we have fabricated the waveguides and mirrors in the microfluidic flow process. This demonstrated cost-effective fabrication can be surely used for the formation of waveguide with integrated mirrors for high speed optical interconnect. The integrated mirror without coating can be used in tunable devices [107] with flexible adjustment of coupling efficiency for dynamic optical interconnection. The integrated mirror can also be locally coated with gold followed by an embedded cladding coating [50, 74] for ribbon based optical interconnect applications having stable coupling efficiency.

4.3 Summary

We have presented our recent fabrication of flexible polymer waveguides with integrated mirrors by the VAM soft lithographic technique in this chapter. A prism was used to deflect the incident UV light for the fabrication of a waveguide structure with inclined surfaces in the SU-8 photoresist. The fabricated slanted surfaces angles of the master were measured ranging from 44.5° to 45.5°, with a ±1% deviation from the designed angle. The VAM fabricated polymer waveguides and 45° integrated mirrors demonstrated about -0.24 dB/cm propagation loss, and 75% and 38% mirror coupling efficiency for full mirrors and half mirrors, respectively. This microfluidic flow VAM fabrication is effective, repeatable, and low cost, which may benefit greatly to optical interconnects applications.

Most optical interconnects architectures are based on point-to-point link topology which result in a higher cost per link and a lower energy efficiency. A shared bus topology for card-to-backplane optical interconnects can effectively multicast signals to all plug-in cards, however, most existing reported approaches set a fixed power distribution to each link after device fabrication. They are not energy efficient since they consume optical signal power even when the cards are not plugged into the backplane. In the next chapter, we will present a dynamic card-to-backplane optical interconnect architecture using polymer waveguides with tunable optofluidic couplers. The dynamic activation and deactivation of the backplane optofluidic couplers can save the optical signal power for card-to-backplane optical interconnection.

Chapter 5

Tunable Optofluidic Coupler for Dynamic Card-to-Backplane Optical Interconnects

As discussed in Chapter 4, we have examined the passive polymer waveguides with 45° integrated mirrors for card-to-backplane optical interconnection. Such passive optical interconnection is useful for fixed point-to-point interconnect link and the cost of polymer waveguide ribbon fabrication can be low. Just like passive optical fiber, the polymer waveguide will be efficient for high data rate signal delivery.

The card-to-backplane optical interconnects using shared bus topology can effectively multicast signals to all plug-in cards. However, most existing reported approaches set a fixed power distribution to each link after device fabrication [44, 46, 79]. They are not energy efficient since they consume optical signal power even when the cards are not plugged into the backplane.

A dynamic card-to-backplane optical interconnect requires that the interconnect coupler is ON when needed such as when the card is plugged in and is OFF when not needed. It avoids wasting of the optical signal beam in the backplane waveguide by unwanted surface normal coupling. Such ON/OFF control on the optical interconnect coupler does not need to be high speed and preferably does not consume electrical power. Traditionally, a waveguide based optical coupler can be ON/OFF switched by using thermo-optical coupler and electro-optical coupler. The advantage of these couplers is high speed with short response time (a few microseconds). However, in order to maintain a status, the couplers will consume power. They are wavelength and polarization

sensitive. They also have high sensitivity to waveguide modes. The multi-mode waveguide are usually used for backplane optical interconnection because of low cost fabrication and large alignment tolerance. Therefore, thermo-optical coupler and electro-optical coupler are not suitable for dynamic card-to-backplane optical interconnects.

To facilitate dynamic optical interconnection using shared bus topology, our group has earlier examined the concept of array waveguide evanescent coupler for card-to-backplane optical interconnections (see Fig. 5.1) [6]. This technique evanescently taps optical signal power from a backplane bus to a flexible optical bus on the daughter card and 10 Gbps optical interconnection has been demonstrated. The problems of this approach are that it requires using pressure-adjustable coupler hardware and the coupling length is relatively long (~ centimeter).

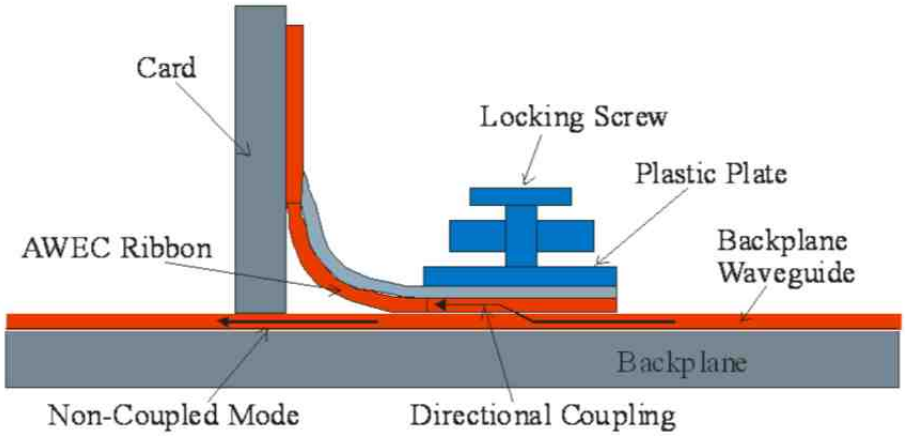

Fig. 5.1. Schematic of array waveguide evanescent coupler for card-to-backplane optical interconnection.

What is truly needed for a dynamic card-to-backplane optical interconnect is pressing ON the interconnect coupler when the card is plugged in and pressing OFF the interconnect coupler when the card is removed. It is like a mechanical switching and upon releasing the press the ON/OFF switching status is maintained. The couplers won't

require any coupler hardware and won't consume power to maintain any status. The coupling length should be quite short (hundreds of micrometers) for high density integration.

Recently, optofluidic technique has got our attention. Optofluidics can bring fluid and light together and exploit their interaction for various applications, such as adaptive optical lenses, optofluidic microscopes, and optofluidic sensors [3, 108, 109]. It also provides exciting opportunities for the realization of tunable optofluidic devices (TOD) using a variety of physical mechanisms [107]. A common method for adjusting the TOD is through modulation of the refractive index which can then cause changes in the phase, amplitude, and/or polarization of the electromagnetic wave propagating through the optical device.

In considering the practical operation advantages of optofluidics, we have designed a new dynamic card-to-backplane optical interconnect architecture using polymer waveguides with tunable optofluidic couplers, as shown in Fig. 5.2(a). It consists of a backplane and multiple plug-in cards. The backplane polymer waveguide will send interconnect light beams to the waveguides on the plug-in cards via 45° integrated waveguide mirrors of the optofluidic coupler. The optofluidic coupler (see Fig. 5.2(b)) consists of the optical waveguides and the perpendicular microfluidic channel with inclined sidewall. They are sandwiched between two low refractive index substrate films while an index matching liquid and air bubbles are located in the microfluidic hollow channel perpendicular to the waveguides.

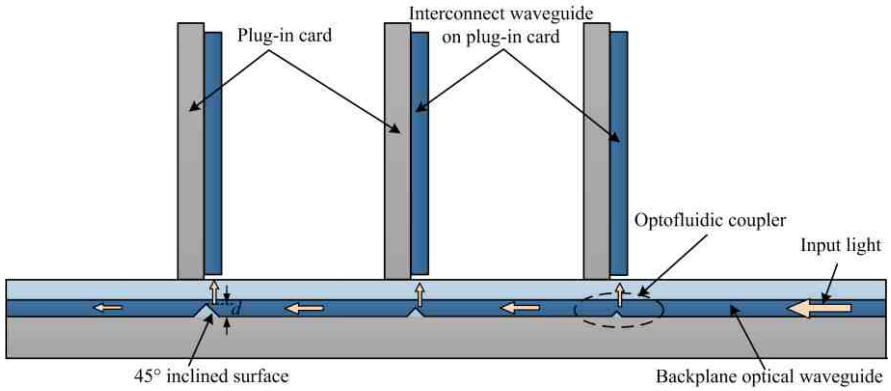

(a)

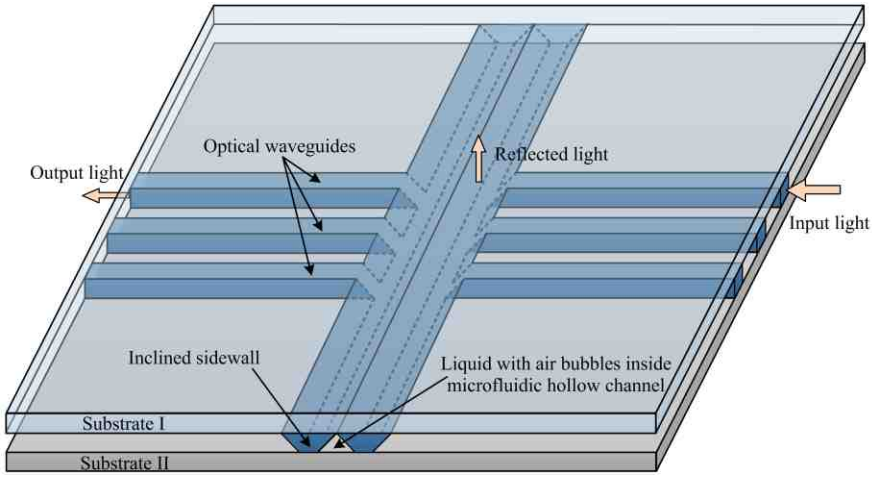

(b)

Fig. 5.2. Schematic illustration of (a) dynamic card-to-backplane optical interconnection and (b) tunable optofluidic coupler.

The activation (ON) and deactivation (OFF) of the optofluidic coupler can be accomplished by controlling the position of air bubbles and index matching liquid in the microfluidic channel for refractive index modulation. When the card is plugged in, we can move the air bubble to the mirror to activate the optofluidic coupler through total internal reflection. When the card is not plugged in, we can move the index matching liquid to the mirror to deactivate the coupler. As a result, the optical signal beam in the backplane waveguide is not wasted by unwanted surface normal coupling. The surface

normal optical coupling efficiency is set by the size of the waveguide mirror. Because of the mirror based optical coupling, the coupler is wavelength and polarization insensitive. It has also low sensitivity to waveguide modes because of the large overlapping of the mirror to the waveguide modes.

5.1 Simulation of Operation of Optofluidic Coupler

To validate the proposed optofluidic coupler concept, we first performed numerical simulation. The depth *d* of the 45° inclined surface (in Fig. 5.2(a)) determines the percentage of light in the waveguide to be reflected to the surface normal. The optofluidic coupler was turned ON and OFF by controlling the air or glycerol (refractive index 1.47) in contact with the inclined surface inside the microfluidic hollow channel. To simulate the operation of tunable optofluidic coupler, we used a ray tracing method to examine the reflected light power and output light power (see Fig. 5.2(b)) compared to the input light power at both the ON and OFF states. The light source used for the simulation is an 850 nm vertical cavity surface emitting laser (VCSEL) with half divergent angle of 5° and an aperture size of 10 μm [46]. The refractive indices of the core and cladding layer are 1.515 and 1.5, respectively. The refractive index of the liquid used for turning OFF the coupler is 1.47. The optical waveguide is 50 μm in width and 40 μm in height. The input waveguide has a length of 10 mm to stabilize the coupling condition. The simulation result is given in Fig. 5.3. When the coupler was ON and the depth of the inclined surface is increased from 0 to 40 μm, the reflected light power ratio can be dynamically tuned from 0% to near 100%. Most of the remaining light will pass through the coupler to the output and there will be about a 3% total loss, on average. When the coupler is OFF, the

input light cannot be reflected by the optofluidic coupler and about 95% of this light will pass through the coupler to the next coupler, on average. There are three optofluidic couplers with 13 μm, 20 μm, and 40 μm depth of inclined surface for three output ports to be examined in our experiment, respectively. Coupler I (13 μm) and Coupler II (20 μm) can be turned ON and OFF to control the percentage of reflected light from 33% and 50% to 0% and 0%, respectively. Coupler III (40 μm) was always turned on for total reflection.

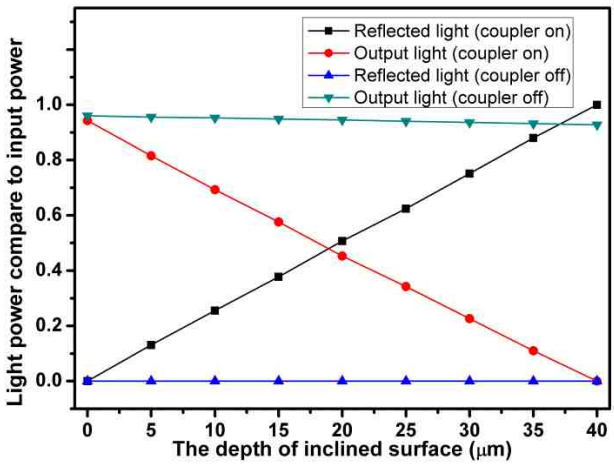

Fig. 5.3. The reflected light power and output light power compare to input light power as a function of the depth of incline surface at on and off states.

5.2 VAM Soft Lithography Fabrication

VAM as a new microfluidic based replication technique as mentioned earlier and has been used for polymer optical waveguide fabrication. It can be utilized to realize complex devices incorporating different materials in the same waveguide layer and to improve the performance of imprinted devices by eliminating the residue planar layer [71, 72]. The VAM soft lithography fabrication of polymer waveguides requires a PDMS mold with microfluidic hollow channel structures to guide the polymer resin flow. We have

designed the new polymer waveguides with optofluidic couplers. According to the design, a master pattern with the structures of channel waveguides, the 45° slanted surfaces, and the perpendicular microfluidic channel structures, is fabricated by prism-assisted inclined UV lithography. A PDMS mold with microfluidic hollow channels, which is a negative imprint from the master pattern, can be subsequently created. The desired waveguides with integrated mirrors and microfluidic channels structures are then realized via VAM soft lithography using synthesized UV curable resins. The whole process of PDMS mold fabrication and polymer waveguide imprint are schematically illustrated in Fig. 5.4.

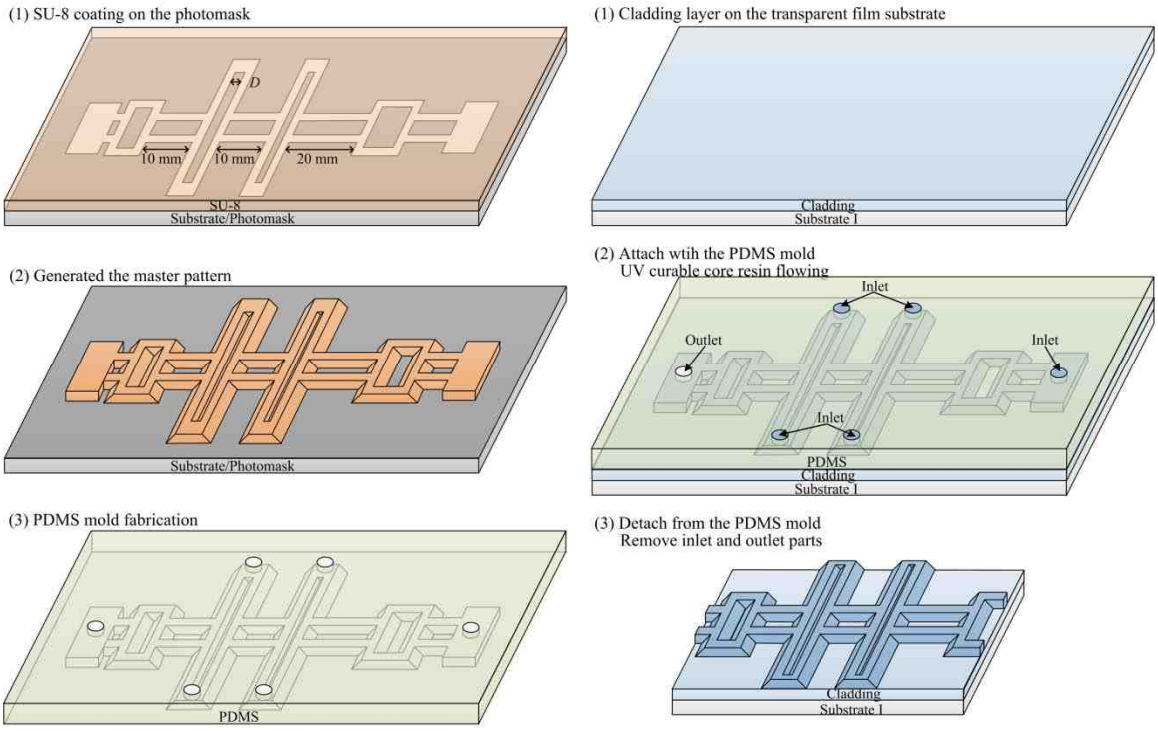

(a) (b)

Fig. 5.4. Schematic illustration of the process of (a) PDMS mold fabrication and (b) polymer waveguide and microfluidic channel structure imprint.

The process of PDMS mold fabrication is schematically shown in Fig. 5.4(a), which is similar to Fig. 4.1. A UV transparent glass, which also bears a prepatterned photomask

layer, was used as the substrate. The distance D between the two adjacent parts in each waveguide can be adjusted to control the depth of the resulting inclined surface to be 13 μm, 20 μm, and 40 μm. The designed size of the waveguide structures on the photomask was 50 μm in width, with a 20 mm length from input to the first coupler, 10 mm length from the first coupler to the second coupler, and 10 mm length from the second coupler to the third coupler (see Fig. 5.4(a)(1)). The lengths of the two perpendicular microfluidic channels are made longer in the present design for easy operation. The photoresist SU-8 2035 (MicroChem) was spin coated on the substrate/photomask with a thickness of 40 μm followed by pre-baking. The inclined UV lithography assisted by a right angle prism with 54° incident angle was then performed to achieve the needed 45° exposure in the SU-8 photoresist. 45° inclined surfaces on all ends of the waveguide structures were formed by increasing UV exposure time through internal UV surface reflection. The accurate patterns can be accomplished through this back-side UV exposure due to the intimate contact between the substrate/photomask and the SU-8. Followed by subsequent post baking and photoresist developing, we obtained the SU-8 master consisting of waveguide channel patterns with 45° inclined surfaces and the perpendicular microfluidic channel with inclined sidewalls. The fabricated master was then transferred to the PDMS mold. It was prepared by pouring liquid PDMS on the master which was encased by aluminum freezer tape. After setting at 85°C for 3 hours, the PDMS mold was then peeled off and inlet and outlet holes were then subsequently drilled for VAM.

Fig. 5.4(b) illustrates the VAM fabrication process of the polymer waveguide and microfluidic channel structure imprint. Suitable UV curable polymer resins for core and cladding materials were synthesized for this process, and the refractive indices at 850 nm

were found to be 1.515 and 1.500, respectively. A cladding resin layer of about 20 μm thickness was spin coated on the OC Grade Polymer Film (Grafix Plastics) used as a flexible transparent substrate and was followed by a 2 minute UV curing (100 mW/cm^2). The fabricated PDMS mold was then placed in conformal contact with the cladding layer. The synthesized UV curable core waveguide resin was then injected into the inlet holes from right to left sequentially and followed by suction to the outlet hole at left to propagate the resin throughout the PDMS hollow channels. The flow speed was controlled to around 2 mm/min through vacuum adjustment for an improved performance of the fabricated polymer structures. Following a 4 min UV curing at the same 100 mW/cm^2 power level, the PDMS mold was removed to reveal the imprinted polymer waveguides and the microfluidic channel structures. The inlet and outlet parts were then removed (see Fig. 5.4(b)(3)).

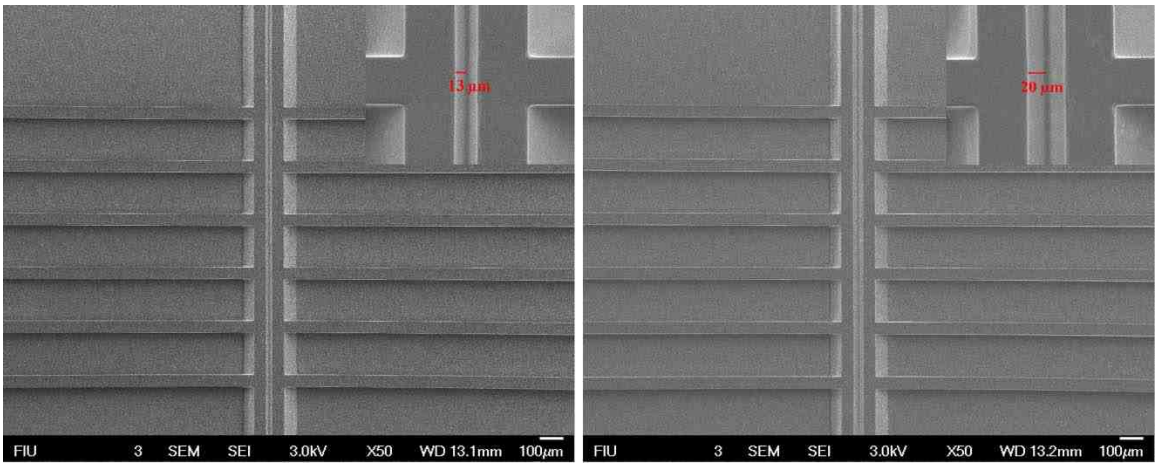

(a) (b)

Fig. 5.5. SEM images of the fabricated polymer waveguide and microfluidic channel structure with (a) 1/3 mirrors and (b) half mirrors.

Fig. 5.5 shows the SEM images of the fabricated polymer waveguides and perpendicular inclined sidewalls. The inclined surface depth is designed for different light coupling efficiencies. Fig. 5.5(a) presents the top view of a 1/3 depth (13 μm) inclined mirror surface (1/3 mirror), while Fig. 5.5(b) shows the top view of a half depth (20 μm) inclined mirror surface (half mirror).

5.3 Tunable Optofluidic Coupler

The optofluidic coupler can be formed by attaching the fabricated polymer optical waveguides and the perpendicularly oriented microfluidic channel with a substrate layer. A flat PDMS film was used as the substrate layer (Substrate II) for demonstration in our experiment. Fig. 5.6 shows the image of the whole system with three optofluidic couplers (coupler I, coupler II, and coupler III), which contain microfluidic channels with 1/3 mirrors, half mirrors, and full mirrors for the surface normal coupling, respectively. The transverse length of microfluidic channels of coupler I and II is expanded for easy operation. Holes were drilled on the substrate I at both ends of microfluidic channels and tubes are set up on the top of holes for liquid injection and suction.

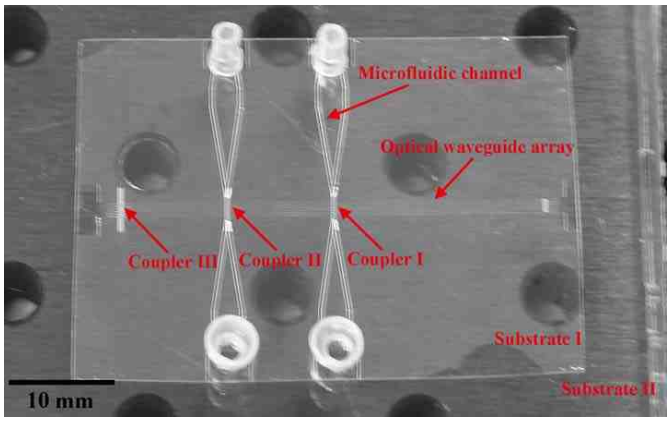

Fig. 5.6. Image of the whole system with waveguide array and three optofluidic couplers.

The tunable optofluidic couplers were realized by refractive index modulation through a positional realignment of air bubbles and index matching liquid in contact with waveguide mirrors. The index matching liquid (glycerol) and air bubbles were both inside the two microfluidic channels. The position of the air bubbles can be easily controlled by suction applied to one end of the microfluidic channel.

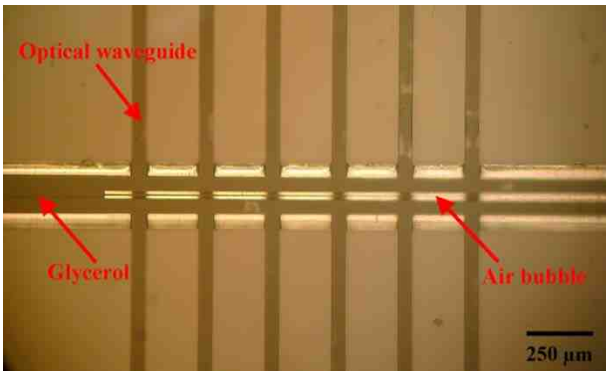

(a)

(b)

Fig. 5.7. Optical micrographs of the operation of tunable optofluidic coupler (a) air bubble contact with waveguide mirrors (b) glycerol contact with waveguide mirrors.

When the air bubble was located at the integrated waveguide mirrors (see Fig. 5.7(a)), the optofluidic coupler was activated via total internal reflection and a portion of the propagating waveguide signal beam was out coupled in the surface normal direction to a waveguide on a plug-in card. The remaining waveguide beams passed to the next coupler

sections for surface normal optical interconnect coupling. When applying a suction to the other end of the microfluidic channel (right side in Fig. 5.7(b)), glycerol was moved to be in contact with the waveguide mirrors (i.e. the air bubble was moved away to right). As a result, the optofluidic coupler was deactivated and most of propagating waveguide signal beams were delivered to the next couplers. Here, we controlled the 6-channel backplane waveguide array together, while the bubble array generated by T-junction or flow-focusing methods [110-112] can be used for independent control of each waveguide.

5.4 Optical Test of Dynamic System

The dynamic optical couplings of this card-to-backplane optical interconnect system have been demonstrated. Coupler I and Coupler II were turned ON and OFF by positional control of the air bubbles and glycerol in contact with waveguide mirrors. Coupler III was always ON for total reflection. To observe the operation of this dynamic system, a visible 632.8 nm wavelength laser beam was coupled into the backplane waveguide through a 45° mirror at right of Fig. 5.6 by a standard 9/125 μm SMF.

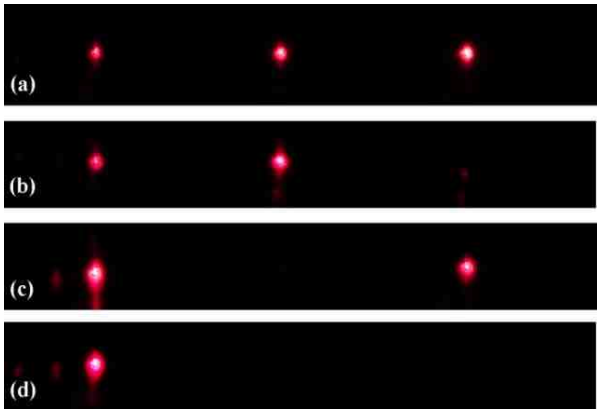

Fig. 5.8. ON/OFF operation of the optofluidic couplers. The interconnect beam in the waveguide is propagating from right to left.

Fig. 5.8 demonstrates the operation of this optical bus system with light coupling from one backplane waveguide from right to left. Fig. 5.8(a) and (b) show the activation and deactivation of coupler I, while coupler II is activated. Fig. 5.8(c) and (d) show the activation and deactivation of coupler I, when coupler II is deactivated.

An interconnect beam of 850 nm laser light was then coupled into the waveguide in the same way for optical test. The output intensity from the integrated mirrors of optofluidic couplers was measured by a Si photodetector above each output mirror. The coupled output power (normalized to the input power) reflected by coupler I and II when activated and deactivated is shown in Fig. 5.9. Fig. 5.9(a) gives the reflected power from coupler I when it is activated (black square) or deactivated (red circle). Fig. 5.9(b) shows the reflected power from coupler II when it is activated (black square) or deactivated (red circle) while coupler I was kept ON. Therefore, there is about 23 dB decrease of light signal intensity from activation to deactivation for both couplers I and II.

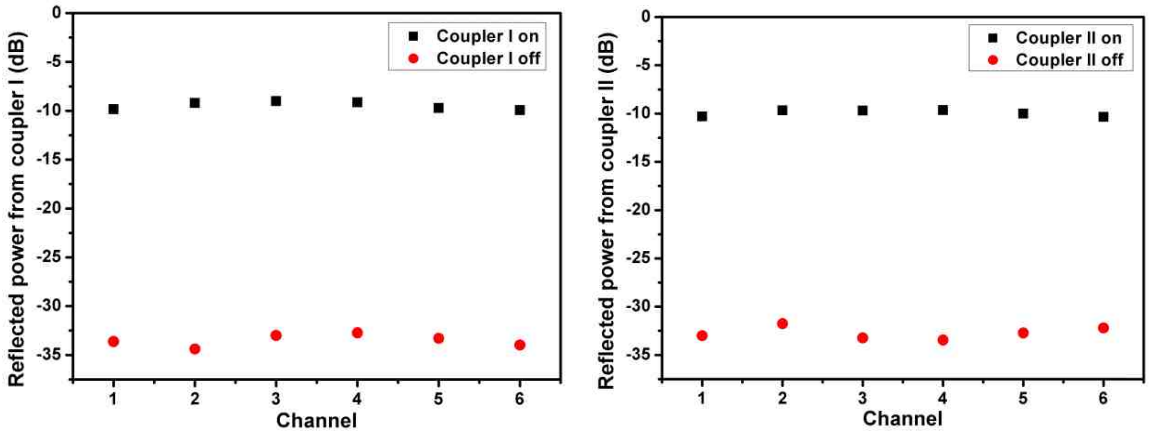

(a) (b)

Fig. 5.9. Reflected power from (a) coupler I with 1/3 mirrors and (b) coupler II with half mirrors when activated (black square) or deactivated (red circle).

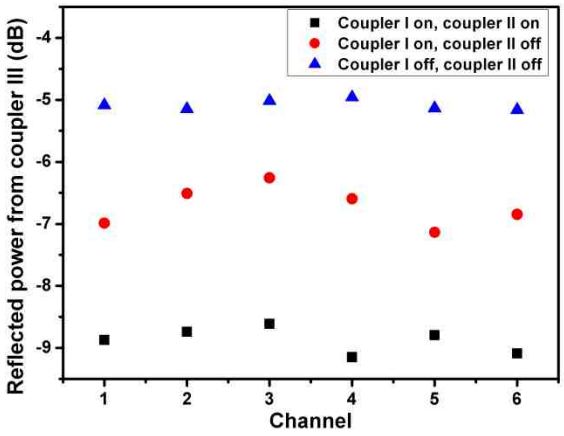

Fig. 5.10. The change of reflected power from the coupler III.

Fig. 5.10 shows the variance of reflection power of coupler III when the first two couplers are turned ON and OFF. First, couplers I and II were kept ON and the signal beam was delivered to all three plug-in-cards. The coupling intensity of coupler III is shown as black square. If a second card was not plugged in, coupler II would be deactivated and coupler III could reflect more of the optical signal (red circle). If the first card was also not plugged in, coupler I would be deactivated and most of the propagating waveguide signal would be reflected by coupler III (blue triangle). The average insertion loss for the 6 channels of the system was about -4.6 dB and -5.1dB when both couplers I and II were ON and OFF, respectively. The propagation loss for polymer waveguide fabricated using VAM lithography method was found to be -0.24 dB/cm [51]. And the coupling efficiency for a full mirror fabricated by the same method was found to be 75%. Therefore, the insertion losses of an optofluidic coupler are about -1.14 dB and -0.82 dB when it is ON and OFF, respectively, assuming coupler I and coupler II has the same insertion loss. The differences of refractive index between glycerol (1.47) and the polymer waveguide (1.515) may result in some reflection when the coupler is expected to be OFF. Therefore, a more suitable index matching liquid with a refractive index closer

to that of the polymer waveguide would help improve the performance of the optofluidic coupler. The surface normal out coupling is expected to experience beam divergence. Microlenses may be integrated over these 45° mirrors [41] to improve the performance of optofluidic couplers.

5.5 High Speed Test

To characterize high-speed data transmission of optical interconnect system, eye diagram analysis was performed. An eye diagram is widely used as a tool for understanding signal impairments in the physical layer of high-speed digital data systems in terms of amplitude and time distortion. A properly constructed eye diagram should contain every possible bit sequence from simple alternate 1's and 0's to isolated 1's after long runs of 0's, and all other patterns that may show up weaknesses in the design. In Fig. 5.11, the bit sequences 000, 100, 010, 110, 001, 101, 011, and 111 are superimposed over one another to obtain the final eye diagram. Several parameters and characteristics can be derived through an eye diagram for system performance measurement, such as Q factor, bit-error-rate (BER), eye opening factor, jitter, and rise and fall time.

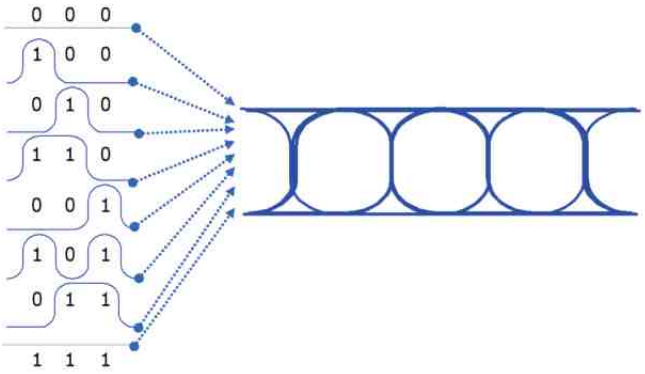

Fig. 5.11. Bit sequences are superimposed over one another to obtain the final eye diagram.

The Q factor is a measure of the signal eye aperture. It can be approximated by the equation

$$Q = \frac{\mu_1 - \mu_0}{\sigma_1 + \sigma_0} \quad , \tag{5.1}$$

where μ_1 and μ_2 are mean value of one level and zero level, and σ_1 and σ_2 are noise distribution of one level and zero level, respectively.

BER is number of bit errors divided by the total number of transferred bits during a studied time interval. The bit errors result from the noise, interference, distortion or bit synchronization errors. BER is an important gauge in communication applications, which can be predicted by

$$BER = \frac{1}{\sqrt{2\pi}} \frac{e^{-Q^2/2}}{Q} \quad , \tag{5.2}$$

if assuming presence of Gaussian distributed noise.

Jitter is defined as the time deviation from the ideal timing of a data-bit event, which results from the misalignment of rise and fall times. It becomes one of the most important topics and a fundamental performance limit when high-speed digital signals are transmitted. The p-p jitter is defined as the full width of the time histogram, as shown in the Fig. 5.12.

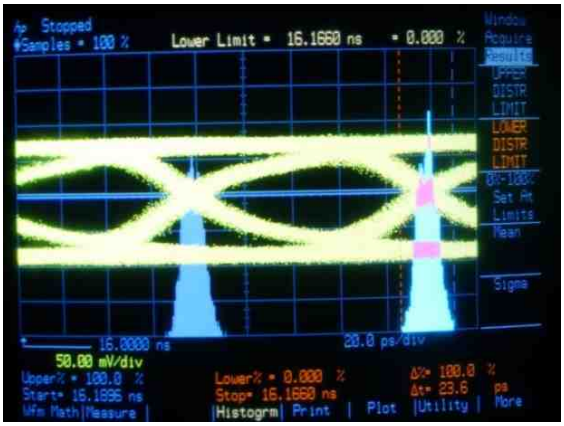

Fig. 5.12. The full width of the time histogram for p-p jitter.

Optical test at 10 Gbps was carried out at 850 nm wavelength for the high speed performance degradation. The schematic setup and experimental setup of high speed test are shown in Fig. 5.13. The OTB3P1A pseudo random bit sequence (PRBS) generator (from Centellax) was used to generate 2^{31}-1 random pattern length with mark density ratio of ¼ in the test. A testboard with VCSEL and photodetector operating at 850 nm meets the performance requirements for 10 Gbps data communication. An HP 8637H signal generator (2.0-12.4 GHz) was used to modulate the laser, and an HP 54120B digitizing oscilloscope (12 GHz) was employed to capture the received signal.

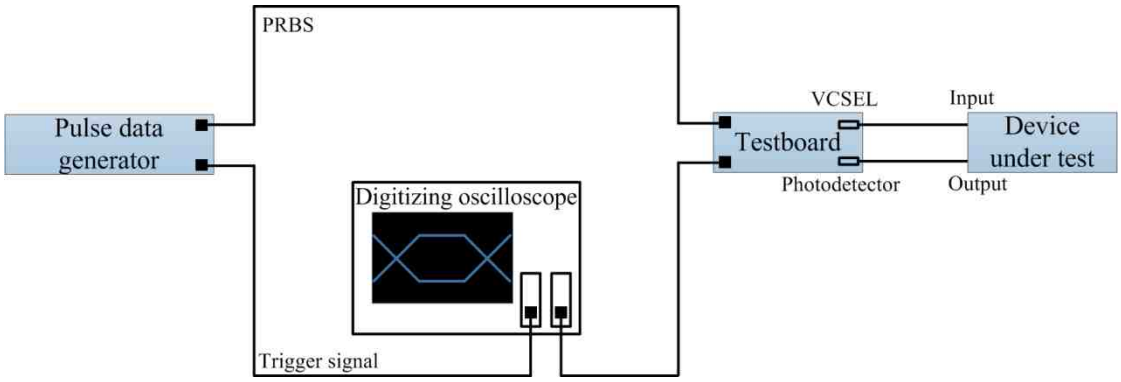

(a)

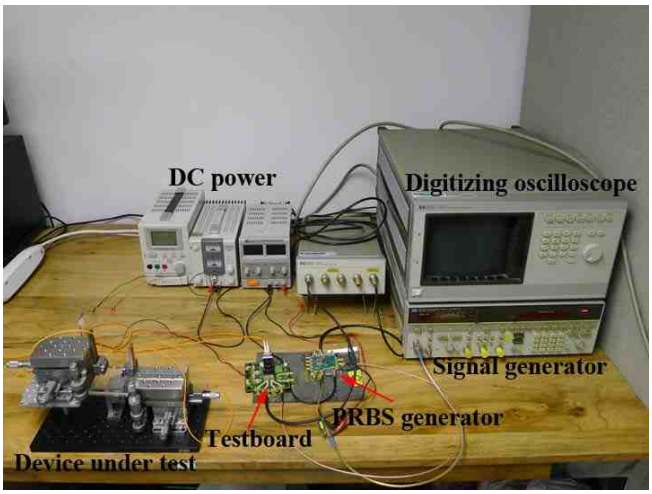

(b)

Fig. 5.13. (a) Schematic setup and (b) experimental setup of high speed test.

Fig. 5.14 shows two 10 Gbps eye diagrams with Q-factors of 5.4 and 5.7 for coupler III when coupler I and II were both activated or deactivated. The corresponding BER were calculated to be 3.44×10^{-8} and 6.16×10^{-9}, respectively, assuming Gaussian distributed noise. When both couplers I and II were deactivated, we received a higher Q factor of coupler III which may result from the higher power reflected from coupler III.

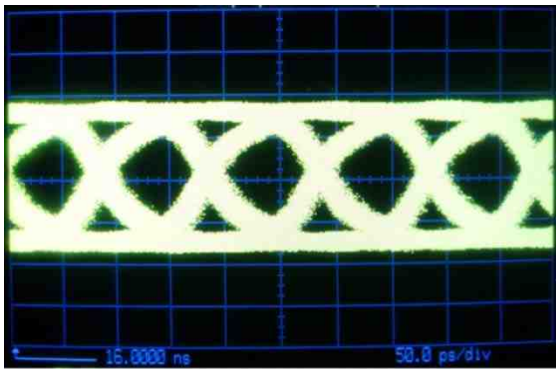

(a)

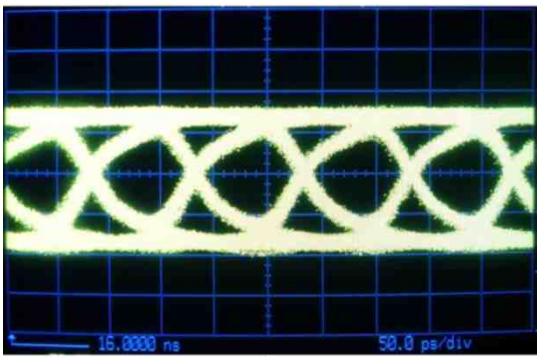

(b)

Fig. 5.14. Measured 10 Gbps eye diagrams for coupler III when both couplers I and II were (a) activated and (b) deactivated.

5.6 Summary

We have reported on tunable optofluidic couplers fabricated by the VAM soft lithography technique for dynamic card-to-backplane optical interconnects. The tunable optofluidic

couplers consist of polymer waveguides with 45° integrated waveguide mirrors and perpendicular microfluidic channels for movement of air bubbles and index matching liquid for mirror on/off modulation. The activation or deactivation of the surface normal coupling of the optofluidic coupler was performed by setting air bubbles or glycerol to be in contact with the waveguide mirrors. A 23 dB surface normal signal contrast was achieved through the activation and deactivation of the optofluidic coupler. Successful backplane waveguide signal transmission and surface normal coupling through the optofluidic couplers have been demonstrated with a 10 Gbps eye diagram observed showing a high performance optical interconnection system. The optofluidic based dynamic card-to-backplane optical interconnect supports shared bus topology and can save the optical signal power when the card is not plugged in. The control of the optical coupler efficiency is effective yet the cost of fabrication via VAM is low. The fabricated tunable optofluidic couplers offer new photonic components that may be used for dynamic card-to-backplane optical interconnect applications as well as various integrated planar lightwave circuits.

Chapter 6

Planar Concave Grating Wavelength Demultiplexer for Optical Interconnection and Integrated Optical Coherence Tomography

Lithographically fabricated polymer waveguides have a broad range of planar lightwave circuit based applications. We have demonstrated earlier our innovative design and useful implementation of optofluidic couplers for card-to-backplane optical interconnection. Herein, we explore its practical application in wavelength multiplexer and demultiplexer as well as integrated spectrometer.

The demand of high aggregate bandwidth for optical communication and interconnection promotes the rapid development of the waveguide WDM system [113]. The WDM technique combines multiple optical carrier signals on a single optical fiber with different wavelengths as different signal carriers. This is an effective and low cost method to dramatically increase the capacity of optical communication. The key optical components in the WDM system are optical multiplexers and demultiplexers. The different signal wavelengths are joined together at the input of the system by the multiplexers and split apart at the output of the system by the demultiplexer. The lithographically fabricated polymer waveguides can meet these communication requirements with low cost. We present herein our design of planar concave grating wavelength demultiplexer for WDM system using the polymer waveguides and the fabrication techniques mentioned earlier.

By changing the channel numbers and wavelength band selection, the polymer waveguide based wavelength demultiplexer can become an integrated spectrometer, which can replace the bulky conventional spectrometer component in an SD-OCT system as discussed earlier. We also present herein our design of a 200-channel PCG spectrometer with 0.5 nm channel spacing and a 1024-channel PCG spectrometer with 0.1 nm channel spacing for SD-OCT system applications.

An alternative solution to support a compact and portable SD-OCT is designing a compact spectrometer by minimizing the beam expansion perpendicular to the spectral dispersion plane as originally planned by using integrated optics. All the optical components can be cut down to 3 mm to yield the compact spectrometer. The compact spectrometer system has been used in our SD-OCT system and it has demonstrated the desired spectrometer performance.

6.1 Planar Concave Grating based on SU-8 Polymer Waveguides

6.1.1 SU-8 Polymer Waveguide

While there are many polymer material candidates that can be used for WDM and integrated spectrometer implementation, SU-8 polymer is presently selected because of its easy fabrication and relatively good chemical and thermal stabilities [64, 85, 114]. SU-8 polymer is typically used as negative photoresist for UV lithography. For our PCG based wavelength demultiplexer device design, Fig. 6.1 shows the cross section view of a small SU-8 strip waveguide with a width of w_{co} and a height of h_{co}. The polymer strip waveguides with air top cladding are preferred for high index contrast and high density integration. The waveguide has OE4141 (Dow Corning) photopolymer bottom cladding

on a Si substrate. The refractive indices of SU-8 and OE4141 are 1.575 and 1.494, respectively at 1310 nm wavelength. The OE4141 cladding layer is about 8 μm thick to avoid waveguide mode leakage to the Si substrate.

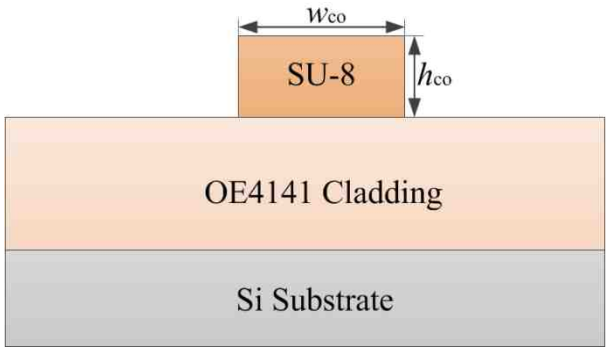

Fig. 6.1. Cross section of a small SU-8 strip waveguide.

Fig. 6.2 shows the single-mode condition for TE (transverse electric) polarization at 1310 nm wavelength. We vary the core width w_{co} and height h_{co} step by step using finite-difference (FD) method for mode solution to determine mode condition and its cutoff boundary of the fundamental and first-order modes. The area between the two curves can support single-mode propagation. This figure can be used to select device parameters to ensure the single-mode condition is met.

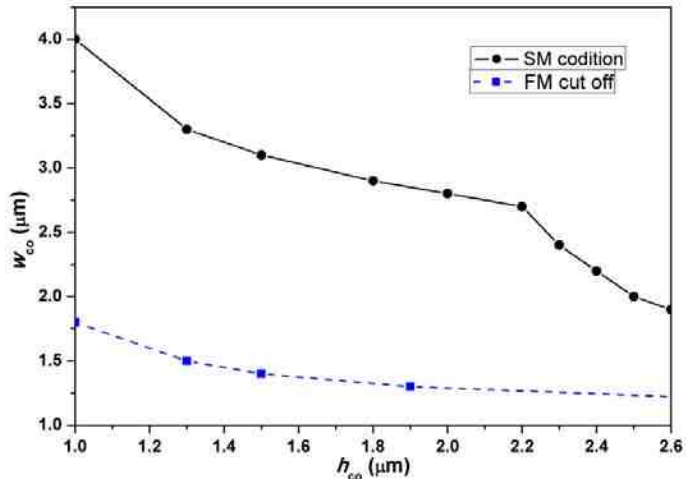

Fig. 6.2. Single-mode (SM) condition and fundamental mode (FM) cutoff.

The single-mode and multi-mode boundary is given by the black solid line. The first-order mode cuts off at a certain aspect when its effective refractive index n_{eff} is equal to the refractive index of the bottom cladding layer. There is a turning point at h_{co} of 2.2 μm. When h_{co} is less than 2.2 μm, the first-order mode is the mode E_{21} with two peaks in the lateral direction and one peak in the vertical direction. When h_{co} is larger than 2.2 μm, the mode E_{12} becomes the first-order mode with two peaks in the vertical direction and one peak in the lateral direction. When the point (w_{co} and h_{co}) is above the boundaries, there is more than one guided mode in the waveguide. The fundamental mode cuts off at a certain aspect (blue dash line) when its effective refractive index n_{eff} is equal to the refractive index of the bottom cladding layer. When the point (w_{co} and h_{co}) is below the fundamental mode cutoff boundary, there is no guided mode supported in the waveguide. Clearly, the waveguide is single-mode when the size parameter falls in between the two curves.

For our device design, we select the width and height of the single mode strip waveguide to be w_{co} = 2.5 μm and h_{co} = 2 μm. The calculated fundamental (TE_{00}) mode profile is shown in Fig. 6.3.

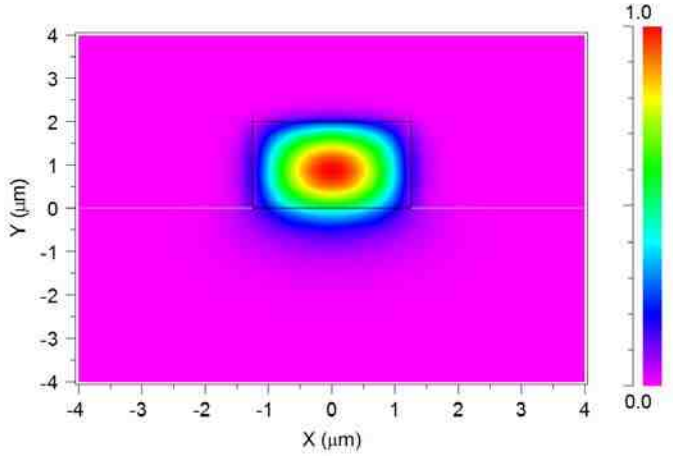

Fig. 6.3. Calculated fundamental (TE_{00}) mode profile.

6.1.2 Basic Theory of Planar Concave Grating

The planar concave grating structure is based on the conventional Rowland circle geometry [115] as illustrated in Fig. 6.4. The input and output waveguides are positioned along the Rowland circle with a radius *R*. The grating facets are located on a grating circle with a radius equal to the diameter of the Rowland circle. The grating circle and Rowland circle touch at the center of the grating.

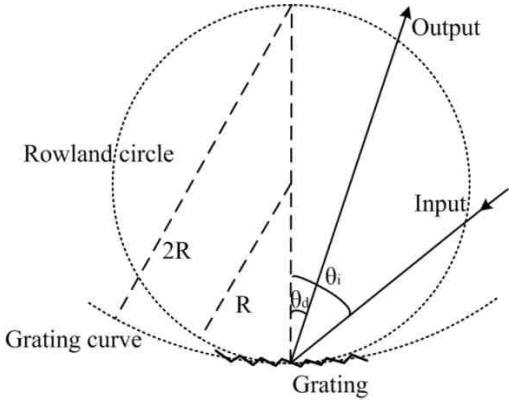

Fig. 6.4. Schematics with the Rowland configuration for PCG.

There is a planar waveguide region between the input/output waveguides and the concave grating. The input light diverges toward the grating in this planar free propagation region. The concave grating on the grating circle diffracts back and focuses the light into the output waveguides on the Rowland circle. The positions of input and output waveguides are determined by the grating equation [31, 116]

$$d(sin\theta_i + sin\theta_d) = m\frac{\lambda}{n_{eff}} \tag{6.1}$$

where θ_i and θ_d are the incident and diffracted angles with respected to the grating circle normal at the center of the grating. d is the period of the grating, m is the diffraction order, λ is the wavelength in free space, and n_{eff} is the effective index of the planar waveguide mode at wavelength λ.

The free spectral range (*FSR*) for a given diffraction order *m* is the largest wavelength range that does not overlap the adjacent order *m*+1 or *m*-1, which can be approximately deduced from grating equation

$$FSR = \frac{\lambda}{m}. \tag{6.2}$$

We can choose the right order of grating *m* such that the *FSR* is greater than the spectral range of the device.

The linear dispersion (*LD*) can be deduced from grating equation as

$$LD = R\frac{\delta\theta_d}{\delta\lambda} = \frac{2Rm}{dcos\theta_d n_{eff}} \tag{6.3}$$

where the incident angle is constant, $\delta\theta_d$ is the differential change in diffracted angle, and $\delta\lambda$ is the differential change in wavelength. The radius *R* of Rowland circle can also be calculated if the linear dispersion *LD* is given from this equation.

6.1.2 Design and Simulations of PCG

The PCG wavelength demultiplexers are designed and fabricated based on SU-8 polymer waveguides, as we mentioned earlier. A 4-channel and 16-channel PCGs are selected for the demonstration. The optical waveguides for input and output of PCG have 2.5 μm width and 2 μm height. The PCG input and output channel waveguides have 300 μm long waveguide tapers that changes width from 5 μm apertures to 2.5 μm wide waveguide.

The design process starts with choosing the center wavelength λ_c of the spectral range of the device, which is 1310 nm wavelength in this study. The diffraction order *m* can be determined by the relationship between the diffraction order and the *FSR* from Eq. (6.2). The *FSR* has to be larger than the operation spectral range. The diffraction order is chosen to be *m* = 10 corresponding to a free spectral range of about 130 nm. The total

internal reflection facet is applied, which quite simplifies our fabrication process without the need in metal deposition. The incident and diffracted angles are chosen to be $\theta_i = 65°$ and $\theta_d = -25°$. The calculated grating period is $d = 17.4$ μm from Eq. (6.1). The 5 μm wide tapered output waveguides are spaced 10 μm apart on the Rowland circle.

The grating facets are chipped and blazed [117] in the design for better performance (higher peak transmission and lower crosstalk). We chose two points (p_1 and p_2) on a facet line equidistant from the facet center position (p_c) to determine the direction of the grating facet, as shown in Fig. 6.5(a). The path lengths for p_1 and p_2 are $m_1 + m_2$ and $n_1 + n_2$, respectively. We rotated the facet (about the facet center position, p_c) until the path difference between the two points becomes zero.

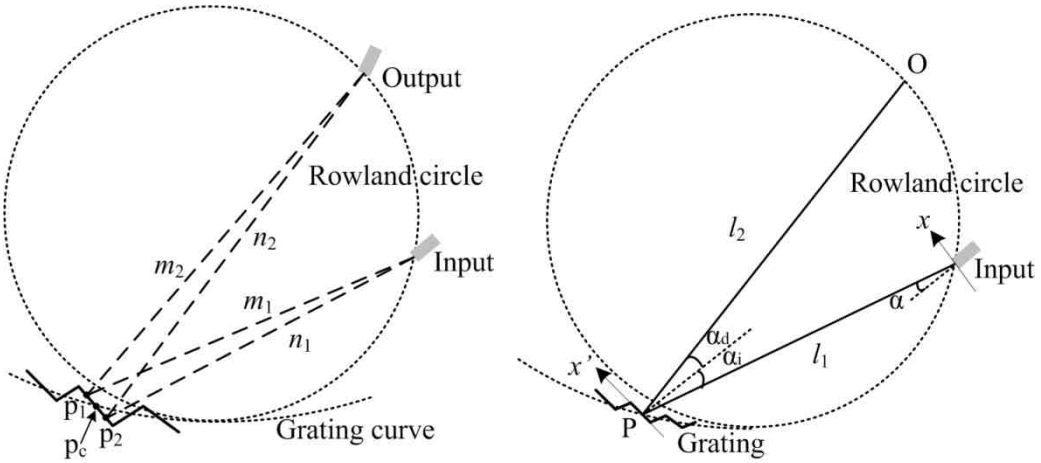

(a) (b)

Fig. 6.5. Schematic of a grating with (a) two paths and (b) coordinate system

For the 4-channel PCG, the designed central wavelengths of four output channels are 1280, 1300, 1320, and 1340 nm, with 20 nm spectral separations. The Rowland circle radius are calculated to be $R = 613.6$ μm from Eq. (6.3). For the 16-channel PCG, the wavelength spacing (channel spacing) $\delta\lambda$ is of 5 nm which results a 2.45 mm Rowland circle radius. The design data are summarized in Table 6.1.

Parameters	4-channel PCG	16-channel PCG
Center wavelength (λ_c)	1310 nm	1310 nm
Wavelength spacing ($\delta\lambda$)	20 nm	5 nm
Diffraction order *m*	10	10
Free spectral range (*FSR*)	130 nm	130 nm
Incident angle (θ_i)	65°	65°
Diffracted angle (θ_d)	-25°	-25°
Grating period (*d*)	17.4 μm	17.4 μm
Rowland circle radius (*R*)	613.6 μm	2.45 mm
Number of output waveguides (*N*)	4	16
Space of output waveguides	10 μm	10 μm

Table 6.1. The design parameters of 4-channel and 16-channel PCGs.

The PCG device simulation is performed based on the scalar diffraction theory [31]. A schematic of a grating with coordinate system is shown in Fig. 6.5(b). The incident electrical field at any points of the grating facets $E_{grating}$ can be calculated according to the Kirchhoff-Huygens diffraction formula

$$E_{grating} = \frac{1}{2}\left(\frac{n_{eff}}{\lambda}\right)^{1/2} \int_{input} \frac{E_{input} e^{-jkl_1}}{\sqrt{l_1}} (1 + cos\alpha) dx \tag{6.4}$$

where E_{input} is the electric field profile of the input aperture of PCG, α is the diffractive angle with respect to the normal input direction, l_1 is the distance between the input port and the point on the grating, and $k = 2\pi\, n_{eff}/\lambda$ is the wavenumber in the planar waveguide.

Similarly, the diffracted field E_{image} on the Rowland circle is the image of the input channel mode and calculated as

$$E_{image} = \frac{1}{2}\gamma\left(\frac{n_{eff}}{\lambda}\right)^{1/2}\int_{grating}\frac{E_{grating}e^{-jkl_2}}{\sqrt{l_2}}(cos\alpha_i + cos\alpha_d)dx' \tag{6.5}$$

where α_i and α_d are the incident and diffracted angles with respect to the normal direction of each grating facet, l_2 is the distance between each point on the grating and the point on the Rowland circle, and γ is the reflection coefficient of the grating.

The intensity I at the wavelength λ coupled into each output waveguide can be obtained by calculating the overlap integral between the output waveguide channel field profile and the diffracted and focused field by the PCG as

$$I(\lambda) = \frac{|\int E_{image}\cdot E^*_{outwg}dx'|}{\int|E_{image}|^2dx'\int|E_{outwg}|^2dx'} \tag{6.6}$$

where E_{outwg} and E^*_{outwg} are the fundamental mode and its conjugation of the output waveguide.

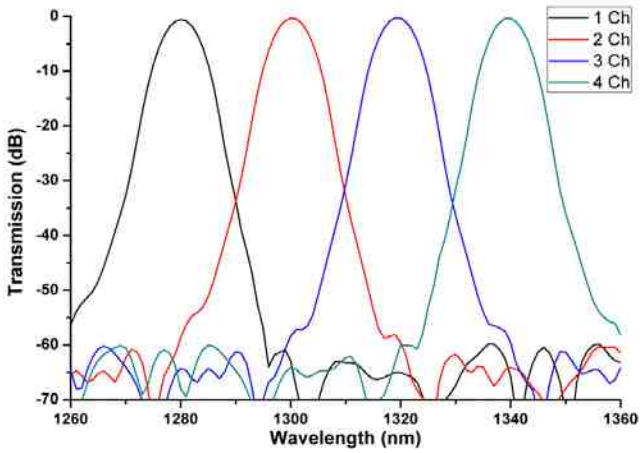

Fig. 6.6. Simulated spectral response of 4-channel PCG.

The field distribution at the end of the input taper is calculated by FD method as the input field of the PCG. The reflection coefficient of the grating γ is set to 1 because of the total internal reflection facets. The simulation spectral response of the designed 4-

channel PCG is shown in Fig. 6.6. The device exhibits a central channel loss of -0.25 dB, a crosstalk of -60 dB, and an on-chip loss non-uniformity of 0.27 dB.

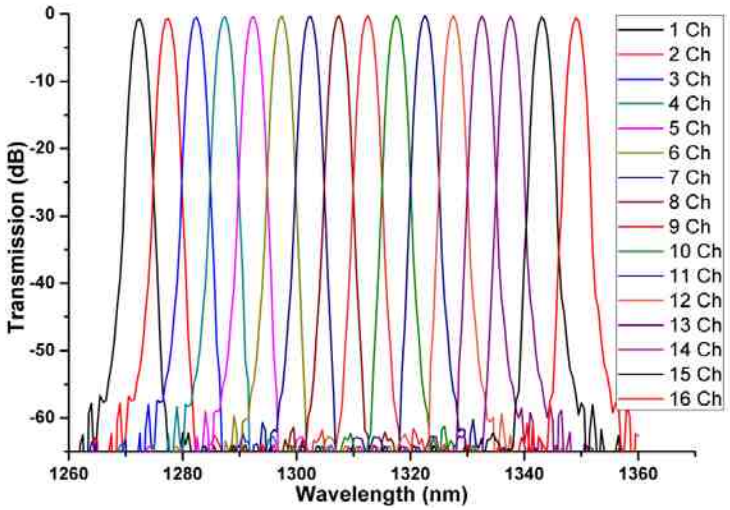

Fig. 6.7. Simulated spectral response of 16-channel PCG.

Fig. 6.7 presents the simulation spectral response of the designed 16-channel PCG. The device exhibits a central channel loss of -0.25 dB, a crosstalk of -57 dB, and an on-chip loss non-uniformity of 0.47 dB.

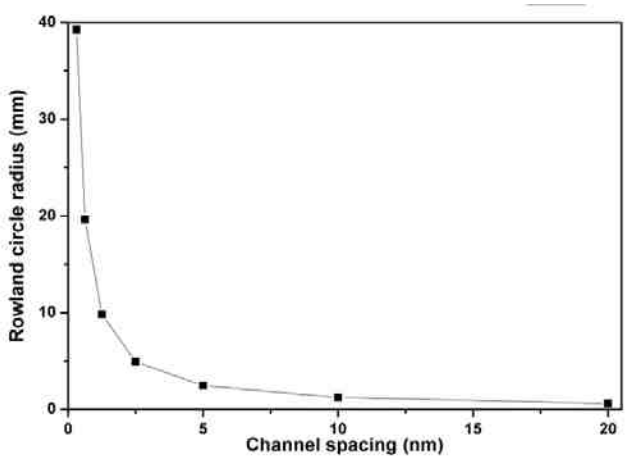

Fig. 6.8. The relationship between channel spacing and Rowland circle radius.

We can increase the channel number and decrease channel spacing by increasing the size of free propagation region (size of Rowland circle). Fig. 6.8 presents the relationship

between channel spacing and Rowland circle radius for the 4-channel PCG while keeping the same diffraction order, incident angle, and diffracted angle. When the channel spacing is as small as 0.5 nm, the Rowland circle radius should be as big as 24.5 mm.

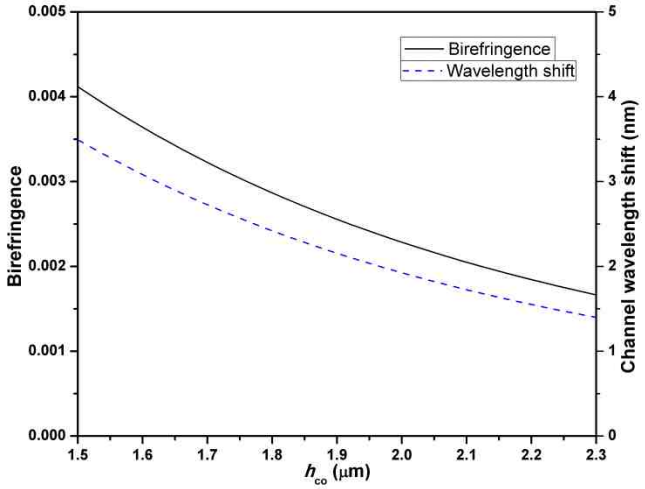

Fig. 6.9. The calculated values of birefringence and wavelength shift as a function of h_{co}.

The birefringence is defined as the difference between the effective indices of the TE and transverse magnetic (TM) polarization mode of the PCG slab region, which results in an unwanted shift in transmission spectra of two polarization states [117]. Fig. 6.9 shows the calculated values of birefringence and channel wavelength shift as a function of h_{co}. The TE-TM channel wavelength shift is 1.9 nm when h_{co} = 2 μm. In order to apply to dense WDM system and on-chip spectrometer system where wavelength spacing is 2 nm per channel or less, one way is to control the polarization state of the incoming light for the PCG device. Also, we can use a compensator section in the free propagation region to reduce the wavelength shift [28, 118, 119].

The characteristic of PCG is easily affected by profile imperfections, such as waveguide thickness and grating round corner. The change of waveguide thickness h_{co} alone will mainly result in center wavelength shift, as shown in Fig. 6.10. The rounding

of the grating teeth (radius *r*) will introduce the extra loss of the device, as presented in Fig. 6.11. There would be more than -2 dB excess loss of PCG device if the rounding radius *r* is greater than 1 μm.

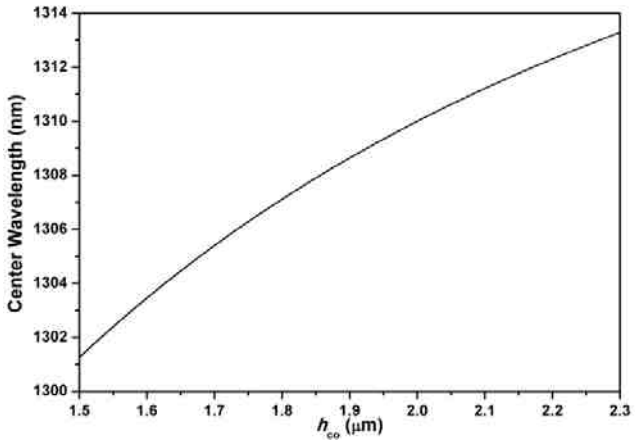

Fig. 6.10. The center wavelength shift as a function of waveguide thickness h_{co}.

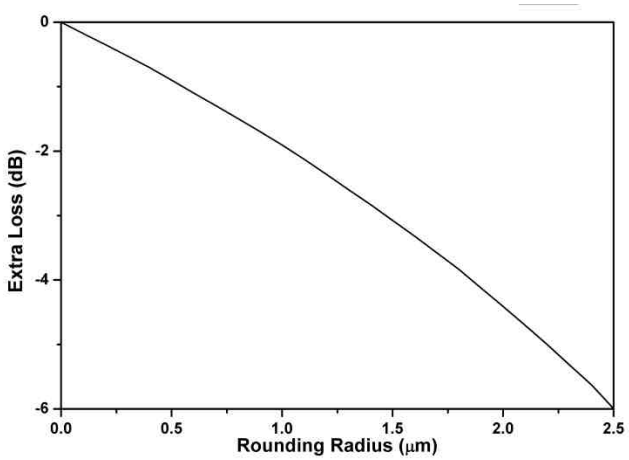

Fig. 6.11. Extra loss related to the rounding radius of grating teeth.

6.1.4 Planar Concave Grating Fabrication and Testing

To verify the device design, we fabricated PCG devices based on SU-8 polymer as illustrated in Fig. 6.12. Only a one-step UV lithography process is needed, which greatly simplifies the fabrication process. We first spin coated an 8 μm thick OE4141 cladding layer on a cleaned Si substrate and cured it by flood UV exposure. The 8 μm thick

OE4141 cladding layer has a very good optical property and is thick enough to avoid waveguide mode leakage to the Si substrate. A 2 μm thick SU-8 polymer film was then formed on the cladding layer by spin-coating. The Si wafer with SU-8 core layer was pre-baked (1 min @ 65°C and 1 min @ 95°C) on a hotplate to evaporate the solvent. Then the patterns on the photomask were transformed to the SU-8 film by i-line UV photolithography. The Si wafer with the exposed SU-8 film was then post-baked (1 min @ 65°C and 2 min @ 95°C) to finish the polymer cross-linking process. Following development and rinsing, the final device with the SU-8 planar and channel waveguides was obtained. A short hard baking time (1 min @ 65°C and 5 min @ 150°C) is generally preferred to smoothen the waveguide sidewalls and reduce the scattering loss while keeping the sidewall vertical [64]. The straight reference waveguides with 1.5, 2 , 2.5, 3 , and 5 μm widths were also fabricated at the same time.

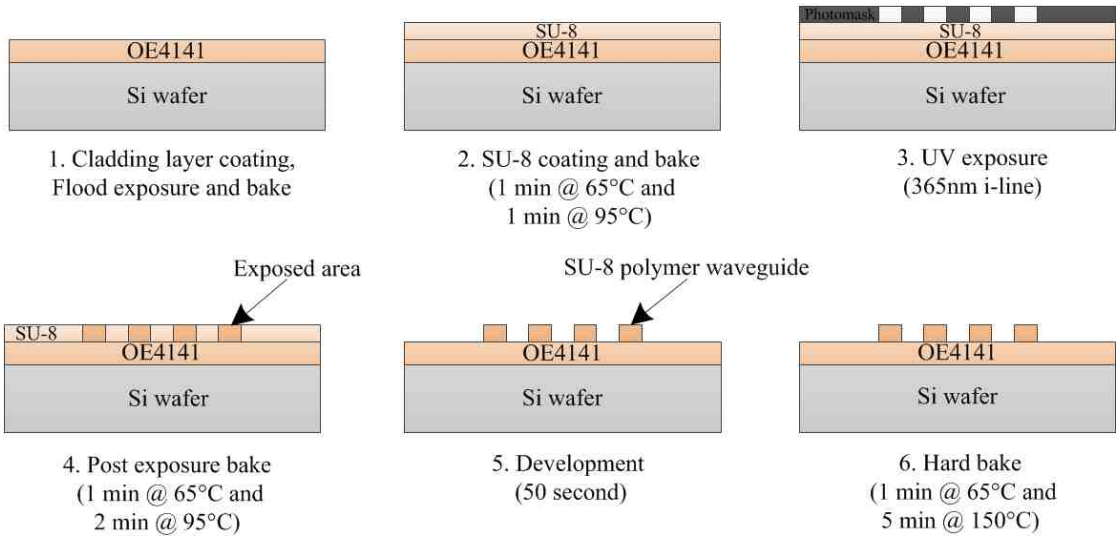

Fig. 6.12. PCG fabrication process.

Fig. 6.13(a) and (b) present the microscope images of the fabricated PCG and the magnification of the grating portion. The microscope images of cross section view of

straight reference waveguides and 4-channel output waveguides are shown in Fig. 6.13(c) and (d).

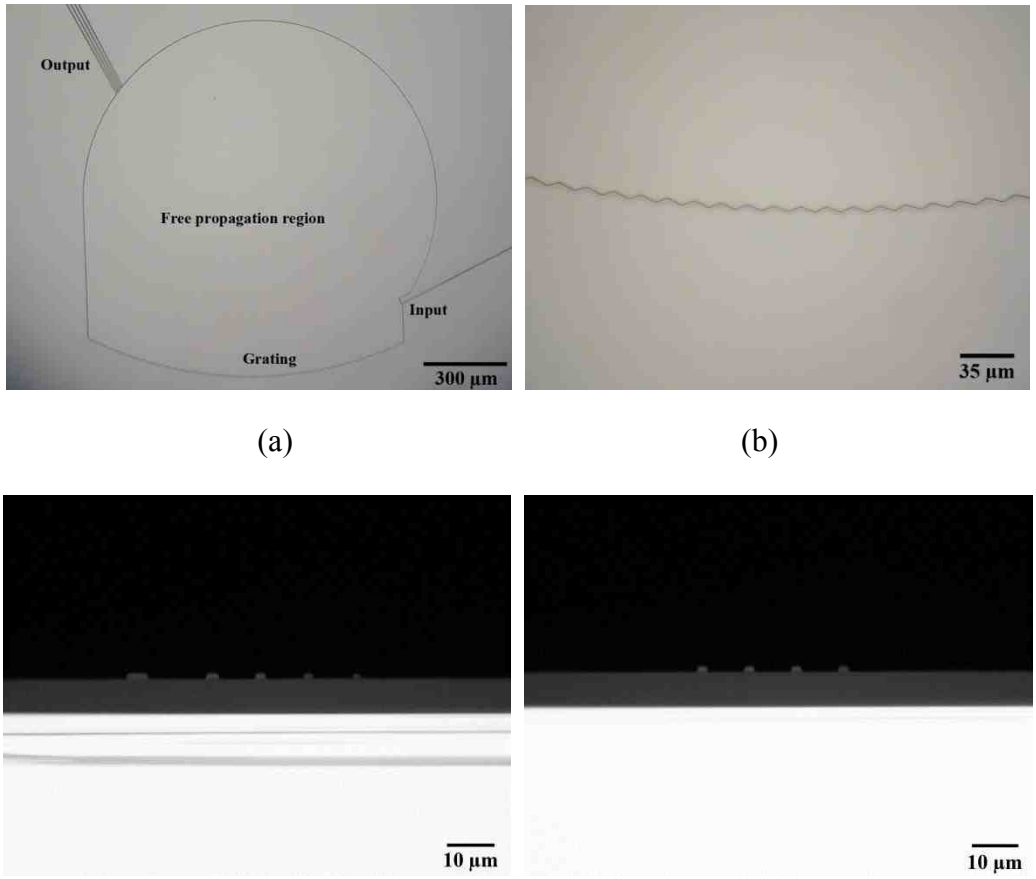

Fig. 6.13. Microscope images of (a) the fabricated PCG device, (b) the further magnified grating portion, (c) the cross section of straight reference waveguides, and (d) the cross section of 4-channel output waveguides.

A schematic of mode profile testing system is shown in Fig. 6.14(a). A light source with 1310 nm center wavelength was used to characterize the fabricated straight waveguides. The input light from the light source fiber was butt-coupled to the input waveguide through a taper lens fiber (TLF) with a focus spot size of about 2.5 µm. A 60× microscope objective lens was used to collect the output light from the end of the output

optical waveguides, which was connected to an infrared camera (Electrophysics Microviewer 7290). The output spot was observed and analyzed using a laser beam profiler (New Span Opto-Technology). The picture of the experimental setup is presented in Fig. 6.14(b).

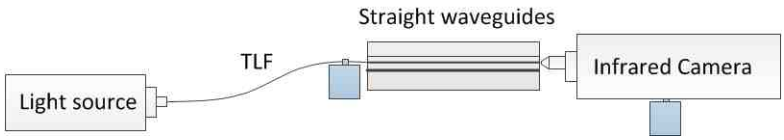

(a)

(b)

Fig. 6.14. (a) Schematic of waveguide mode profile testing system and (b) picture of the experimental setup.

The mode profiles of the 2.5 μm and 5 μm wide waveguides and their 3D intensity distribution are shown in Fig. 6.15. Fig. 6.15(a) and (b) presents the one peak Gaussian intensity distribution, indicating single-mode propagation in the fabricated 2.5 μm wide SU-8 ridge waveguide. Fig. 6.15(c) and (d) presents the multiple peaks intensity distribution, indicating multi-mode propagation in the fabricated 5 μm wide SU-8 ridge waveguide. These results agree well with the calculated single-mode condition.

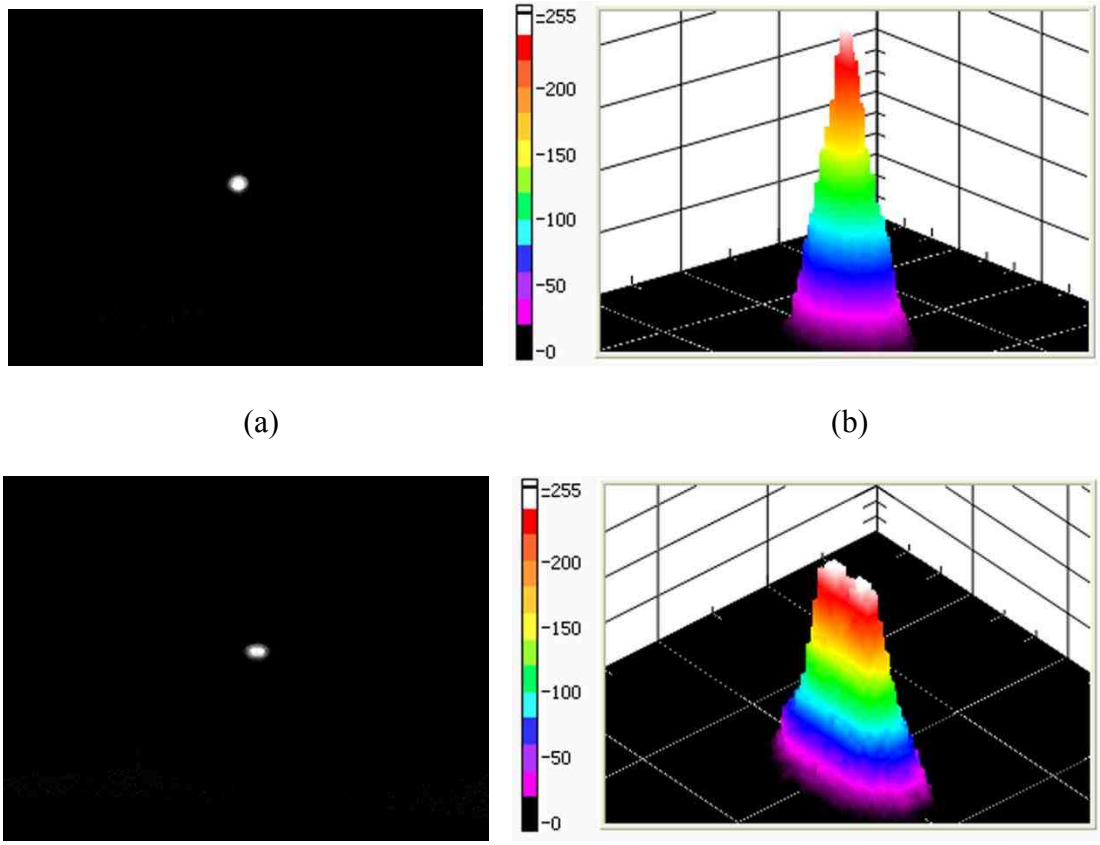

(a) (b)

(c) (d)

Fig. 6.15. Mode profiles of the 2.5 μm and 5 μm wide waveguides.

A schematic of PCG testing system is shown in Fig. 6.16(a). A broadband superluminescent diode light source was used to characterize the fabricated PCG devices. The input light from the light source fiber was butt-coupled to the input waveguide through a TLF with a focus spot size of about 2.5 μm. Another TLF was used to collect the output light from the end of the output optical waveguides, which was connected to an optical spectrum analyzer (Agilent 86142B). The picture of the experimental setup is given in Fig. 6.16(b). The propagation loss of a straight SU-8 waveguide of 2.5 μm width is about -0.6 dB/mm measured by conventional cut back method at 1310 nm wavelength, which may be mainly due to the large scattering loss from the waveguide sidewalls.

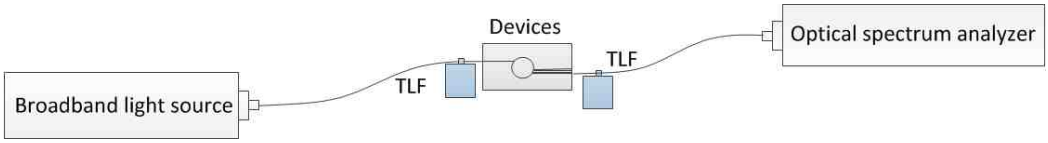

(a)

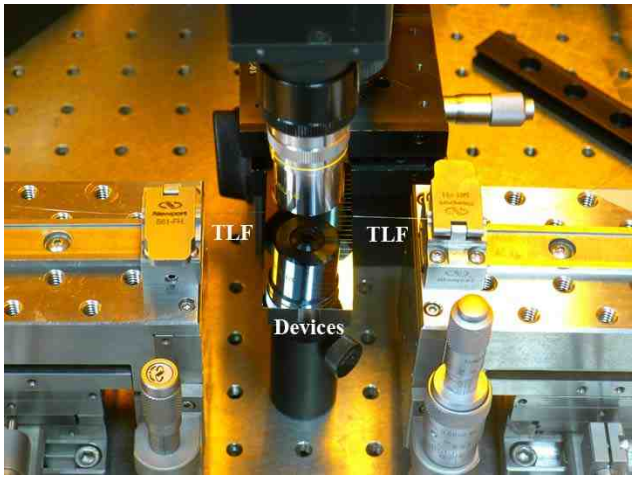

(b)

Fig. 6.16. (a) Schematic of PCG test system and (b) picture of the experimental setup.

The measured transmission spectrum of the fabricated 4-channel PCG is given in Fig. 6.17. The losses are normalized to a reference straight waveguide. The on-chip loss for the central wavelength is about -13 dB. The crosstalk of the fabricated device is -25 dB and the on-chip loss non-uniformity is 2.5 dB. The high on-chip loss and crosstalk may results from the grating round corner and non-vertical grating facet. There is about 10 nm spectral shift in the transmission spectrum toward short wavelength, which may be caused by the smaller height of the core waveguide layer and the slightly smaller effective refractive index in the planar waveguide comparing with the values used in the simulation. The spectral shift as a function of waveguide height is expected based on the simulation given in section 6.1.3.

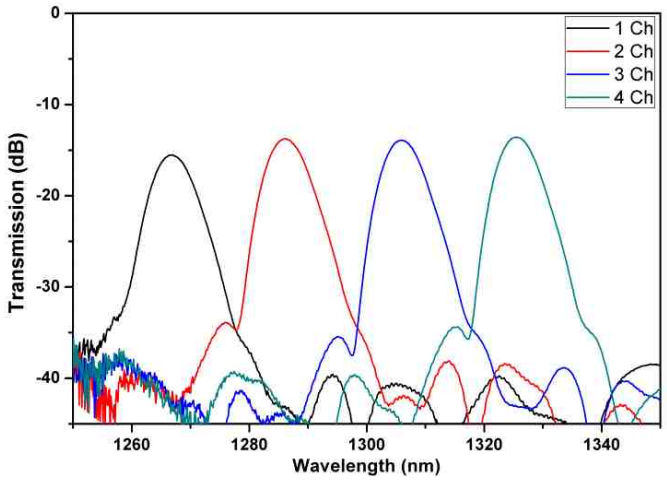

Fig. 6.17. The measured transmission spectrum of the fabricated 4-channel PCG.

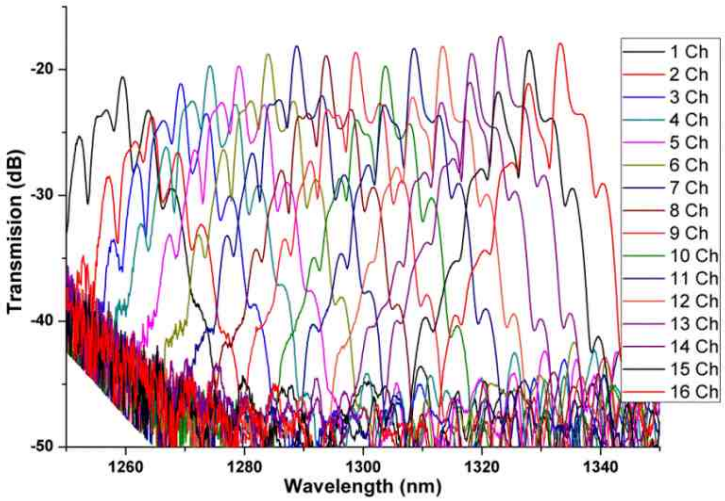

Fig. 6.18. The measured transmission spectrum of the fabricated 16-channel PCG.

The measured result of the 16-channel PCG is given in Fig. 6.18. The device shows on-chip loss of about -18 dB for the central wavelength. The high crosstalk between each channel mainly restricts its practical application. One reason is the TE-TM channel wavelength shift as we discussed earlier in section 6.1.3. It also may be caused by the poor quality of the large polymer slab waveguide fabricated by spin coating process. The thickness non-uniformity of the large slab area will affect the light path of each wavelength which will degrade the quality of interference pattern on the output channel.

Also the defects in the large slab area, due to the dusts in the fabrication process and micro cracks formed during the baking process, will largely scatter the light and increase the crosstalk of the device.

6.2 Planar Concave Grating with Flattened Spectral Response for Optical Interconnects

The conventional design of PCG offers a Gaussian-like spectral response with small shift tolerance on spectral channels as shown above, which seriously restricts its practical application in dense or coarse WDM systems [120]. A slight change in spectral channel wavelength could seriously affect the WDM device performance. Various techniques have been proposed to flatten the spectral response of the PCG. The most common method is to use a mode shaper such as MMI section to form a double-peak field distribution in the PCG planar input [121, 122]. The convolution of this imaged field profile and the output waveguide mode at the PCG planar output will produce a flattened spectral response. The schematic diagram of the MMI-PCG is given in Fig. 6.19.

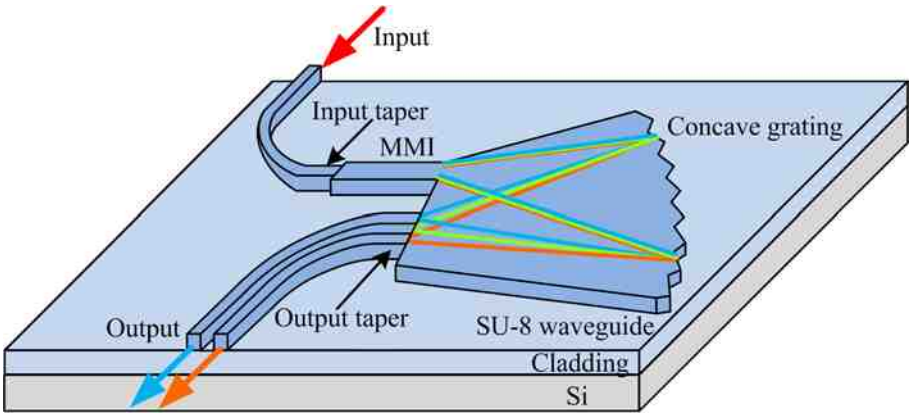

Fig. 6.19. The schematic diagram of the MMI-PCG.

In this section, we present a 4-channel PCG wavelength demultiplexer on SU-8 polymer waveguides with a flattened spectral response. The flattened spectral response is accomplished by using an optimized MMI as the PCG planar input for all spectrally separated channels. The mode field distribution at the PCG planar input is controlled by adjusting the waveguide taper width coupled to MMI. The devices are again realized by using SU-8 polymer strip waveguides fabricated by one-step UV lithography process, offering lower cost and wider spectral band selection flexibility. The PCG wavelength demultiplexer with the desired flatten spectral response has been demonstrated.

6.2.1 MMI Aperture for the Desired Input Field Profile

A MMI mode shaper located on the input port of PCG is used to form the desired field distribution in the input plane. It consists of a taper with width *w* and a multi-mode section with length *L* and width *W*, as shown in Fig. 6.20. The input taper of the MMI is located at the center of the MMI for a symmetric interference. According to the self-imaging principle of MMI, an input field profile is reproduced in single or multiple images along the propagation direction of the waveguide [123]. The location of the first *N* images of the input field distribution can be calculated from equation

$$z = \frac{3\pi}{4N(\beta_0 - \beta_1)} \tag{6.7}$$

where β_0 and β_1 are the propagation constant of the first two lowest modes of MMI. Any *N* images location can be chosen for the desired field output of the MMI aperture. The width *W* of the MMI can be utilized for changing the distance between the adjacent center positions of the *N* images. The width *w* of the input taper can be used for defining the field distribution of each image and changing the overlap of them. The parameters *w*,

W, and *L* of the MMI aperture can be adjusted to control the mode field distribution at the PCG planar input. The convolution of this imaged flat field and the output waveguide mode at the PCG planar output will produce a flattened spectral response. The width of the flat region in the spectral response depends on the width of the MMI field distribution at the PCG planar input.

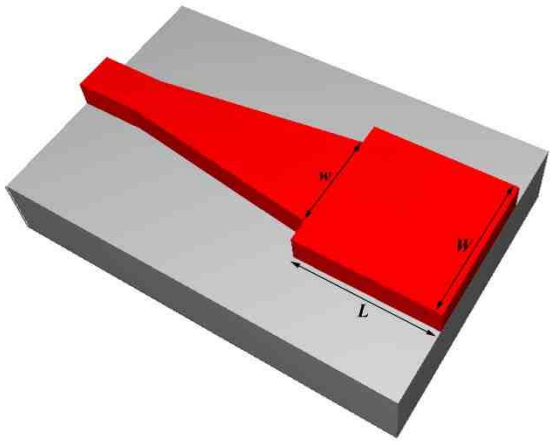

Fig. 6.20. Schematic image of a MMI aperture for a PCG.

The position of two images of the MMI aperture is chosen for the desired field output because of its better flat-top performance and larger tolerance compared with other *N* image positions. The field width of the MMI aperture should be comparable to the width of the PCG output aperture to create a sufficiently flat spectral response. A 10 μm wide *W* MMI aperture with a 5 μm wide field profile (close to the width of PCG output aperture) are the best compromise for achieving a low loss and flat spectral response. The decrement in width *W* will produce a lower loss but have a narrower spectral response. The increment in width *W* will have a wider spectral response but will significantly increase the loss [121]. The required length *L* of a 10 μm wide MMI aperture is

calculated to be 60.8 μm from Eq. (6.7). The width *w* of the 300 μm long input taper of MMI has been optimized as discussed below.

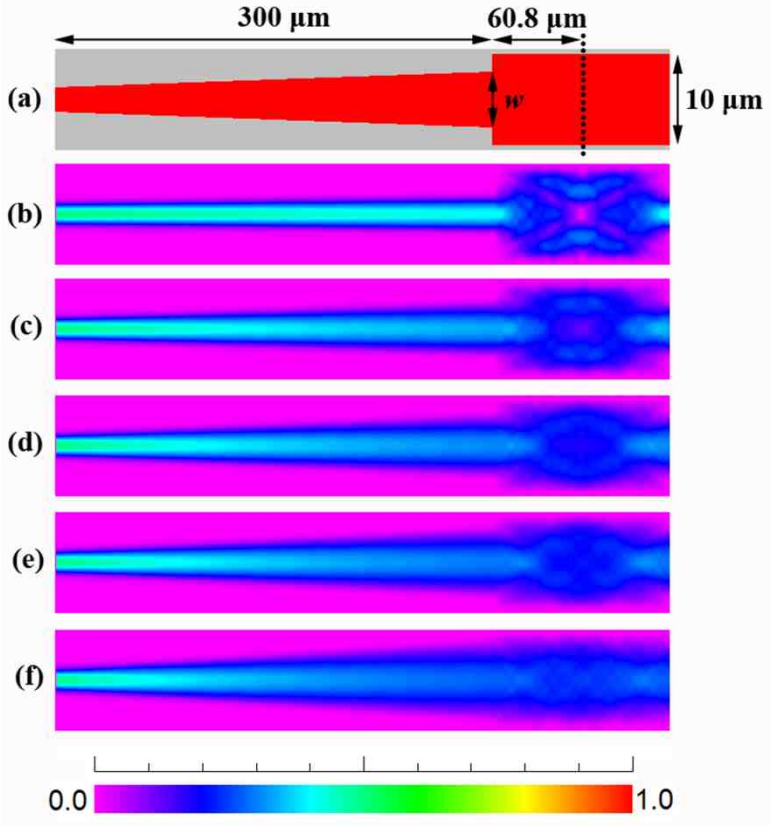

Fig. 6.21. (a) Schematic geometry of MMI aperture. (b)-(f) Simulated filed distribution of the 10 μm wide *W* MMI with input taper widths *w* of 4.0, 6.0, 7.0, 7.7, and 9.0 μm, respectively.

The simulated field propagations for the 10 μm wide and up-to 122 μm long MMIs with input taper widths *w* of 4.0, 6.0, 7.0, 7.7, and 9.0 μm are shown in Fig. 6.21. Two images of input field distribution is clearly reproduced at the L = 60.8 μm position (dotted line). The field distributions of the reproduced images are defined by the input taper width. A line scan of the field distribution at the two images position of these MMI apertures is shown in Fig. 6.22. The field distribution of these two images in combination changes from twofold image with a center dip to a Gaussian-like curve, by varying the

input taper width w from 4.0 μm to 9.0 μm. The spectral response can be realized from the convolution of the waveguide mode field profile at the PCG planar output (solid line) with the field distributions at the MMI aperture.

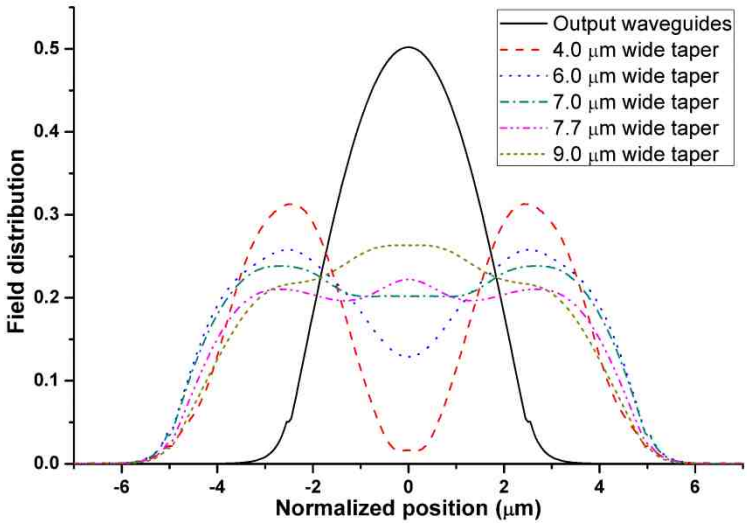

Fig. 6.22. Mode field distribution at the end of MMI for different input taper widths w.

6.2.2 MMI-PCG Design and Simulations

The MMI-PCG is designed around a central wavelength λ of 1310 nm. The diffraction order is chosen to be m = 10 in this study, which results in a free spectral range of about 130 nm. The total internal reflection facet is applied to the PCG grating. The incident and diffracted angles are chosen to be θ_i = 65° and θ_d = -25°. The calculated grating period is d = 17.4 μm from Eq. (6.1). The 5 μm wide tapered output waveguides are spaced 10 μm apart on the Rowland circle. The designed central wavelengths of the four output channels are 1280, 1300, 1320, and 1340 nm, with 20 nm spectral separations. The Rowland circle radius is then R = 613.6 μm. The length L and width W of the MMI are 60.8 μm and 10 μm, respectively. The design data are summarized in Table 6.2.

PCG Parameters	Device
Center wavelength (λ_c)	1310 nm
Wavelength spacing ($\delta\lambda$)	20 nm
Order of diffraction *m*	10
Free spectral range (*FSR*)	130 nm
Incident angle (θ_i)	65°
Diffracted angle (θ_d)	-25°
Grating period (*d*)	17.4 μm
Rowland circle radius (R)	613.6 μm
Number of output waveguides (*N*)	4
Space of output waveguides	10 μm
MMI length (*L*)	60.8 μm
MMI width (*W*)	10 μm

Table 6.2. The parameters of the designed MMI-PCG.

The MMI-PCG simulation is performed based on the scalar diffraction theory mentioned earlier. The field distribution at the end of the MMI is calculated by BeamPROP (Rsoft), which is used as the input field of the PCG. The incident waveguide field on the grating facets and the diffracted field on the Rowland circle are calculated according to the Kirchhoff-Huygens diffraction formula. The spectral response of each channel can be obtained by calculating the overlap integral between the waveguide taper field profile at the PCG planar output and the diffracted and focused field by the PCG. The grating facets are also chipped and blazed for better performance as we discussed before. Fig. 6.23(a) shows the simulated spectral response of the MMI-PCGs with

variation of input taper widths *w*. The optimized taper width is found to be 7.7 μm which has a quite flat spectral response. If the taper width is 4.0 or 6.0 μm smaller than the optimized taper width 7.7 μm, the device indicates a center dip spectral response. If the taper width is 9.0 μm wider than 7.7 μm, the device approaches a Gaussian like spectral response. The simulated transmission spectrum of MMI-PCG with 7.7 μm wide input taper is presented in Fig. 6.23 (b). The simulated device exhibits a central channel loss of -3.4 dB, a crosstalk of -36.6 dB, and an on-chip loss non-uniformity of 0.3 dB.

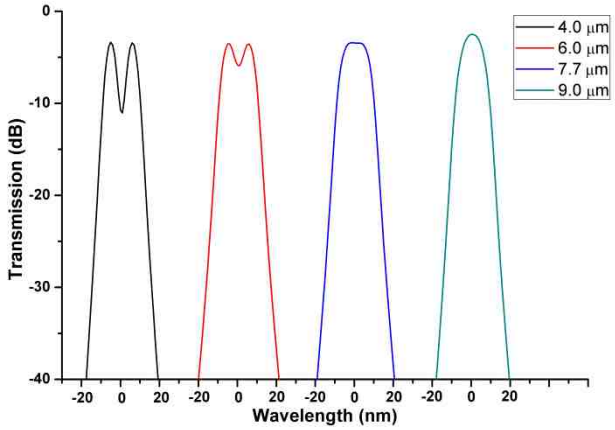

(a)

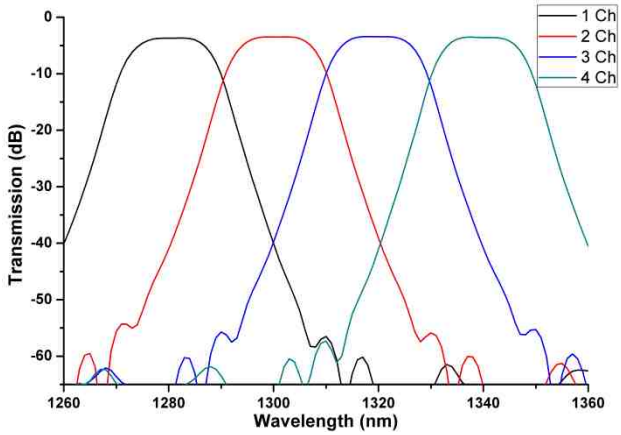

(b)

Fig. 6.23. Simulated transmission spectrum of (a) MMI-PCG with variation of input taper width *w* of (b) MMI-PCG with a 7.7 μm wide input taper.

6.2.3 MMI-PCG Fabrication and Testing

To verify the device design with a flattened spectral response, the MMI-PCG devices with different input taper widths *w* were fabricated on SU-8 polymer. The fabrication processes are the same as mentioned in section 6.1.4. Fig. 6.24(a) and (b) show the microscope images of the fabricated MMI-PCG and the magnified image of the grating. The microscope images of the fabricated MMI aperture with the input taper width *w* of (a) 4 μm, (b) 6 μm, (c) 7 μm, and (d) 8 μm are shown in Fig. 6.25.

A broadband superluminescent diode light source was used to characterize the fabricated MMI-PCG devices. The input light from the light source fiber was butt-coupled to the input waveguide through a TLF with a focus spot size of about 2.5 μm. Another TLF was used to collect the output light from the end of output optical waveguides, which was connected to an optical spectrum analyzer (Agilent 86142B).

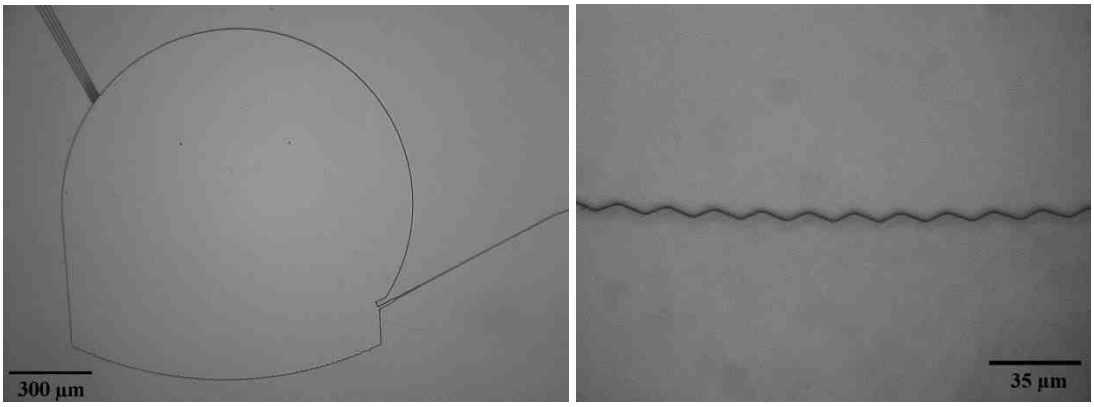

(a) (b)

Fig. 6.24. Microscope images of (a) the fabricated MMI-PCG and (b) magnified image of the grating.

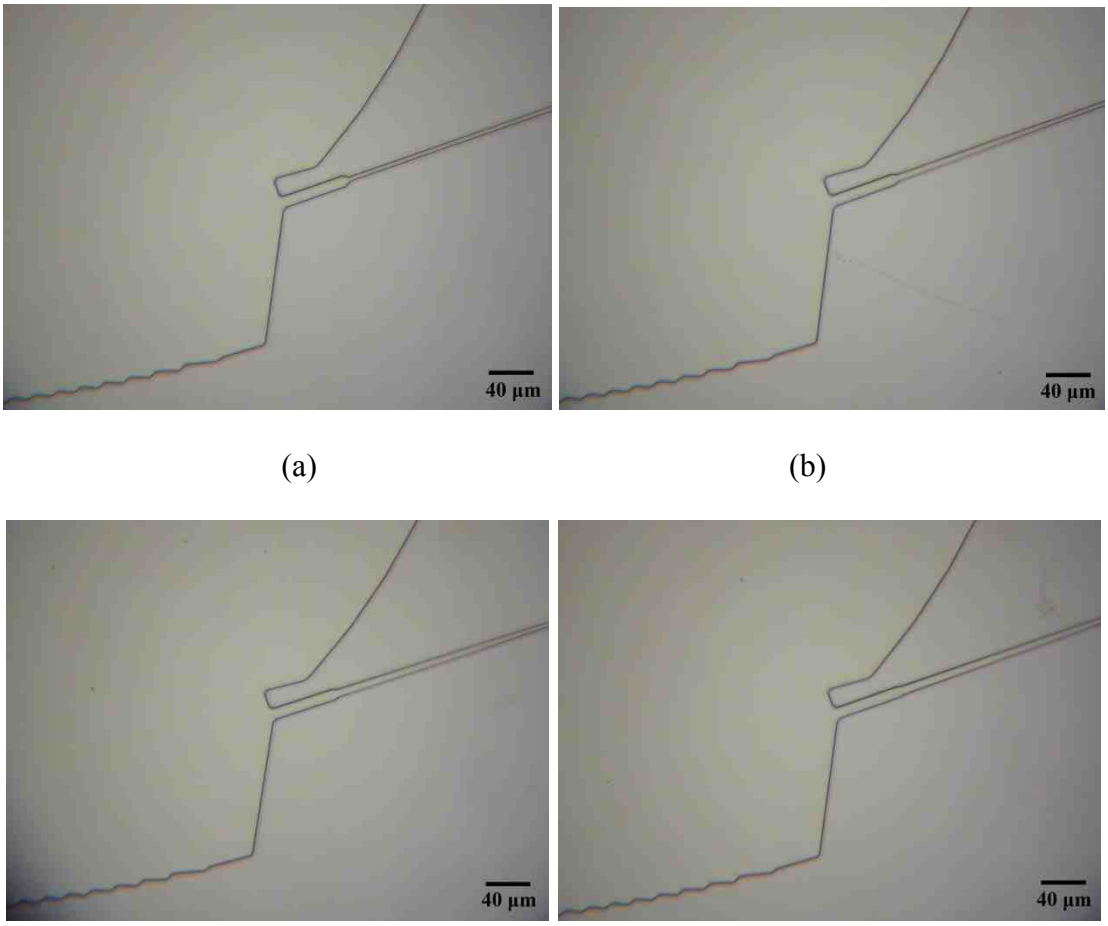

Fig. 6.25. Microscope images of the fabricated MMI aperture with input taper width *w* of (a) 4 µm, (b) 6 µm, (c) 7 µm, and (d) 8 µm.

The measured spectral response of the fabricated MMI-PCG devices with different input taper widths *w* is shown in Fig. 6. 26(a). The losses are normalized to a reference straight waveguide. The MMI-PCG devices with 4 µm and 6 µm wide input tapers show the center dip spectral response, while the one with 8 µm wide input taper shows near Gaussian shaped spectral response. The device with 7 µm wide input taper presents most flattened spectral response, which is slightly different from the simulation results of 7.7

μm, due most likely to a small mismatch between the fabricated MMI width and waveguide height and the values used in the design simulation.

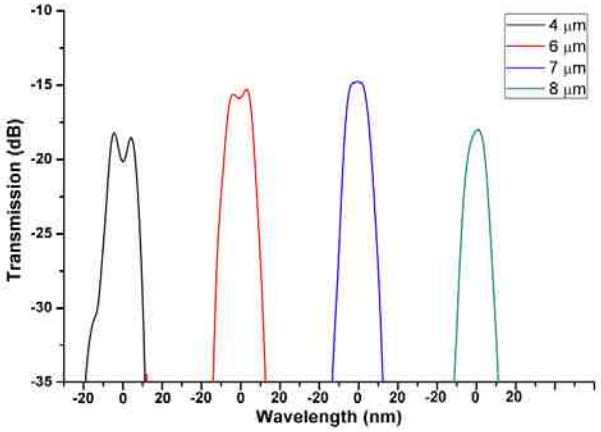

(a)

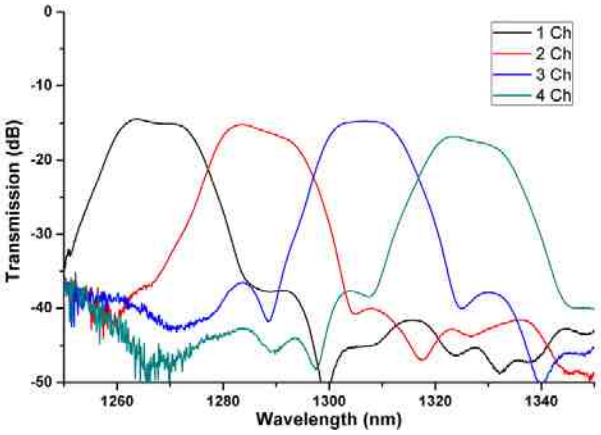

(b)

Fig. 6.26. Measured spectral response of (a) MMI-PCG with variation of input taper width *w* and (b) MMI-PCG with 7 μm wide input taper

Fig. 6.26(b) presents the measured transmission spectrum of the fabricated MMI-PCG device with 7 μm wide input taper. The on-chip loss for the central wavelength is about -14.8 dB. There is about -3 dB loss resulting from the flat top response. The remaining loss is mainly due to the grating facets imperfections such as the non-verticality, corner rounding, and sidewall roughness. The crosstalk of the fabricated device is -22 dB and

the on-chip loss non-uniformity is 2.5 dB. There is about 10 nm spectral shift in the transmission spectrum toward short wavelength comparing with the simulation results. This is believed to be caused by the thinner planar waveguide of the fabricated PCG and slightly smaller effective refractive index of the planar waveguide mode, as compared with the values used in simulation. Thus, we have successfully achieved a flattened spectral response by adjusting the input taper width *w* of the MMI aperture structure.

In summary, we have demonstrated 4-channel PCG wavelength demultiplexers with a flattened spectral response based on SU-8 polymer waveguides. The flattened spectral response to all spectrally separated channels is accomplished by using an optimized MMI as the input aperture to the PCG. The mode field distribution in the PCG planar input is controlled by adjusting the width *w* of the input taper connected to the MMI. The devices were realized on SU-8 polymer waveguides by one-step UV lithography. Experimental results show that the shape of the spectral response can be controlled by adjusting the taper width. The devices with a flattened spectral response can be widely used for dense or coarse WDM systems to support various optical interconnection and communication applications. The small PCG device footprint as compared to AWG is attractive for practical implementation.

6.3 Planar Concave Grating for Integrated Spectrometer

As discussed in Chapter 1, the OCT system is bulky and expensive which contains many bulk optical components such as beam splitters, reference arm optics, and optical spectrometers. The most bulky component is the optical spectrometer that often occupies

a large portion of the SD-OCT system (see Fig. 6.27). Using bulk optics based SD-OCT is not possible to yield book size system for portable clinical applications.

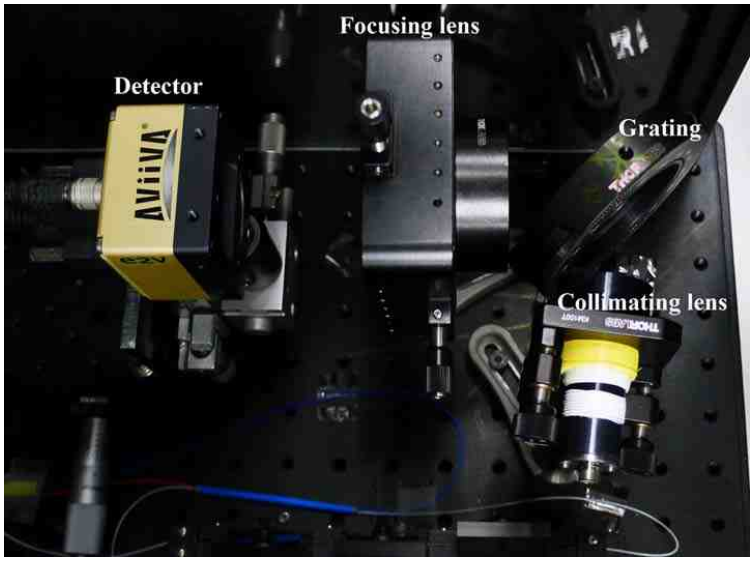

Fig. 6.27. Bulky optical spectrometer portion of SD-OCT system.

From the SD-OCT system configuration, besides the semiconductor SLD light source, the galvanometer scanner, and focusing lenses at the sample arm, many SD-OCT system components including the 2×2 coupler, reference arm, and optical spectrometer could be realized by using integrated optics. It is thus of our interest to explore the design of the integrated optics version of the optical spectrometer for the SD-OCT in this section.

6.3.1 SD-OCT Parameters

The parameters that determine the imaging quality in SD-OCT are center wavelength, lateral resolution, axial resolution, and maximum imaging range.

The axial resolution of an SD-OCT is mainly set by the effective bandwidth of the detected light, which depends on both the bandwidth of the light source and the bandwidth of the spectrometer [124]. If the detected spectrum has a Gaussian shape, the axial (depth) resolution is given by [34, 36, 125]

$$\delta z = \frac{2ln2}{\pi}\frac{\lambda_0^2}{\Delta\lambda} \tag{6.8}$$

where λ_0 is the center wavelength and $\Delta\lambda$ is the effective bandwidth of the detected spectrum. The typical OCT axial resolution is in the range of 2-20 μm depending on the center wavelength and bandwidth.

The lateral resolution of an SD-OCT is defined as the full width at half maximum of a focusing beam spot size on a sample and is given by [36]

$$\delta x = 0.37\frac{\lambda_0}{NA} \tag{6.9}$$

where *NA* is the numerical aperture of the objective lens. Increasing the numerical aperture *NA* can reduce the spot size and thereby increase the lateral OCT resolution. However, an increase in *NA* leads to a reduced depth of focus, which results in a reduced OCT imaging depth. An appropriate numerical aperture should be chosen depending on the application.

The maximum imaging range of an SD-OCT depends on the spectral sampling interval and is given by [126]

$$z_{max} = \frac{\lambda_0^2}{4\delta\lambda} \tag{6.10}$$

where $\delta\lambda$ is the wavelength spacing of the spectrometer.

6.3.2 PCG Spectrometer for SD-OCT

The effective bandwidth of the detected spectrum $\Delta\lambda$ for an SD-OCT system using a PCG is determined by both the spectral range of the light source and the *FSR* of the spectrometer. The spectral range of the light source that we used in the OCT measurement is about 100 nm for 1310 nm center wavelength. In this work, the *FSR* of the PCG spectrometer is designed to be large than the spectral range of the light source.

The *FSR* of a PCG is determined by the diffraction order *m* of the grating. Therefore, the diffraction order *m* should be smaller than 13, which results in free spectral range larger than 100 nm. As a result, the FWHM of the light source, which is about 80 nm in our SD-OCT system, mainly determines the axial resolution. The theoretical axial resolution is limited to be 9.47 μm according to Eq. (6.8). We aim at integrated SD-OCT systems with the maximum imaging range around 1 mm and 4 mm.

The PCG integrated spectrometers are designed based on SU-8 polymer waveguide. The optical waveguides for input and output of PCG have 2.5 μm width and 2 μm height. The PCG input and output channel waveguides have 300 μm long waveguide tapers that changes width from 5 μm apertures to 2.5 μm wide waveguide.

Parameters	**200-channel**	**1024-channel**
Center wavelength (λ_c)	1310 nm	1310 nm
Wavelength spacing ($\delta\lambda$)	0.5 nm	0.1
Diffraction order (*m*)	10	12
Free spectral range (*FSR*)	130 nm	109 nm
Incident angle (θ_i)	27.5°	42°
Diffracted angle (θ_d)	25°	38°
Grating period (*d*)	9.53 μm	7.87 μm
Rowland circle radius (*R*)	13.43mm	40 mm
Number of output waveguides (*N*)	200	1024
Space of output waveguides	10 μm	10 μm

Table 6.3. The design parameters of the PCG spectrometers.

Table 6.3 lists the design parameters of the 200-channel and 1024-channel PCGs for the spectrometers. The wavelength spacing is 0.5 nm and 0.1 nm resulting in maximum imaging range of 0.85 and 4.3 mm, respectively. The lower diffraction order results in shorter facets which can minimize the variation in transmission between channels. But it will cause lower fabrication tolerance such as grating round corner. The choice for incident and diffracted angles is a compromise between transmission spectrum performance and the size of the device. Placing the input waveguide and the output waveguide at a greater angle improves performance. But it will also increase the device size.

For the 200-channel PCG, the diffraction order is chosen to be $m = 10$ corresponding to a free spectral range of about 130 nm, which can cover the operational spectral range of the spectrometer. The incident and diffracted angles are chosen to be $\theta_i = 27.5°$ and $\theta_d = 25°$. The calculated grating period is $d = 9.53$ μm from Eq. (6.1). The chip size of the 200-channel PCG device is 3 cm × 3 cm. The main challenge for the 1024-channel PCG is the tremendous increase of the device size because of the quite small wavelength spacing. We use a larger diffraction order $m = 12$ and larger incident angle $\theta_i = 42°$ and diffracted angle $\theta_d = 38°$ for the 1024-channel PCG device, which results in the grating period $d = 7.87$ μm and an acceptable chip size of 8 cm × 8 cm.

The simulated transmission spectra of the 200-channel PCG for TE-polarized light are shown in Fig. 6.28. At the central channels, a crosstalk of -70 dB and a channel loss of -1.2 dB are calculated. At the outermost channels, these values are -60 dB and -4.42 dB, respectively.

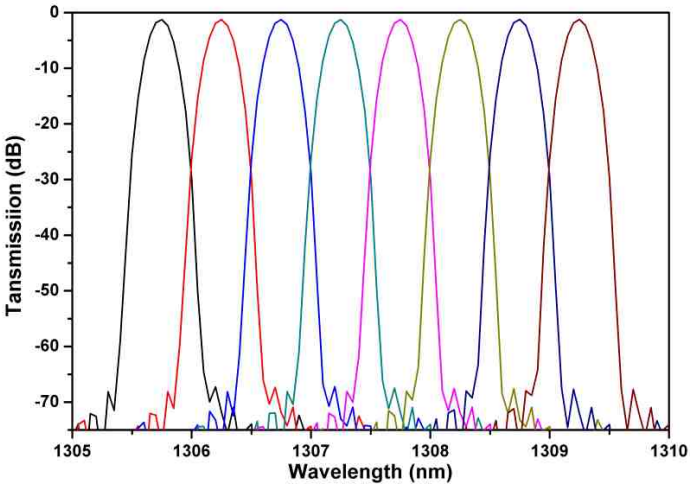

(a)

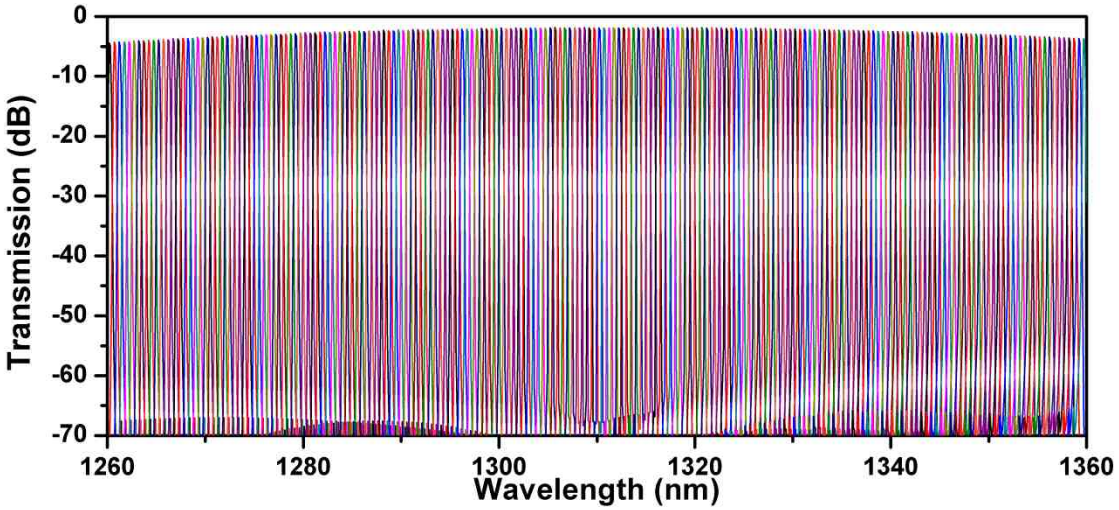

(b)

Fig. 6.28. Simulated transmission spectra for the 200-channel PCG (a) at central channels and (b) over the complete spectral range.

The simulated transmission spectra of the 1024-channel PCG for TE-polarized light are shown in Fig. 6.29. A crosstalk of -70 dB and -40 dB and a channel loss of -1.7 dB and -5.6 dB are calculated for central channels and outermost channels, respectively. The crosstalk and channel loss of the 1024-channel PCG is slightly higher than the 200-

channel PCG because of large incident and diffracted angles, as we discussed earlier, which is still good enough for the integrated spectrometer application.

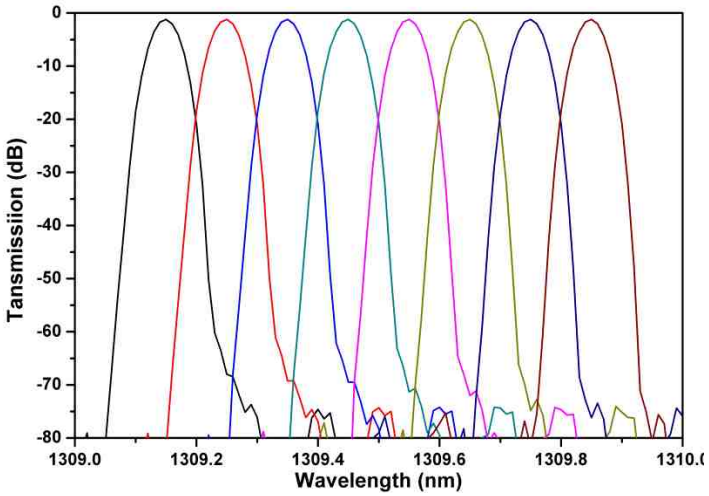

(a)

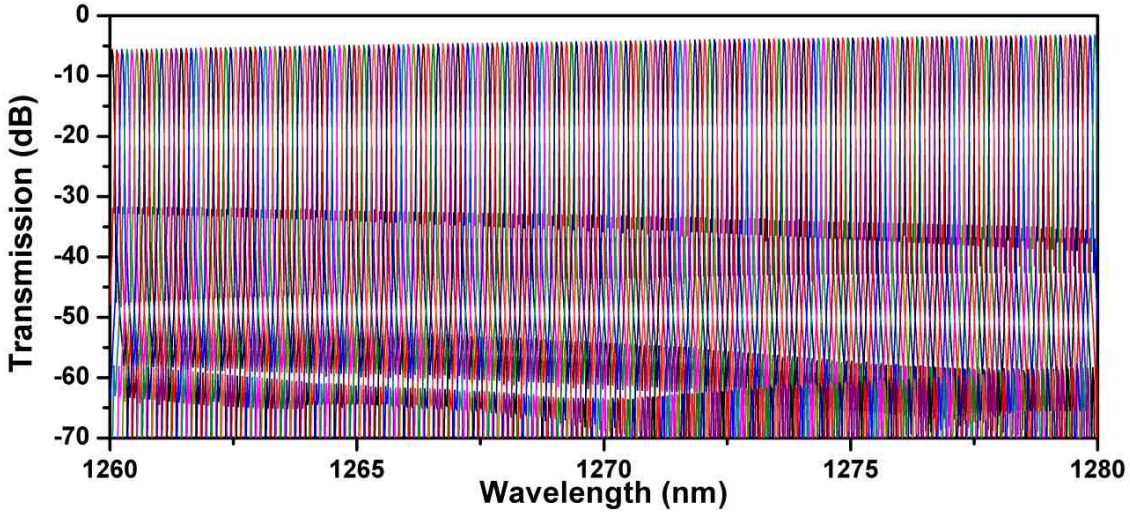

(b)

Fig. 6.29. Simulated transmission spectrum for the 1024-channel PCG (a) at central channels and (b) over the spectral range from 1260 nm to 1280 nm.

The simulation results show good performance of the 200-channel PCG spectrometer with 0.5 nm channel spacing and the 1024-channel PCG spectrometer with 0.1 nm channel spacing. The 200-channel and 1024-channel PCGs both have low crosstalk,

small channel loss, and good uniformity, with chip size of 3 cm × 3 cm and 8 cm × 8 cm, respectively. The maximum imaging ranges are 0.85 mm and 4.3 mm with 9.47 μm axial resolution in theory, respectively. The design of PCG spectrometers moves a significant step toward on-chip SD-OCT system.

The fabrication and testing processes of PCG spectrometers are the same as the processes we mentioned earlier in section 6.1. It is however hard to measure the transmission spectra of the fabricated PCG devices because of the large insertion loss and crosstalk of PCGs, due to the TE-TM channel wavelength shift, non-uniformity and defects of the large polymer slab waveguide, and non-vertical and rounding corner of the grating portion, as we analyzed earlier. The devices fabrication condition needs to be further optimized to improve the performance of the PCG spectrometer based on SU-8 polymer waveguide by UV lithography.

Another way to avoid the present high insertion loss and crosstalk is using other dielectric material such as silicon nitride for wavelength demultiplexer fabrication by reactive ion etching [126-128], which is outside our focus on polymer waveguides. We have shown that we can realize a compact spectrometer by using integrated optics which is an extended vision of the wavelength demultiplexer for SD-OCT.

6.3.3 Alternative Compact Spectrometer

We have designed the integrated optics spectrometer with 200 and 1024 channels. Our simulation does show that PCG based waveguide spectrometer concept is valid and realizable. To support near term OCT application, we present in this section an alternative solution to compact spectrometer.

We designed a compact spectrometer by using small optical elements, as shown in Fig. 6.30. The compact spectrometer consists of two cylindrical lenses, two cylindrical mirrors, a diffraction grating, and a linear CCD array detector. The light beam from a single-mode fiber is first collimated by a cylindrical collimating lens in the vertical axis and is then collimated by the cylindrical collimating mirror in the horizontal plane (paper plane) toward a diffraction grating. The diffraction grating disperses the incident beam into its component wavelengths. The spectrum dispersed from the diffraction grating is focused onto the detector plane by using a focusing cylindrical mirror (horizontal focusing) and a collection lens (vertical focusing).

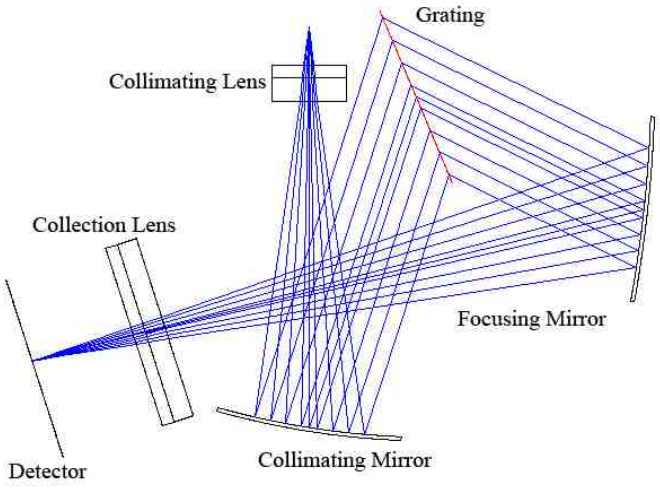

Fig. 6.30. Schematic of a compact spectrometer.

The angular dispersion is the amount of change of diffraction angle per unit change of the wavelength. The equation for the angular dispersion of the grating can be derived from the grating Eq. (6.1) by differentiation

$$\frac{d\theta_d}{d\lambda} = \frac{m}{d\cos\theta_d} \quad . \tag{6.11}$$

We usually choose m = 1 and achieve high dispersion by selecting a grating with a high groove frequency.

If we use a collimating cylindrical mirror with focal length *f* to focus the spectrum dispersed from the diffraction grating, the linear dispersion on the focusing plane is

$$\frac{dl}{d\lambda} = f\frac{d\theta_d}{d\lambda} = \frac{fm}{dcos\theta_d} \quad . \tag{6.12}$$

The spectral resolution of the grating is

$$\delta\lambda_{grating} = \frac{\lambda}{mN} = \frac{\lambda}{m\left(D/(cos\theta_d d)\right)} = \frac{\lambda cos\theta_d d}{mD} \tag{6.13}$$

where *N* is the groove number covered by the incident light beam and *D* is the size of the light beam in the horizontal direction collimated by the collimating mirror.

The spectral resolution decided by the pixel size *S* of the CCD camera can be derived from linear dispersion of grating

$$\delta\lambda_{CCD} = \frac{S}{dl/d\lambda} = \frac{Sdcos\theta_d}{fm} \quad . \tag{6.14}$$

The focus beam diameter *M* on the CCD camera plane by focusing mirror is

$$M = \frac{4\lambda f}{\pi D} \quad . \tag{6.15}$$

In order to achieve better performance and higher efficiency, the focused beam size *M* should be smaller than pixel size *S* and the spectral resolution of the grating $\delta\lambda_{grating}$ should be smaller than the spectral resolution $\delta\lambda_{CCD}$ decided by the pixel size of the CCD camera.

The spectrometer is designed for the broadband superluminescent diode light source with the center wavelength of 840 nm and bandwidth of 100 nm as an example. The input light is incident to the spectrometer system from a single-mode fiber with *NA* = 0.14. We used a 9.7 mm effective focal length (EFL) collimating cylindrical lens, a 62.5 mm EFL collimating cylindrical mirror, an 1800 l/mm transmission grating, a 100 mm EFL focusing cylindrical mirror, and a 20 mm EFL detector collection lens for the

spectrometer design. The incidence angle of the transmission grating is set to be 49.1° for the spectrometer design. The diffraction angle calculated from the grating equation is 49.1° for center wavelength. The linear array detector has 1 × 2048 pixels with 14 μm by 28 μm pixel size.

The spectral resolution of the grating is

$$\delta\lambda_{grating} = \frac{\lambda cos\theta_d d}{mD} = \frac{840 \times cos49.1 \times (1/1800)}{2 \times 0.14 \times 62.5} nm = 0.0175\ nm \tag{6.16}$$

The spectral resolution decided by the pixel size of CCD camera is

$$\delta\lambda_{CCD} = \frac{Sdcos\theta_d}{fm} = \frac{14000 \times (1/1800) \times cos49.1}{100} nm = 0.05\ nm \tag{6.17}$$

Therefore, the spectral resolution of the spectrometer system is 0.05 nm, decided by the pixel size of the CCD camera. The focus beam size $M = 6.11\ \mu m$, which is smaller than the pixel size. The axial resolution of the SD-OCT is thus $\delta z = 6.9\ \mu m$. The maximum imaging range of the SD-OCT is $z_{max} = 3.53\ mm$.

The optical design and ZEMAX ray tracing of the compact spectrometer are illustrated in Fig. 6.31. The use of collimating and focusing cylindrical mirrors can eliminate the chromatic aberration on the horizontal direction. The spherical and coma aberrations can be largely offset by tilting two mirrors to the opposite directions. The collimating cylindrical mirror is tilted 9° and the focusing cylindrical mirror is tilted -20° in our ZEMAX design.

The field curvature is caused by the different incident angle of the different wavelength diffracted from the grating to the focusing mirror. The focused beam size of the center wavelength on the detector can be optimized to be relatively small. However it is still quite large for the shortest wavelength (790 nm) and largest wavelength (890 nm) because of the focus field curvature. We slightly tilted the detector and its collection lens

with 4° to improve the quality of the focus beam for edge wavelengths. The eleven wavelengths with 10 nm wavelength spacing from 790 nm to 890 nm were defined in ZEMAX for performance analysis of the spectrometer. The detector view of focused dispersion beam is shown in Fig. 6.31(b).

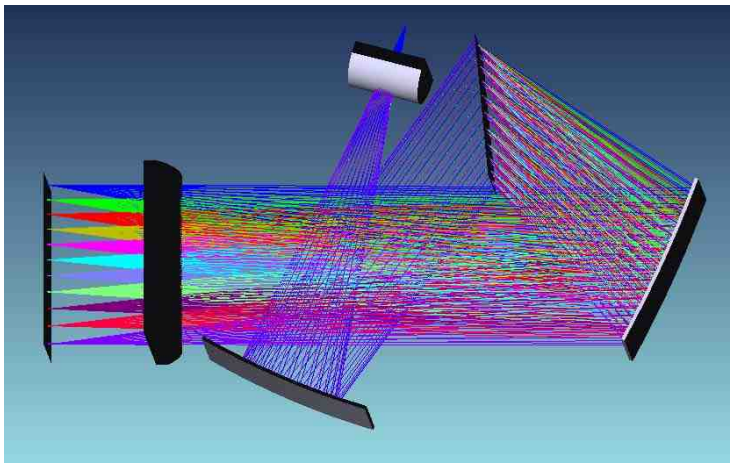

(a)

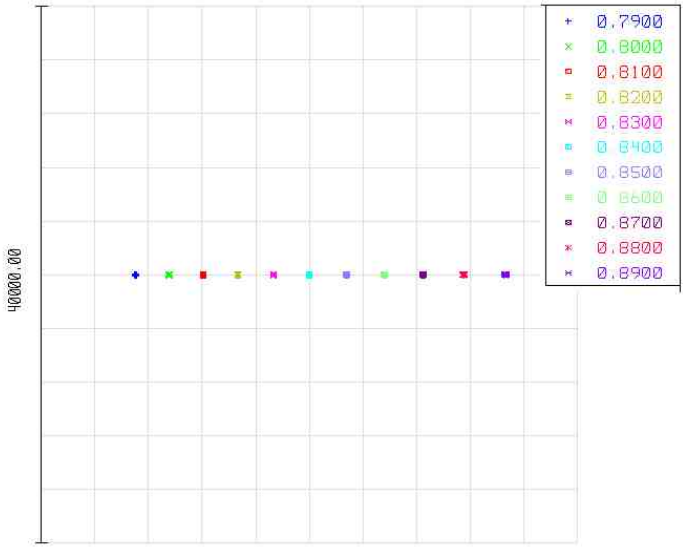

(b)

Fig. 6.31. The optical design and ZEMAX ray tracing of the compact spectrometer.

The irradiance on the detector is analyzed by using Physical Optics Propagation algorithm. The mode field diameter of the input single-mode fiber is 5 μm with 8°

divergent angle. Fig. 6.33 shows the total irradiance and X-cross (linear pixel direction) irradiance of the detector at center wavelength of 840 nm before tilting the detector and its collection lens. The full width at half maximum (FWHM) of X-cross irradiance is 10 μm on the detector. The FWHM of X-cross irradiance are about 47 μm and 100 μm at wavelength 790 nm and 890 nm, respectively, as shown in Fig. 6.34.

The FWHM of X-cross irradiance at center wavelength of 840 nm is almost the same after tilting the detector and its collection lens with 4°, while the FWHM at edge wavelengths will be much smaller. The FWHM at center wavelength (840 nm) is 11 μm, as shown in Fig. 6.34. The FWHM at wavelength 790 nm and 890 nm are about 35 μm and 32 μm, respectively, as shown in Fig. 6.35.

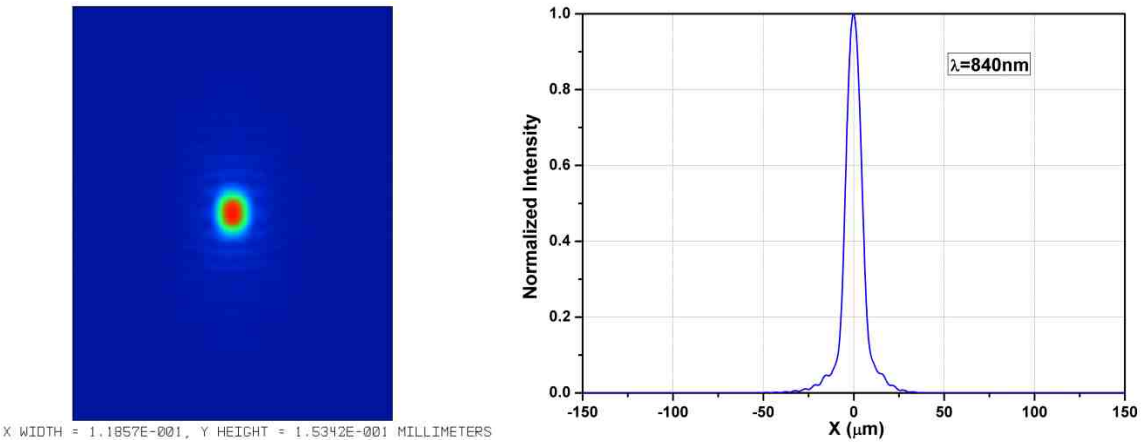

(a) (b)

Fig. 6.32. (a) Total irradiance and (b) X-cross irradiance of the detector at 840 nm wavelength before tilting the detector and its collection lens.

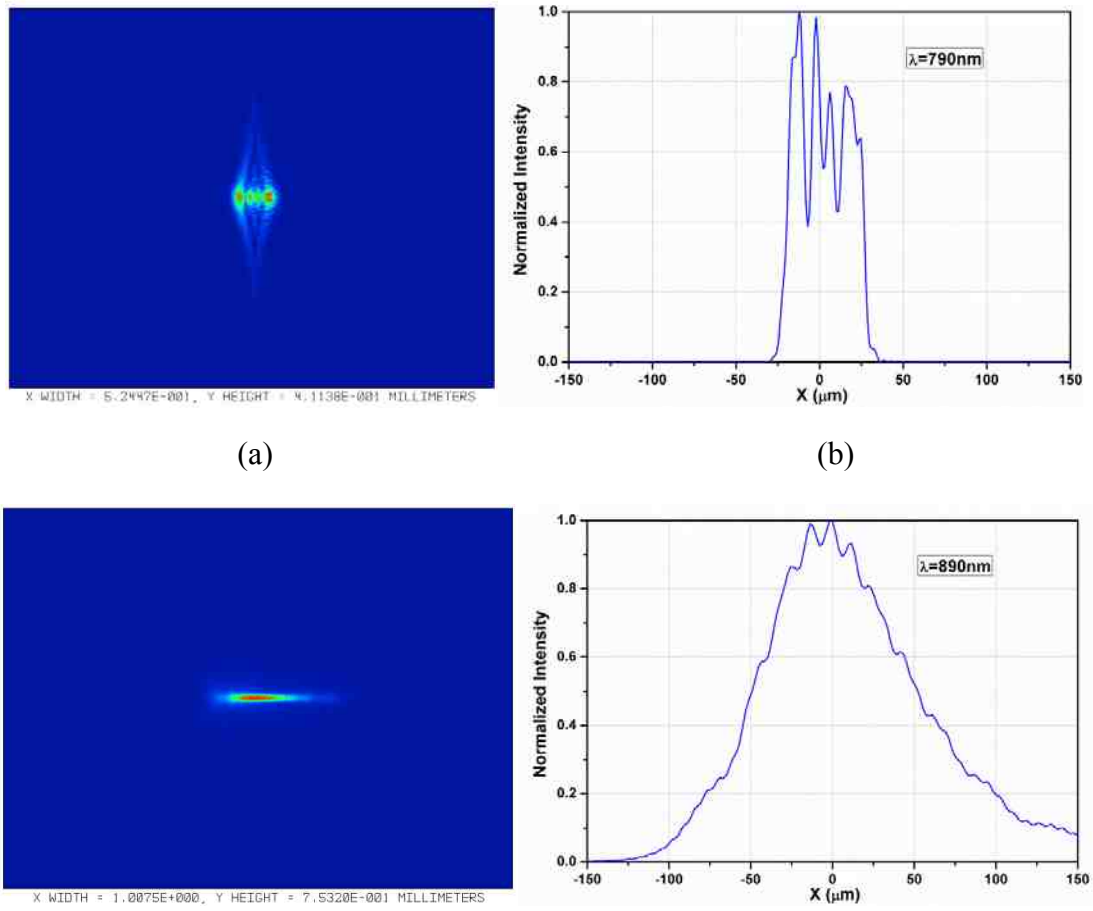

Fig. 6.33. (a) Total irradiance and (b) X-cross irradiance at 790 nm wavelength; (c) Total irradiance and (d) X-cross irradiance at 890 nm wavelength.

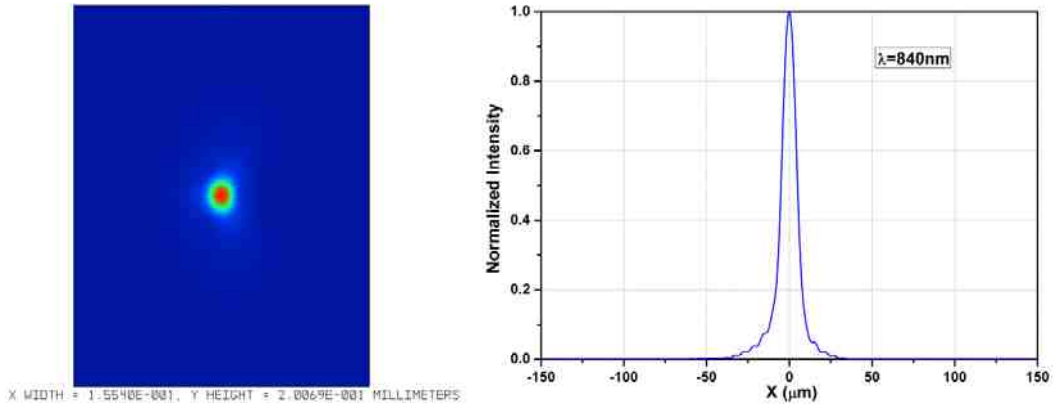

Fig. 6.34. (a) Total irradiance and (b) X-cross irradiance of the detector at 840 nm wavelength after tilting the detector and its collection lens with 4°.

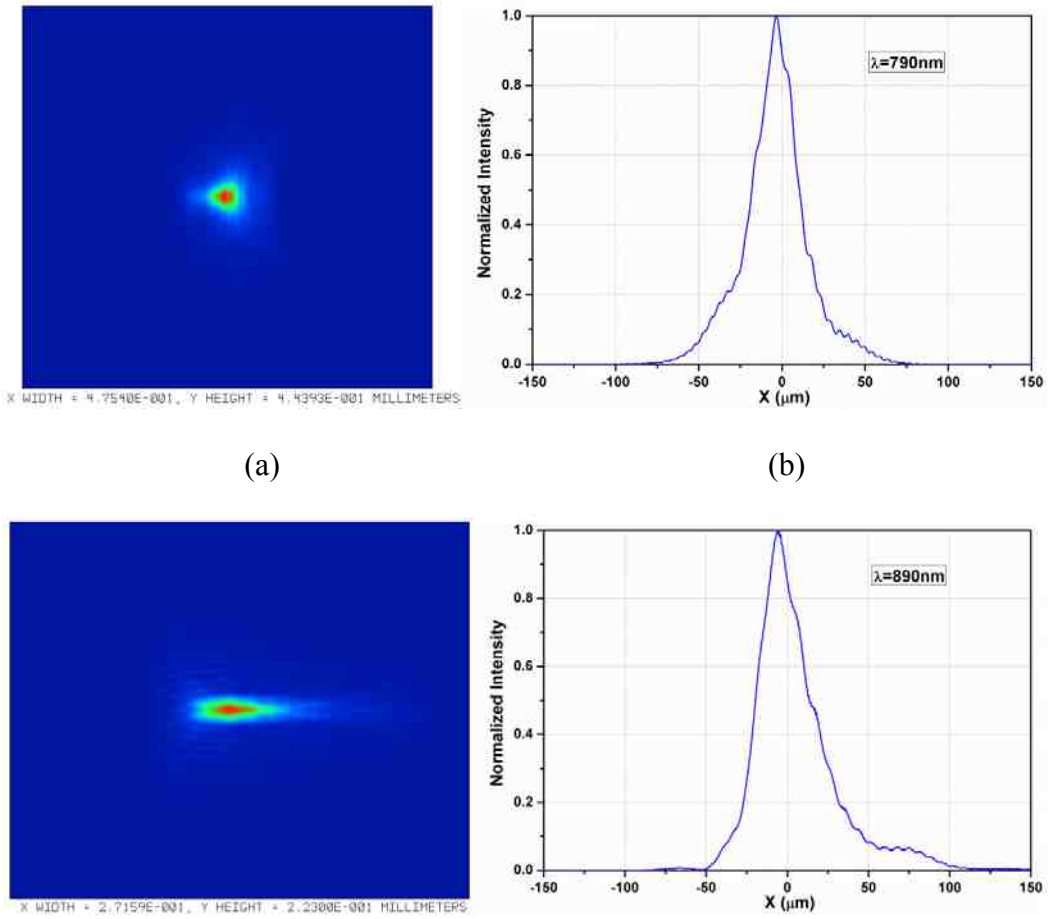

(a) (b)

(c) (d)

Fig. 6.35. (a) Total irradiance and (b) X-cross irradiance at 790 nm wavelength; (c) Total irradiance and (d) X-cross irradiance at 890 nm wavelength.

The experimental setup of the compact spectrometer system is presented in Fig. 6.36. Two cylindrical lenses were realized by plano-convex cylindrical lens with f = 9.7 mm and f = 20 mm. Two cylindrical mirrors were achieved by silver coating on plano-concave cylindrical lens with f = 250 mm and f = 400 mm. The EFL of the collimating and foucsing mirrors were 62.5 mm and 100 mm, respectively. We used a transmission grating with 1800 l/mm and 49.1° incidence angle which is optimized for 840 nm center wavelength with high diffraction efficiency and low wavefront distortion. The

wavelength at each detected pixel is known after calibrating the system with a reference source, as shown in Fig. 6.37.

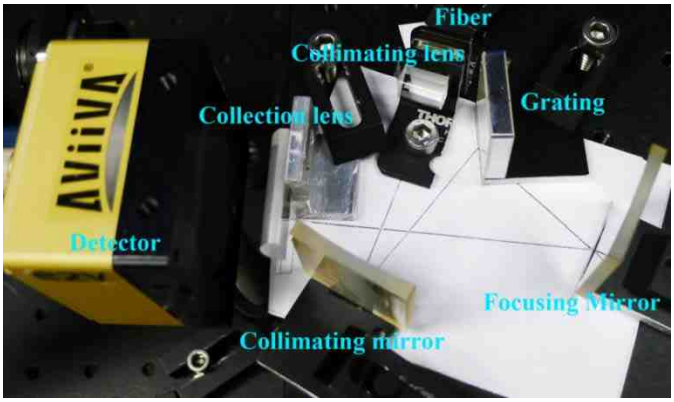

Fig. 6.36. Experimental setup of the compact spectrometer system.

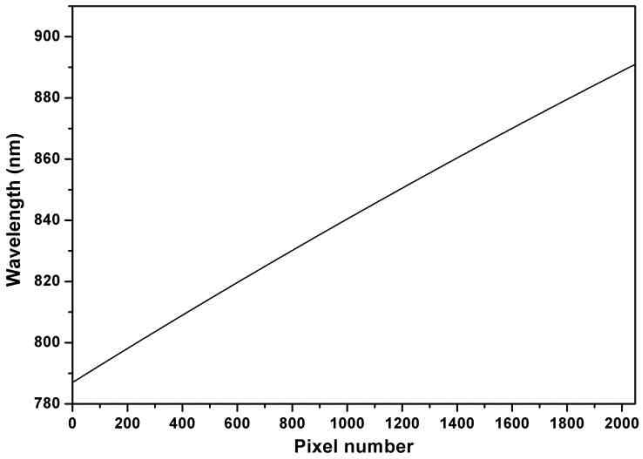

Fig. 6.37. Dispersion plot of spectrometer.

In order to determine the image performance of the compact spectrometer, it was incorporated into an SD-OCT system. Fig. 6.38 (a) shows an output spectrum with an optical path difference of 0.09 mm when a mirror is placed in the sample arm of the SD-OCT system. The interference spectrum is achieved after background and DC component subtraction. The point spread function of OCT demonstrated an axial resolution of 9.94 μm in air, as shown in Fig. 6.38 (b).

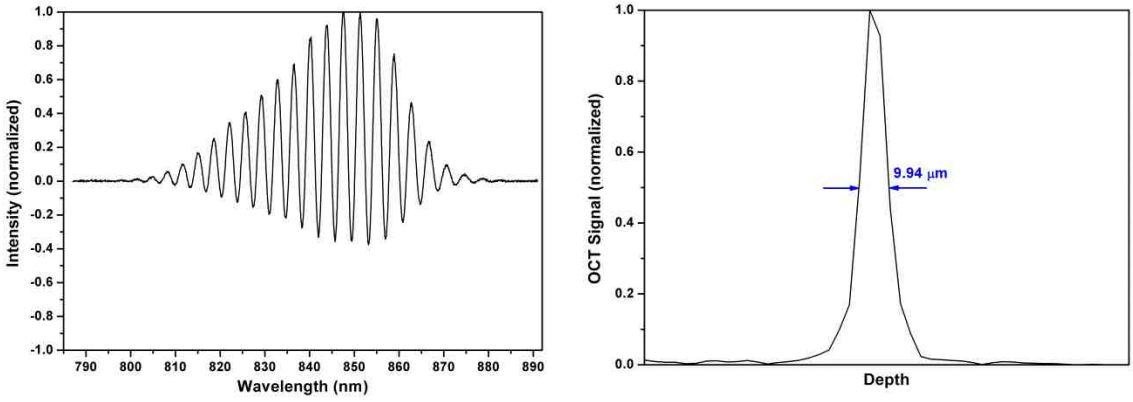

(a) (b)

Fig. 6.38. (a) Sample interferogram measured by compact spectrometer in the SD-OCT system with a mirror in the sample arm and (b) the reconstructed data showing the axial resolution.

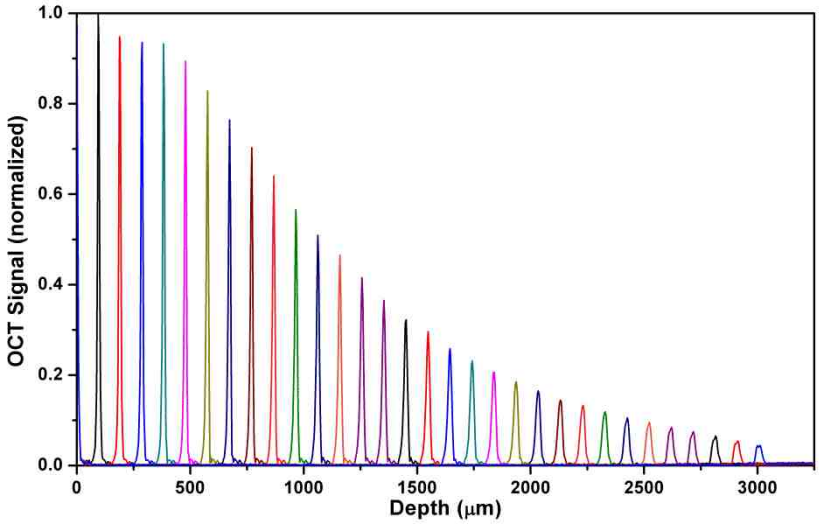

Fig. 6.39. OCT signal roll-off versus sample depth.

The roll-off curve for the system is presented in Fig. 6.39 when a mirror is placed in the sample arm at various imaging depth. The axial resolution does not degrade too much with distance. We achieved imaging range up to 3.0 mm. The OCT images of an orange sample, an onion sample, and a fingerprint were obtained by using SD-OCT system in combination with the compact spectrometer, as shown in Fig. 6.40.

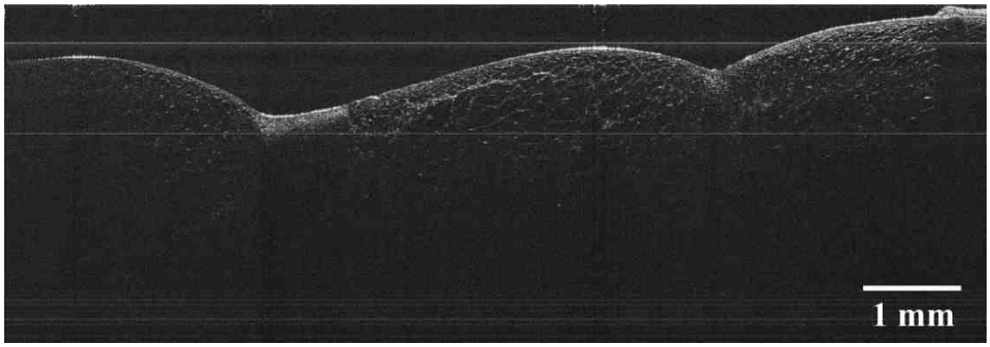

(a)

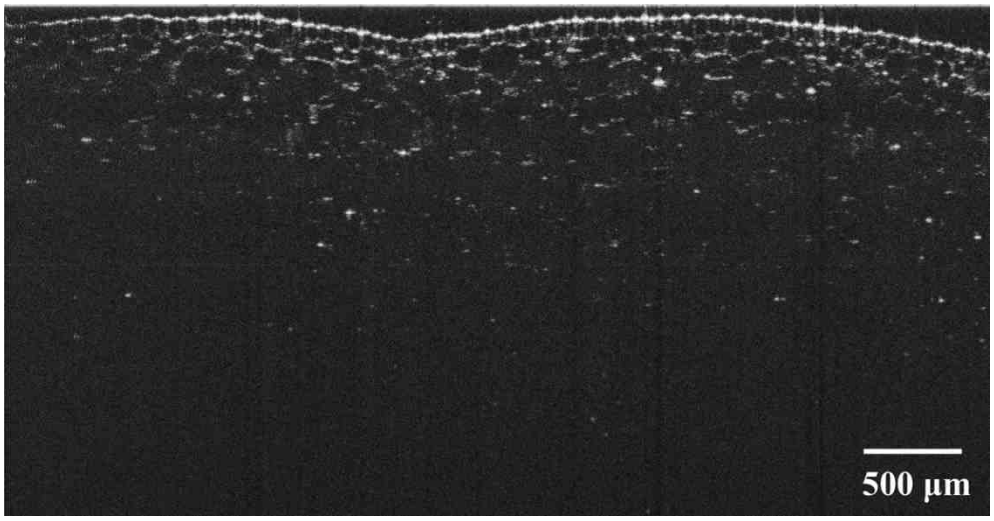

(b)

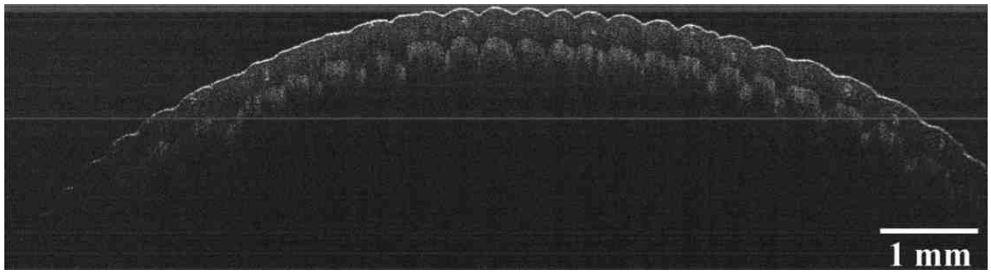

(c)

Fig. 6.40. OCT images of the (a) orange sample, (b) onion sample, and (c) fingerprint.

The compact spectrometer system has been used in our SD-OCT system and it has demonstrated the desired spectrometer performance. This design using cylindrical optics achieved a vertical beam size of about 3 mm in the diffraction plane which is only

slightly thicker than the designed on-chip spectrometer thickness of about 1 mm. The cylindrical lenses and grating can all be cut down to 3 mm to yield the compact spectrometer. The free space beam propagation in this configuration avoids the waveguide defect scattering in the planar region which is found to be detrimental to the spectrometer performance. This alternative solution to on-chip spectrometer is found effective.

6.4 Summary

In the chapter, we have presented our design and fabrication of planar concave grating for wavelength demultiplexer. The 4-channel PCG wavelength demultiplexers with a flattened spectral response for WDM have been demonstrated based on SU-8 polymer waveguides. The flattened spectral response to spectrally separated channels is accomplished by using an optimized MMI as the input aperture to the PCG. The mode field distribution at the PCG planar input is controlled by adjusting the width of input taper connected to MMI. The devices were realized by using SU-8 polymer strip waveguides fabricated by one-step UV lithography. Experimental results showed that the shape of the spectral response can be controlled by adjusting the taper width. The devices with a flattened spectral response can be widely used for dense or coarse WDM systems to support various optical interconnection and communication applications.

The PCG wavelength demultiplexer can also be used for the realization of on-chip optical spectrometer to support applications in optical coherence tomography. We have designed a 200-channel PCG spectrometer with 0.5 nm channel spacing and a 1024-channel PCG spectrometer with 0.1 nm channel spacing for SD-OCT application. The

simulated results showed that both have low crosstalk, small channel loss, and good uniformity, with chip size of 3 cm × 3 cm and 8 cm × 8 cm, respectively. The theoretical maximum imaging ranges set by the spectrometer design are 0.85 mm and 4.3 mm, respectively, with 9.47 μm axial resolution. The design of PCG spectrometers is an important step toward on-chip SD-OCT system.

To overcome the large insertion loss and crosstalk of the present fabricated on-chip PCG, an alternative solution is also demonstrated to design a compact optical spectrometer to support portable SD-OCT. This design using cylindrical optics has achieved a vertical beam size of about 3 mm in the diffraction plane which is only slightly thicker than the on-chip spectrometer thickness of about 1 mm. All the optical components can be cut down to 3 mm to yield the compact spectrometer. The compact spectrometer system has been used in our SD-OCT system and it has demonstrated the desired spectrometer performance. This alternative solution to on-chip spectrometer is found effective.

Chapter 7

Conclusion

In this dissertation, we have presented our innovative design and fabrication of optical polymer waveguide devices for optical interconnects and integrated optical coherence tomography. A dynamic card-to-backplane optical interconnects system is accomplished by using tunable optofluidic couplers. The PCG with optimized MMI input aperture is utilized to achieve a flattened spectral response for dense or coarse WDM systems that can benefit optical interconnects with multi-wavelength signal beams. The PCG wavelength demultiplexer is also designed to extend its channel number and density for on-chip optical spectrometer that could support the implementation of portable OCT system.

To begin, a cost-effective approach for polymer waveguides fabrication has been formulated. The VAM as a lower cost, rapid prototyping and high-resolution patterning technique is found suitable for polymer waveguide fabrication. It has been utilized to improve the performance of planar lightwave circuits by eliminating the residue planar layer. It can fabricate complex waveguide devices incorporating different materials in the same planar layer. SEM analysis depicts improved waveguide structures with high quality and multi-section. Low-cost polymer materials exhibiting high transparency, refractive index tunability, UV curability, and low viscosity have also been developed in accordance with the VAM fabrication method.

Consequently, a prism-assisted inclined UV lithography technique has been introduced to fabricate master pattern of waveguide structures with 45° slanted surfaces for the

VAM fabrication. It also benefits the fabrication of slanted structures with exposure angles ranging from 0° to 60° in SU-8 photoresist without immersion in the index matching liquid. The fabrication process of multidirectional slanted structures has been simplified to one-step UV exposure using a prism with multidirectional side surfaces such as a corner prism and a cone prism.

The flexible polymer waveguide with 45° integrated mirrors has been designed and fabricated by the VAM soft lithography technique for optical interconnects. Different light coupling efficiency has been realized by varying the inclined surface mirror depth. The fabricated polymer waveguides with 45° mirrors has demonstrated a propagation loss of -0.24 dB/cm, and a coupling efficiency of 75% and 38% for full and half mirrors, respectively. Such passive optical interconnection is useful for optical interconnect link with fixed point-to-point topology and shared bus topology.

The more energy efficient method has been demonstrated by using tunable optofluidic couplers to facilitate ON/OFF control of the interconnect link. The operation of the tunable optofluidic coupler has been accomplished by controlling the position of air bubbles and index matching liquid in the perpendicular microfluidic channel for refractive index modulation. The ON/OFF operations of the backplane optofluidic couplers save the optical signal power for card-to-backplane optical interconnection. High-speed dynamic card-to-backplane optical interconnects has also been demonstrated with 10 Gbps per channel.

To facilitate optical interconnection with external fiber networks that may include multi-wavelength signals, planar concave grating wavelength demultiplexer has been designed and fabricated using SU-8 polymer waveguides. The PCG devices simulation

has been performed based on the scalar diffraction theory. Factors such as TE-TM birefringence, waveguide thickness, and rounding radius of grating teeth have been considered for their effects on the PCG device performance. The 4-channel and 16-channel PCGs with conventional design have been demonstrated. The measured mode profiles and 3D intensity distribution of 2.5 μm and 5 μm wide straight reference waveguides indicate single-mode and multi-mode propagation, respectively, agreeing well with the calculated single-mode condition. The measured transmission spectrum of the fabricated PCG devices shows a Gaussian-like spectral response. The reasons for center wavelength shift, on-chip loss, and crosstalk have also been discussed.

The PCG wavelength demultiplexers with a flattened spectral response have also been designed and fabricated to demonstrate a large spectral shift tolerance on spectral channel that may benefit dense or coarse WDM systems. The flattened spectral response to spectrally separated channels has been accomplished by using an optimized MMI as the input aperture to the PCG. The mode field distribution in the PCG planar input is controlled by adjusting the width of the input taper connected to MMI. Experimental results show that the shape of the spectral response can be controlled by adjusting the taper width. The devices with a flattened spectral response can support various optical interconnection and communication applications.

The PCG wavelength demultiplexer can also be used for the realization of on-chip spectrometer by increasing channel number and channel density to support applications in optical coherence tomography. A 200-channel PCG spectrometer with 0.5 nm channel spacing and a 1024-channel PCG spectrometer with 0.1 nm channel spacing have been designed for the SD-OCT application. The simulated results show that both devices have

low crosstalk, small channel loss, and good uniformity, with chip size of 3 cm × 3 cm and 8 cm × 8 cm, respectively. The theoretical maximum imaging ranges set by the spectrometer design are 0.85 mm and 4.3 mm, respectively, with 9.47 μm axial resolution. The design of PCG spectrometers is an important step toward portable on-chip SD-OCT system. An alternative spectrometer solution has also been demonstrated using cylindrical optics to achieve a beam size of about 3 mm perpendicular to the diffraction plane which is only slightly thicker than the on-chip spectrometer thickness of about 1 mm. All the optical components can be cut down to 3 mm to yield the compact spectrometer. The compact spectrometer system has been used in our SD-OCT system to verify its desired spectrometer performance. This alternative solution to on-chip spectrometer is found effective.

7.1 Recommendations for Future Work

While the polymer waveguides with integrated mirrors have demonstrated effective application in dynamic card-to-backplane optical interconnects, there are challenging issues that need to be addressed. Although we have achieved the relatively high coupling efficiency of waveguide integrated mirrors (75% for full mirrors and 38% for half mirrors), the coupling loss between the card and the backplane could still be high due to the beam divergence after the mirror coupler. We could insert a mirco-lens in the optical path to reduce the divergence angle of the out-coupled beam [41] and to decrease the coupling loss.

The VAM soft lithography technique has been used to successfully produce the polymer waveguides with integrated mirrors and optofluidic couplers. The single-mode

polymer waveguide has also been fabricated by VAM technique by introducing the sectional flow tapers. More importantly, we are looking into accomplishing complex devices incorporating different materials in different portion of the waveguide on the same waveguide substrate by using different microfluidic channels. It is thus possible to fabricate polymer waveguides of passive, light sensitive, electro-optic, and light emitting on the common substrate to demonstrate monolithically integrated functional system. The exploration of multi-functional devices integration by VAM would be an important research direction.

The prism-assisted inclined UV lithography technique has been introduced to successfully produce 3D microstructures. It has been utilized to fabricate master pattern of waveguide structures with 45° slanted surfaces. The fabrication process of multidirectional slanted structures such as 3D mesh and horn structures has been simplified by using this method. More useful 3D structures with unique functional features could be fabricated.

The tunable optofluidic couplers for dynamic card-to-backplane system have been realized by refractive index modulation through a positional realignment of air bubbles and index matching liquid in contact with waveguide mirrors. The position of the air bubbles have been controlled by suction applied to one end of the microfluidic channel for all interconnect channels. The independent control of each waveguide could be realized by generating the bubble array using T-junction or flow-focusing methods.

The PCG wavelength demultiplexers with a flattened spectral response have been successfully demonstrated based on SU-8 polymer waveguide for a large spectral shift tolerance in dense or coarse WDM systems. Experiment results show that the shape of

the spectral response can be controlled by adjusting the width of the input taper connected to MMI. Polarization insensitive PCG device could be designed by balancing the material and waveguide birefringence or using a compensator section in the free propagation region.

The polymer waveguide based PCG spectrometers have been designed for compact and portable SD-OCT application with low crosstalk, small channel loss, and good uniformity. The theoretical maximum imaging ranges set by the spectrometer design are 0.85 mm and 4.3 mm, respectively, with 9.47 μm axial resolution. It is however hard to measure the transmission spectra of the fabricated PCG devices because of large insertion loss and crosstalk of PCGs, due to the TE-TM channel wavelength shift, non-uniformity and defects of the large polymer slab waveguide, and non-vertical and rounding corner of the grating portion. The devices fabrication condition needs to be further optimized to improve the performance of the PCG spectrometer based on SU-8 polymer waveguide by UV lithography. It is possible to realize the PCG spectrometer devices using dielectric material such as silicon nitride with significantly reduced waveguide defect scattering.

References

[1] S. E. Miller, "Integrated optics: An introduction," *Bell System Technical Journal,* vol. 48, pp. 2059-2069, 1969.

[2] R. G. Hunsperger, *Integrated optics: theory and technology*. New York: Springer, 1984.

[3] C. Monat, P. Domachuk, and B. Eggleton, "Integrated optofluidics: A new river of light," *Nature Photonics,* vol. 1, pp. 106-114, 2007.

[4] Y. Fainman, L. P. Lee, D. Psaltis, and C. Yang, *Optofluidics: fundamentals, devices, and applications*. New York: McGraw-Hill, 2010.

[5] M.-C. Estevez, M. Alvarez, and L. M. Lechuga, "Integrated optical devices for lab‐on‐a‐chip biosensing applications," *Laser & Photonics Reviews,* vol. 6, pp. 463-487, 2012.

[6] A. S. Flores, "Array Waveguide Evanescent Coupler for Card-to-Backplane Optical Interconnections," Ph.D. Dissertation, University of Miami, 2009.

[7] R. T. Chen and C. Choi, "Optical Interconnects," *Synthesis Lectures on Solid State Materials and Devices,* vol. 2, pp. 1-104, 2007.

[8] M. Horowitz, C.-K. K. Yang, and S. Sidiropoulos, "High-speed electrical signaling: overview and limitations," *IEEE Micro,* vol. 18, pp. 12-24, 1998.

[9] D. A. B. Miller, "Physical reasons for optical interconnection," *International Journal of Optoelectronics,* vol. 11, pp. 155-168, May-Jun 1997.

[10] E. Yuceturk, S. C. Esener, H. Dawei, and T. Sze, "Comparative study of very short distance electrical and optical interconnects based on channel characteristics," in *Optics in Computing*, 2003, pp. 7-9.

[11] N. Bamiedakis, J. Beals, R. V. Penty, I. H. White, J. V. Degroot, and T. V. Clapp, "Cost-effective multimode polymer waveguides for high-speed on-board optical interconnects," *IEEE Journal of Quantum Electronics,* vol. 45, pp. 415-424, 2009.

[12] F. Choubani, J. Schutt-Aine, and R. Baca, "Characterization of Skin Effect in High-Speed Interconnects and Spiral Inductors," in *ARFTG Conference Digest-Spring, 54th*, 2000, pp. 1-5.

[13] D. Huang, T. Sze, A. Landin, R. Lytel, and H. L. Davidson, "Optical interconnects: out of the box forever?," *IEEE Journal of Selected Topics in Quantum Electronics,* vol. 9, pp. 614-623, 2003.

[14] M. Li, J. Nuebel, J. L. Drewniak, T. H. Hubing, R. E. DuBroff, and T. P. Van Doren, "EMI reduction from airflow aperture arrays using dual-perforated screens and loss," *IEEE Transactions on Electromagnetic Compatibility,* vol. 42, pp. 135-141, 2000.

[15] R. L. Ozenbaugh and T. M. Pullen, *EMI filter design*. New York: CRC Press, 2012.

[16] S. Shahparnia and O. M. Ramahi, "Electromagnetic interference (EMI) reduction from printed circuit boards (PCB) using electromagnetic bandgap structures," *IEEE Transactions on Electromagnetic Compatibility,* vol. 46, pp. 580-587, 2004.

[17] A. F. Benner, M. Ignatowski, J. A. Kash, D. M. Kuchta, and M. B. Ritter, "Exploitation of optical interconnects in future server architectures," *IBM Journal of Research and Development,* vol. 49, pp. 755-775, 2005.

[18] J. W. Goodman, F. J. Leonberger, S.-Y. Kung, and R. A. Athale, "Optical interconnections for VLSI systems," *Proceedings of the IEEE,* vol. 72, pp. 850-866, 1984.

[19] A. Levi, "Optical interconnects in systems," *Proceedings of the IEEE,* vol. 88, pp. 750-757, 2000.

[20] D. Miller, "Device requirements for optical interconnects to silicon chips," *Proceedings of the IEEE,* vol. 97, pp. 1166-1185, 2009.

[21] D. A. Miller, "Optical interconnects to silicon," *IEEE Journal of Selected Topics in Quantum Electronics,* vol. 6, pp. 1312-1317, 2000.

[22] N. Savage, "Linking with light [high-speed optical interconnects]," *IEEE Spectrum,* vol. 39, pp. 32-36, 2002.

[23] M. A. Taubenblatt, "Optical interconnects for high-performance computing," *Journal of Lightwave Technology,* vol. 30, pp. 448-457, 2012.

[24] G. Jiang, S. Baig, and M. R. Wang, "Tunable Optofluidic Couplers for Dynamic Card-to-Backplane Optical Interconnect," *Journal of Lightwave Technology,* vol. 31, pp. 4135-4141, 2013.

[25] G. Jiang, S. Baig, and M. R. Wang, "Dynamic polymer ribbon couplers for card-to-backplane optical interconnects," in *SPIE OPTO*, 2013, pp. 86300G-86300G-7.

[26] A. Flores, S. Song, J. J. Yang, Z. Liu, and M. R. Wang, "High-speed optical interconnect coupler based on soft lithography ribbons," *Journal of Lightwave Technology,* vol. 26, pp. 1956-1963, 2008.

[27] J. Song and J. Ding, "Silicon Nanowire Waveguides and Their Applications in Planar Wavelength Division Multiplexers/Demultiplexers," in *Nanowires - Fundamental Research*, A. Hashim, Ed., ed Croatia: InTech, 2011.

[28] S. Janz, A. Balakrishnan, S. Charbonneau, P. Cheben, M. Cloutier, A. Delâge*, et al.*, "Planar waveguide echelle gratings in silica-on-silicon," *IEEE Photonics Technology Letters,* vol. 16, pp. 503-505, 2004.

[29] S. Cheung, T. Su, K. Okamoto, and S. Yoo, "Ultra-compact silicon photonic 512× 512 25 GHz arrayed waveguide grating router," *IEEE Journal of Selected Topics in Quantum Electronics,* vol. 20, pp. 310-316, 2014.

[30] W. Bogaerts, P. Dumon, D. V. Thourhout, D. Taillaert, P. Jaenen, J. Wouters*, et al.*, "Compact wavelength-selective functions in silicon-on-insulator photonic wires," *IEEE Journal of Selected Topics in Quantum Electronics,* vol. 12, pp. 1394-1401, 2006.

[31] J. Brouckaert, W. Bogaerts, P. Dumon, D. Van Thourhout, and R. Baets, "Planar concave grating demultiplexer fabricated on a nanophotonic silicon-on-insulator platform," *Journal of Lightwave Technology,* vol. 25, pp. 1269-1275, 2007.

[32] D. Feng, W. Qian, H. Liang, C.-C. Kung, J. Fong, B. J. Luff*, et al.*, "Fabrication insensitive echelle grating in silicon-on-insulator platform," *IEEE Photonics Technology Letters,* vol. 23, pp. 284-286, 2011.

[33] D. S. Gareau, K. Nehal, and M. Rajadhyaksha, "Confocal Mosaicing Microscopy in Skin Excisions: Feasibility of Cancer Margin Screening at the Bedside to Guide Mohs Surgery," in *Reflectance Confocal Microscopy for Skin Diseases*, ed New York: Springer, 2012, pp. 449-454.

[34] A. F. Fercher, W. Drexler, C. K. Hitzenberger, and T. Lasser, "Optical coherence tomography-principles and applications," *Reports on Progress in Physics,* vol. 66, p. 239, 2003.

[35] P. H. Tomlins and R. K. Wang, "Theory, developments and applications of optical coherence tomography," *Journal of Physics D: Applied Physics,* vol. 38, pp. 2519-2535, 2005.

[36] J. Izatt and M. Choma, "Theory of optical coherence tomography," in *Optical Coherence Tomography*, W. Drexler and J. G. Fujimoto, Eds., ed: Springer, 2008, pp. 47-72.

[37] G. Palumbo and R. Pratesi, *Lasers and current optical techniques in biology*. Cambridge: Royal Society of Chemistry, 2004.

[38] R. Hu, D. Dai, and S. He, "A small polymeric ridge waveguide with a high index contrast," *Journal of Lightwave Technology,* vol. 26, pp. 1964-1968, 2008.

[39] M. Kawachi, "Silica waveguides on silicon and their application to integrated-optic components," *Optical and Quantum Electronics,* vol. 22, pp. 391-416, 1990.

[40] K. S. Chiang, "Development of optical polymer waveguide devices," in *OPTO*, 2010, pp. 760507-760507-18.

[41] X. Lin, A. Hosseini, X. Dou, H. Subbaraman, and R. T. Chen, "Low-cost board-to-board optical interconnects using molded polymer waveguide with 45 degree mirrors and inkjet-printed micro-lenses as proximity vertical coupler," *Opt. Express,* vol. 21, pp. 60-69, 2013.

[42] F. E. Doany, C. L. Schow, C. W. Baks, D. M. Kuchta, P. Pepeljugoski, L. Schares*, et al.*, "160 Gb/s bidirectional polymer-waveguide board-level optical interconnects using CMOS-based transceivers," *IEEE Transactions on Advanced Packaging,* vol. 32, pp. 345-359, 2009.

[43] R. Dangel, C. Berger, R. Beyeler, L. Dellmann, M. Gmur, R. Hamelin*, et al.*, "Polymer-waveguide-based board-level optical interconnect technology for datacom applications," *IEEE Transactions on Advanced Packaging,* vol. 31, pp. 759-767, 2008.

[44] A. L. Glebov, M. G. Lee, and K. Yokouchi, "Integration technologies for pluggable backplane optical interconnect systems," *Optical Engineering,* vol. 46, pp. 015403-015403-10, 2007.

[45] M. Immonen, M. Karppinen, and J. K. Kivilahti, "Fabrication and characterization of polymer optical waveguides with integrated micromirrors for three-dimensional board-level optical interconnects," *IEEE Transactions on Electronics Packaging Manufacturing,* vol. 28, pp. 304-311, 2005.

[46] X. Dou, A. X. Wang, X. Lin, and R. T. Chen, "Photolithography-free polymer optical waveguide arrays for optical backplane bus," *Opt. Express,* vol. 19, pp. 14403-14410, 2011.

[47] L. Wang, X. Wang, W. Jiang, J. Choi, H. Bi, and R. Chen, "45 polymer-based total internal reflection coupling mirrors for fully embedded intraboard guided wave optical interconnects," *Applied Physics Letters,* vol. 87, pp. 141110-141110-3, 2005.

[48] X. Wang, W. Jiang, L. Wang, H. Bi, and R. T. Chen, "Fully embedded board-level optical interconnects from waveguide fabrication to device integration," *Journal of Lightwave Technology,* vol. 26, pp. 243-250, 2008.

[49] C. Choi, L. Lin, Y. Liu, J. Choi, L. Wang, D. Haas*, et al.*, "Flexible optical waveguide film fabrications and optoelectronic devices integration for fully embedded board-level optical interconnects," *Journal of Lightwave Technology,* vol. 22, p. 2168, 2004.

[50] X. Dou, X. Wang, X. Lin, D. Ding, D. Z. Pan, and R. T. Chen, "Highly flexible polymeric optical waveguide for out-of-plane optical interconnects," *Opt. Express,* vol. 18, pp. 16227-16233, 2010.

[51] G. Jiang, S. Baig, and M. R. Wang, "Flexible Polymer Waveguides With Integrated Mirrors Fabricated by Soft Lithography for Optical Interconnection," *Journal of Lightwave Technology,* vol. 31, pp. 1835-1841, 2013.

[52] F. Wang, J. Yang, L. Chen, X. Jiang, and M. Wang, "Optical switch based on multimode interference coupler," *IEEE Photonics Technology Letters,* vol. 18, pp. 421-423, 2006.

[53] Y. Shi, C. Zhang, H. Zhang, J. H. Bechtel, L. R. Dalton, B. H. Robinson*, et al.*, "Low (sub-1-volt) halfwave voltage polymeric electro-optic modulators achieved by controlling chromophore shape," *Science,* vol. 288, pp. 119-122, 2000.

[54] A. Rodrıguez, G. Vitrant, P. Chollet, and F. Kajzar, "Optical control of an integrated interferometer using a photochromic polymer," *Applied Physics Letters,* vol. 79, pp. 461-463, 2001.

[55] X. Ke, M. R. Wang, and D. Li, "All-optical controlled variable optical attenuator using photochromic sol gel material," *IEEE Photonics Technology Letters,* vol. 18, pp. 1025-1027, 2006.

[56] R. Friend, R. Gymer, A. Holmes, J. Burroughes, R. Marks, C. Taliani*, et al.*, "Electroluminescence in conjugated polymers," *Nature,* vol. 397, pp. 121-128, 1999.

[57] A. Hashim, N. Bamiedakis, J. Beals, Y. Hao, R. Penty, and I. White, "Polymer-based board-level optical interconnects," in *Photonics (ICP), 2011 IEEE 2nd International Conference on*, 2011, pp. 1-5.

[58] X. Dou, X. Wang, H. Huang, X. Lin, D. Ding, D. Z. Pan*, et al.*, "Polymeric waveguides with embedded micro-mirrors formed by Metallic Hard Mold," *Opt. Express,* vol. 18, pp. 378-385, 2010.

[59] J.-S. Kim, J.-W. Kang, and J.-J. Kim, "Simple and low cost fabrication of thermally stable polymeric multimode waveguides using a UV-curable epoxy," *Japanese Journal of Applied Physics,* vol. 42, p. 1277, 2003.

[60] I. Papakonstantinou, D. R. Selviah, K. Wang, R. A. Pitwon, K. Hopkins, and D. Milward, "Optical 8-channel, 10 Gb/s MT pluggable connector alignment technology for precision coupling of laser and photodiode arrays to polymer waveguide arrays for optical board-to-board interconnects," in *Electronic Components and Technology Conference, 2008. ECTC 2008. 58th*, 2008, pp. 1769-1775.

[61] L. Eldada, C. Xu, K. M. Stengel, L. W. Shacklette, and J. T. Yardley, "Laser-fabricated low-loss single-mode raised-rib waveguiding devices in polymers," *Journal of Lightwave Technology,* vol. 14, pp. 1704-1713, 1996.

[62] W. Wong, J. Zhou, and E. Pun, "Low-loss polymeric optical waveguides using electron-beam direct writing," *Applied Physics Letters,* vol. 78, pp. 2110-2112, 2001.

[63] W. Wong and E. Pun, "Polymeric waveguide wavelength filters using electron-beam direct writing," *Applied Physics Letters,* vol. 79, pp. 3576-3578, 2001.

[64] B. Yang, L. Yang, R. Hu, Z. Sheng, D. Dai, Q. Liu*, et al.*, "Fabrication and characterization of small optical ridge waveguides based on SU-8 polymer," *Journal of Lightwave Technology,* vol. 27, pp. 4091-4096, 2009.

[65] K. Tung, W. Wong, and E. Pun, "Polymeric optical waveguides using direct ultraviolet photolithography process," *Applied Physics A,* vol. 80, pp. 621-626, 2005.

[66] J. A. Rogers and R. G. Nuzzo, "Recent progress in soft lithography," *Materials Today,* vol. 8, pp. 50-56, 2005.

[67] L. Eldada and L. W. Shacklette, "Advances in polymer integrated optics," *IEEE Journal of Selected Topics in Quantum Electronics,* vol. 6, pp. 54-68, 2000.

[68] Y. Xia and G. M. Whitesides, "Soft lithography," *Annual Review of Materials Science,* vol. 28, pp. 153-184, 1998.

[69] G. Jiang, S. Baig, and M. R. Wang, "Prism-assisted inclined UV lithography for 3D microstructure fabrication," *Journal of Micromechanics and Microengineering,* vol. 22, p. 085022, 2012.

[70] G. Jiang, K. Shen, and M. R. Wang, "Fabrication of 3D Micro-and Nano-Structures by Prism-Assisted UV and Holographic Lithography," in *Updated in Advanced Lithography*, S. Hosaka, Ed., ed Croatia: InTech, 2013.

[71] A. Flores, S. Song, S. Baig, and M. R. Wang, "Vacuum-assisted microfluidic technique for fabrication of guided wave devices," *IEEE Photonics Technology Letters,* vol. 20, pp. 1246-1248, 2008.

[72] A. Fujii, T. Suzuki, K. Shimizu, K. Yatsuda, M. Igusa, S. Ohtsu*, et al.*, "A novel fabrication technology of a polymer optical waveguide and its application," in *Optics East 2007*, 2007, pp. 677506-677506-12.

[73] S. J. Ahn and J. Moon, "Vacuum‐Assisted Microfluidic Lithography of Ceramic Microstructures," *Journal of the American Ceramic Society,* vol. 88, pp. 1171-1174, 2005.

[74] W.-J. Lee, S. H. Hwang, M. J. Kim, E. J. Jung, J. B. An, G. W. Kim*, et al.*, "Multilayered 3-D Optical Circuit With Mirror-Embedded Waveguide Films," *IEEE Photonics Technology Letters,* vol. 24, pp. 1179-1181, 2012.

[75] W.-J. Lee, S. H. Hwang, J. W. Lim, and B. S. Rho, "Polymeric waveguide film with embedded mirror for multilayer optical circuits," *IEEE Photonics Technology Letters,* vol. 21, pp. 12-14, 2009.

[76] T. Yoshimura, M. Miyazaki, Y. Miyamoto, N. Shimoda, A. Hori, and K. Asama, "Three-dimensional optical circuits consisting of waveguide films and optical Z-connections," *Journal of Lightwave Technology,* vol. 24, pp. 4345-4352, 2006.

[77] M. Hikita, R. Yoshimura, M. Usui, S. Tomaru, and S. Imamura, "Polymeric optical waveguides for optical interconnections," *Thin Solid Films,* vol. 331, pp. 303-308, 1998.

[78] G. Van Steenberge, P. Geerinck, S. Van Put, J. Van Koetsem, H. Ottevaere, D. Morlion*, et al.*, "MT-compatible laser-ablated interconnections for optical printed circuit boards," *Journal of Lightwave Technology,* vol. 22, pp. 2083-2090, 2004.

[79] M. Kagami, A. Kawasaki, and H. Ito, "A polymer optical waveguide with out-of-plane branching mirrors for surface-normal optical interconnections," *Journal of Lightwave Technology,* vol. 19, p. 1949, 2001.

[80] N. Hendrickx, J. Van Erps, E. Bosman, C. Debaes, H. Thienpont, and P. Van Daele, "Embedded micromirror inserts for optical printed circuit boards," *IEEE Photonics Technology Letters,* vol. 20, pp. 1727-1729, 2008.

[81] J. Inoue, T. Ogura, K. Kintaka, K. Nishio, Y. Awatsuji, and S. Ura, "Fabrication of embedded 45-degree micromirror using liquid-immersion exposure for single-mode optical waveguides," *Journal of Lightwave Technology,* vol. 30, pp. 1563-1568, 2012.

[82] F. Wang, F. Liu, and A. Adibi, "45 Degree polymer micro-mirror integration for board-level three-dimensional optical interconnects," in *Electronic Components and Technology Conference, 2009. ECTC 2009. 59th*, 2009, pp. 1842-1845.

[83] M. Han, D.-H. Hyun, H.-H. Park, S. S. Lee, C.-H. Kim, and C. Kim, "A novel fabrication process for out-of-plane microneedle sheets of biocompatible polymer," *Journal of Micromechanics and Microengineering,* vol. 17, p. 1184, 2007.

[84] K.-Y. Hung, H.-T. Hu, and F.-G. Tseng, "Application of 3D glycerol-compensated inclined-exposure technology to an integrated optical pick-up head," *Journal of Micromechanics and Microengineering,* vol. 14, p. 975, 2004.

[85] D. Dai, L. Yang, Z. Sheng, B. Yang, and S. He, "Compact Microring Resonator With 2$\,\ times\, $2 Tapered Multimode Interference Couplers," *Journal of Lightwave Technology,* vol. 27, pp. 4878-4883, 2009.

[86] A. Flores and M. R. Wang, "Soft Lithographic Fabrication of Micro Optic and Guided Wave Devices," in *Lithography*, M. Wang, Ed., ed Croatia: InTech, 2010.

[87] D. Qin, Y. Xia, and G. M. Whitesides, "Soft lithography for micro-and nanoscale patterning," *Nature Protocols,* vol. 5, pp. 491-502, 2010.

[88] X. M. Zhao, Y. Xia, and G. M. Whitesides, "Fabrication of three‐dimensional micro‐structures: Microtransfer molding," *Advanced Materials,* vol. 8, pp. 837-840, 1996.

[89] S. Baig, G. Jiang, Q. Sun, and M. R. Wang, "Fabrication of eight-channel array single-mode waveguides via vacuum assisted microfluidics," in *SPIE MOEMS-MEMS*, 2012, pp. 82490P-82490P-7.

[90] S. Baig, G. Jiang, Q. Sun, and M. Wang, "Fabrication of single-mode channel polymer waveguides using vacuum assisted microfluidic soft lithography," *Journal of the European Optical Society-Rapid publications,* vol. 8, 2013.

[91] S. Baig, G. Jiang, and M. R. Wang, "Light sensitive waveguides fabricated by vacuum assisted microfluidics," in *SPIE MOEMS-MEMS*, 2013, pp. 861310-861310-7.

[92] Z. Ling and K. Lian, "SU-8 3D microoptic components fabricated by inclined UV lithography in water," *Microsystem Technologies,* vol. 13, pp. 245-251, 2007.

[93] H. Sato, T. Kakinuma, J. S. Go, and S. Shoji, "In-channel 3-D micromesh structures using maskless multi-angle exposures and their microfilter application," *Sensors and Actuators A: Physical,* vol. 111, pp. 87-92, 2004.

[94] H.-P. Shieh, Y.-P. Huang, and K.-W. Chien, "Micro-optics for liquid crystal displays applications," *Journal of Display Technology,* vol. 1, pp. 62-76, 2005.

[95] Y.-K. Yoon, J.-H. Park, and M. G. Allen, "Multidirectional UV lithography for complex 3-D MEMS structures," *Journal of Microelectromechanical Systems,* vol. 15, pp. 1121-1130, 2006.

[96] H. Sato, D. Yagyu, S. Ito, and S. Shoji, "Improved inclined multi-lithography using water as exposure medium and its 3D mixing microchannel application," *Sensors and Actuators A: Physical,* vol. 128, pp. 183-190, 2006.

[97] S. Baek and S. Song, "A one-step photolithography method for fabrication of a staggered herringbone mixer using inclined UV lithography," *Journal of Micromechanics and Microengineering,* vol. 21, p. 077001, 2011.

[98] Y.-K. Yoon, J.-H. Park, J.-W. Lee, M. R. Prausnitz, and M. G. Allen, "A thermal microjet system with tapered micronozzles fabricated by inclined UV lithography for transdermal drug delivery," *Journal of Micromechanics and Microengineering,* vol. 21, p. 025014, 2011.

[99] C. Beuret, G.-A. Racine, J. Gobet, R. Luthier, and N. de Rooij, "Microfabrication of 3D multidirectional inclined structures by UV lithography and electroplating," in *Micro Electro Mechanical Systems, 1994, MEMS'94, Proceedings, IEEE Workshop on*, 1994, pp. 81-85.

[100] M. Han, W. Lee, S.-K. Lee, and S. S. Lee, "3D microfabrication with inclined/rotated UV lithography," *Sensors and Actuators A: Physical,* vol. 111, pp. 14-20, 2004.

[101] A. del Campo and E. Arzt, "Fabrication approaches for generating complex micro-and nanopatterns on polymeric surfaces," *Chemical Reviews,* vol. 108, pp. 911-945, 2008.

[102] A. Del Campo and C. Greiner, "SU-8: a photoresist for high-aspect-ratio and 3D submicron lithography," *Journal of Micromechanics and Microengineering,* vol. 17, p. R81, 2007.

[103] W.-J. Kang, E. Rabe, S. Kopetz, and A. Neyer, "Novel exposure methods based on reflection and refraction effects in the field of SU-8 lithography," *Journal of Micromechanics and Microengineering,* vol. 16, p. 821, 2006.

[104] Z. Zhu, Z.-F. Zhou, Q.-A. Huang, and W.-H. Li, "Modeling, simulation and experimental verification of inclined UV lithography for SU-8 negative thick photoresists," *Journal of Micromechanics and Microengineering,* vol. 18, p. 125017, 2008.

[105] Y.-J. Huang, T.-L. Chang, H.-P. Chou, and C.-H. Lin, "A novel fabrication method for forming inclined groove-based microstructures using optical elements," *Japanese Journal of Applied Physics,* vol. 47, p. 5287, 2008.

[106] G. Jiang, S. Baig, and M. R. Wang, "Soft lithography fabricated polymer waveguides and 45° inclined mirrors for card-to-backplane optical interconnects," in *SPIE OPTO*, 2012, pp. 82670R-82670R-7.

[107] U. Levy and R. Shamai, "Tunable optofluidic devices," *Microfluidics and Nanofluidics,* vol. 4, pp. 97-105, 2008.

[108] X. Heng, D. Erickson, L. R. Baugh, Z. Yaqoob, P. W. Sternberg, D. Psaltis*, et al.*, "Optofluidic microscopy—a method for implementing a high resolution optical microscope on a chip," *Lab on a Chip,* vol. 6, pp. 1274-1276, 2006.

[109] S. Kuiper and B. Hendriks, "Variable-focus liquid lens for miniature cameras," *Applied Physics Letters,* vol. 85, p. 1128, 2004.

[110] S.-Y. Teh, R. Lin, L.-H. Hung, and A. P. Lee, "Droplet microfluidics," *Lab on a Chip,* vol. 8, pp. 198-220, 2008.

[111] P. Garstecki, M. J. Fuerstman, H. A. Stone, and G. M. Whitesides, "Formation of droplets and bubbles in a microfluidic T-junction—scaling and mechanism of break-up," *Lab on a Chip,* vol. 6, pp. 437-446, 2006.

[112] L. Yobas, S. Martens, W.-L. Ong, and N. Ranganathan, "High-performance flow-focusing geometry for spontaneous generation of monodispersed droplets," *Lab on a Chip,* vol. 6, pp. 1073-1079, 2006.

[113] K. Okamoto, "Wavelength-division-multiplexing devices in thin SOI: Advances and prospects," *IEEE Journal of Selected Topics in Quantum Electronics,* vol. 20, pp. 248-257, 2014.

[114] M. Nordström, D. A. Zauner, A. Boisen, and J. Hübner, "Single-mode waveguides with SU-8 polymer core and cladding for MOEMS applications," *Journal of Lightwave Technology,* vol. 25, pp. 1284-1289, 2007.

[115] M. C. Hutley, *Diffraction gratings*. London: Academic Press, 1982.

[116] D. Chowdhury, "Design of low-loss and polarization-insensitive reflection grating-based planar demultiplexers," *IEEE Journal of Selected Topics in Quantum Electronics,* vol. 6, pp. 233-239, 2000.

[117] R. J. Lycett, D. F. G. Gallagher, and V. J. Brulis, "Perfect Chirped Echelle Grating Wavelength Multiplexor: Design and Optimization," *IEEE Photonics Journal,* vol. 5, pp. 2400123-2400123, 2013.

[118] J. He, E. S. Koteles, B. Lamontagne, L. Erickson, A. Delage, and M. Davies, "Integrated polarization compensator for WDM waveguide demultiplexers," *IEEE Photonics Technology Letters,* vol. 11, pp. 224-226, 1999.

[119] D. Feng, N.-N. Feng, C.-C. Kung, H. Liang, W. Qian, J. Fong*, et al.*, "Compact single-chip VMUX/DEMUX on the silicon-on-insulator platform," *Optics Express,* vol. 19, pp. 6125-6130, 2011.

[120] X. Chen, J. N. McMullin, C. J. Haugen, and R. G. DeCorby, "Planar concave grating demultiplexer for coarse WDM based on confocal ellipses," *Optics Communications,* vol. 237, pp. 71-77, 2004.

[121] S. Pathak, M. Vanslembrouck, P. Dumon, D. Van Thourhout, and W. Bogaerts, "Optimized silicon AWG with flattened spectral response using an MMI aperture," *Journal of Lightwave Technology,* vol. 31, pp. 87-93, 2013.

[122] G. Jiang, S. Baig, H. Lu, K. Shen, and M. R. Wang, "Planar concave grating with flattened spectral response for wavelength demultiplexing optical interconnection," in *SPIE OPTO*, 2015, pp. 93680R-93680R-7.

[123] L. B. Soldano and E. C. Pennings, "Optical multi-mode interference devices based on self-imaging: principles and applications," *Journal of Lightwave Technology,* vol. 13, pp. 615-627, 1995.

[124] B. Akca, V. D. Nguyen, J. Kalkman, T. van Leeuwen, K. Worhoff, R. de Ridder*, et al.*, "Towards spectral-domain optical coherence tomography on a silicon chip," in *Quantum Electronics Conference & Lasers and Electro-Optics (CLEO/IQEC/PACIFIC RIM), 2011*, 2011, pp. 775-777.

[125] C. Akcay, P. Parrein, and J. P. Rolland, "Estimation of longitudinal resolution in optical coherence imaging," *Applied Optics,* vol. 41, pp. 5256-5262, 2002.

[126] D. Nguyen, "Integrated-optics-based optical coherence tomography," Ph.D. Dissertation, University of Amsterdam, 2013.

[127] A. Nitkowski, K. Preston, N. Sherwood-Droz, B. S. Schmidt, and A. R. Hajian, "On-chip spectrometer for low-cost optical coherence tomography," in *SPIE BiOS*, 2014, pp. 89340F-89340F-8.

[128] A. Nitkowski, K. J. Preston, N. Sherwood-Droz, B. B. Behr, Y. Bismilla, A. T. Cenko*, et al.*, "Sensing systems using chip-based spectrometers," in *SPIE Defense+ Security*, 2014, pp. 908332-908332-8.